

ER-5288

ADVANCED INDUCER

STUDY
(NAS 8-4006)

COPY

Prepared for
The Propulsion and Vehicle Engineering Division
George C. Marshall Space Flight Center
National Aeronautics and Space Administration
Huntsville, Alabama

MAY 24, 1963



TAPCO a division of
Thompson Ramo Wooldridge Inc.

PROJECT

512-0X9440-08

ER-5288

ADVANCED INDUCER STUDY

(NAS 8-4006)

Prepared for:

The Propulsion and Vehicle Engineering Division
George C. Marshall Space Flight Center
National Aeronautics and Space Administration
Huntsville, Alabama

PREPARED BY:

H B Bosch
H. B. Bosch
Engineering Specialist

P Cooper
P. Cooper
Engineering Specialist

Wm F Stoermer
Wm. F. Stoermer
Program Manager

CHECKED BY:

J D Stanitz
J. D. Stanitz
Chief Scientist

Wm F Stoermer
Wm. F. Stoermer
Program Manager

APPROVED BY:

J F Urich
J. F. Urich
Chief Engineer
Fluid Systems

DATE

May 24, 1963

DEPARTMENT

Fluid Systems Development Engineering

Thompson Ramo Wooldridge Inc.

CLEVELAND, OHIO, U. S. A.

ABSTRACT

This report presents the results of work conducted by the Tapco Division of Thompson Ramo Wooldridge Inc. to satisfy the NASA-Marshall contract NAS 8-4006. The period of performance for this advanced inducer study was thirteen months, which included both analytical investigations and an experimental test program.

The major emphasis of the theoretical effort was to set up an analytical flow model. Mathematical methods and techniques were developed for a numerical solution of this model on a digital computer; both the FORTRAN listing and performance calculations obtained from this program are reported. Studies were completed in regard to loss distributions, dimensionless parameters, scaling laws, and correlation factors which, when combined with the velocity distributions obtained from the flow field solution, form the basis for design criteria or performance evaluation of full scale inducers.

Concurrent with, and in support of, the aforementioned analytical work, a referee inducer was tested in both water and liquid hydrogen. The data obtained in over ten hours running time in the water loop plus four usable liquid hydrogen test runs are presented for the purpose of evaluating the theoretical results.

TABLE OF CONTENTS

	<u>Page</u>
1.0 INTRODUCTION	1-1
2.0 SUMMARY AND DISCUSSION	2-1
3.0 CONCLUSIONS AND RECOMMENDATIONS	3-1
4.0 TECHNICAL STUDIES AND PROCEDURES.	4-1
4.1 Inducer Fluid Mechanics and Thermodynamics (the Flow Model) . .	4-1
4.1.1 Basic Flow Relations	4-1
4.1.2 The Equation of State	4-3
4.1.3 Losses	4-6
4.2 Quasi Three-Dimensional Solution of Axial Inducer Flow Field . .	4-9
4.2.1 Method of Analysis	4-9
4.2.2 Procedure for Calculation	4-11
4.2.3 Blade-to-Blade Solution.	4-14
4.2.4 Mathematical Methods for Solution	4-18
4.2.5 Results and Applicability to Design Methods	4-21
4.3 Three-Dimensional Solution of Inducer Flow Field	4-23
4.3.1 General Discussion	4-23
4.3.2 Mathematical Methods for Three-Dimensional Solution of the Flow Model.	4-23
4.3.2.1 Introduction	4-23
4.3.2.2 Development of Equations	4-24
4.3.2.3 Numerical Methods	4-29
4.3.2.4 Iteration Methods	4-31
4.3.2.5 General Boundary Conditions	4-33
4.3.2.6 Simplified Boundary Conditions	4-33
4.3.3 Comments on the Three-Dimensional Solution and Recommendations	4-36
4.3.3.1 General Observations	4-36
4.3.3.2 W as Independent Variable	4-36
4.3.3.3 Special Algorithm for Calculating Partial Derivatives	4-36
4.3.3.4 Comparison of Methods A and B	4-38
4.3.3.5 Recommendations	4-38



TABLE OF CONTENTS (Continued)

	<u>Page</u>
4.4 Studies of Scale and Fluid Effects	4-39
4.4.1 Introduction	4-39
4.4.2 Dimensional Analysis	4-39
4.4.3 Bubble Studies	4-42
4.4.4 Application of the Similarity Parameters	4-44
4.4.5 Net Positive Suction Head Requirements	4-47
4.5 Advanced Design Criteria	4-50
4.5.1 Introduction	4-50
4.5.2 Relations of Parameters and Sizing Methods	4-50
4.5.3 Design Considerations for the Internal Flow Field	4-52
4.5.4 One-Dimensional Homogeneous Two-Phase Flow	4-54
4.5.4.1 Two-Phase Flow in a Nozzle	4-54
4.5.4.2 Two-Phase Flow in an Inducer Test Set Up	4-57
4.6 Test Program	4-65
4.6.1 Test Vehicle	4-65
4.6.2 Test Inducer	4-65
4.6.3 Test Set Up.	4-68
4.6.3.1 Water Loop	4-68
4.6.3.2 Cryogenic Loop	4-68
4.6.4 Test Instrumentation	4-73
4.6.4.1 Water Tests	4-73
4.6.4.2 Cryogenic Tests	4-73
4.6.4.3 Instrument Accuracy	4-74
4.6.5 Test Procedure and Results	4-74
4.6.5.1 Water Run	4-75
4.6.5.2 Cryogenic Runs	4-76
4.6.6 Test Program Conclusions and Recommendations	4-78
4.7 Presentation and Discussion of Results	4-83
4.7.1 Introduction	4-83
4.7.2 Test Results.	4-83
4.7.3 Results of Theoretical Calculations.	4-90
4.7.4 Conclusions	4-101
APPENDIX A - Nomenclature	A-1
APPENDIX B - References	B-1
APPENDIX C - Blade Contour of Referee Inducer	C-1
APPENDIX D - Instructions for Use of Computer Program.	D-1

LIST OF ILLUSTRATIONS

	<u>Page</u>
4.1.2-1 Fluid State	4-2
4.2.1-1 Meridional Inducer Flow Analysis	4-9
4.2.1-2 Blade-to-Blade Flow Analysis	4-10
4.2.3-1 Analysis for Linear Blade-to-Blade Pressure Distribution	4-16
4.2.3-2 Analysis for Linear Blade-to-Blade Relative Velocity Distribution.	4-16
4.2.4-1 Axial View of Two Radially Adjacent Annuli	4-19
4.2.4-2 Hypothetical Residual vs Radius Curve	4-20
4.3.2-1 The Orthonormal Triad ($\hat{r} : \hat{z} : \hat{\tau}$)	4-24
4.3.2-2 Developed View of Inducer Flow Channel Showing Boundaries	4-34
4.3.3-1 Configuration for Partial Derivative Algorithm	4-37
4.4.3-1 $\log_N P_i/P_o$ vs Bubble Radius	4-43
4.4.5-1 Vapor-to-Liquid Volume Ratio Distributions on Inducer Volumes	4-48
4.5.4-1 Two-Phase Flow in the Throat of a Nozzle	4-56
4.5.4-2 Analysis of Fluid State at Inducer Inlet for Two-Phase Flow	4-58
4.6.1-1 Inducer Test Vehicle	4-66
4.6.1-2 Test Vehicle Disassembled	4-67
4.6.1-3 Test Vehicle With Shroud	4-67
4.6.1-4 Test Vehicle Without Shroud	4-67
4.6.3-1 Dynamometer Installation (Bldg. 43)	4-69
4.6.3-2 Control Room (Bldg. 42)	4-69
4.6.3-3 Water Test Set Up Schematic	4-70



LIST OF ILLUSTRATIONS (Continued)

	<u>Page</u>
4.6.3-4 Water Loop Set Up	4-69
4.6.3-5 Cryogenic Test Set Up Schematic	4-71
4.6.3-6 Cryogenic Set Up	4-72
4.6.3-7 Facility	4-72
4.6.3-8 Cryogenic Set Up with Insulation	4-72
4.6.4-1 Total-Static Angle Probe Calibration	4-75
4.6.5-1 Impeller Pitting After Ten Hours of Water Operation	4-77
4.7.2-1 Wall Static Pressure Coefficient vs Flow Efficient (Non-Cavitating)	4-85
4.7.2-2 Total Head Coefficient vs Cavitation Parameter, in Water	4-86
4.7.2-3 Measured Velocity and Pressure Distributions vs Radius at 16,000 RPM, 0.1139 ϕ , and 0.1947 τ	4-88
4.7.2-4 Measured Velocity and Pressure Distributions vs Radius at 16,000 RPM, 0.1139 ϕ , and 0.0408 τ	4-88
4.7.2-5 Measured Velocity and Pressure Distributions vs Radius at 12,000 RPM, 0.1139 ϕ , and 0.2154 τ	4-88
4.7.2-6 Measured Velocity and Pressure Distributions vs Radius at 12,000 RPM, 0.1139 ϕ , and 0.0528 τ	4-88
4.7.2-7 Measured Velocity and Pressure Distributions vs Radius at 8,000 RPM, 0.1139 ϕ , and 0.3351 τ	4-88
4.7.2-8 Measured Velocity and Pressure Distributions vs Radius at 8,000 RPM, 0.1139 ϕ , and 0.1127 τ	4-88
4.7.2-9 Measured Velocity and Pressure Distributions vs Radius at 16,000 RPM, 0.0785 ϕ , and 0.1593 τ	4-88
4.7.2-10 Measured Velocity and Pressure Distributions vs Radius at 16,000 RPM, 0.0785 ϕ , and 0.0335 τ	4-88

LIST OF ILLUSTRATIONS (Continued)

	<u>Page</u>
4.7.2-11 Measured Velocity and Pressure Distributions vs Radius at 12,000 RPM, and 0.0785 ϕ , and 0.1884 τ	4-88
4.7.2-12 Measured Velocity and Pressure Distributions vs Radius at 12,000 RPM, and 0.0785 ϕ , and 0.0494 τ	4-88
4.7.2-13 Measured Velocity and Pressure Distributions vs Radius at 8,000 RPM, and 0.0785 ϕ , and 0.2584 τ	4-88
4.7.2-14 Measured Velocity and Pressure Distributions vs Radius at 8,000 RPM, and 0.0785 ϕ , and 0.1119 τ	4-88
4.7.2-15 Total Head Coefficient vs Cavitation Parameter, in Hydrogen . .	4-89
4.7.2-16 Measured Velocity and Pressure Distributions vs Radius at 20,000 RPM, 0.1100 ϕ , and 0.0531 τ	4-89
4.7.2-17 Measured Velocity and Pressure Distributions vs Radius at 20,000 RPM, 0.1090 ϕ , and 0.0399 τ	4-89
4.7.3-1 Efficiency vs Reynolds Number, for Theoretical Incompressible Flow	4-92
4.7.3-2 Theoretical Pressure Distribution on Blades	4-93
4.7.3-3 Theoretical Relative Velocity Distributions on Blades	4-93
4.7.3-4 Theoretical Pressure Distribution on Blades	4-94
4.7.3-5 Theoretical Relative Velocity Distributions on Blades	4-94
4.7.3-6 Theoretical Velocity and Pressure Distributions vs Radius at 0.1139 ϕ	4-95
4.7.3-7 Theoretical Velocity and Pressure Distributions vs Radius at 16,000 RPM, 0.1139 ϕ , and Water at 82°F	4-95
4.7.3-8 Theoretical Velocity and Pressure Distributions vs Radius at 12,000 RPM, 0.1139 ϕ , and Water at 82°F	4-95
4.7.3-9 Theoretical Velocity and Pressure Distributions vs Radius at 8,000 RPM, 0.1139 ϕ , and Water at 82°F	4-95



LIST OF ILLUSTRATIONS (Continued)

		<u>Page</u>
4.7.3-10	Theoretical Velocity and Pressure Distributions vs Radius at 16,000 RPM, 0.1139 ϕ , and Hydrogen at 20°K	4-95
4.7.3-11	Theoretical Velocity and Pressure Distribution vs Radius at 20,000 RPM, 0.1139 ϕ , and Hydrogen at 20°K	4-95
4.7.3-12	Theoretical Velocity and Pressure Distributions vs Radius at 30,000 RPM, 0.1139 ϕ , and Hydrogen at 20°K	4-95
4.7.3-13	Theoretical Velocity and Pressure Distributions vs Radius at 16,000 RPM, 0.1139 ϕ , and RP-1 at 60°F	4-95
4.7.3-14	Theoretical Velocity and Pressure Distributions vs Radius at 16,000 RPM, 0.1139 ϕ , and Oxygen at 90°K	4-95
4.7.3-15	"Head Coefficient" of Initial 8-1/3% of Inducer vs Cavitation Parameter	4-98
4.7.3-16	Efficiency of Initial 8-1/3% of Inducer vs Suction Parameter . .	4-98
4.7.3-17	Theoretical Pressure Distribution on Blades	4-99
4.7.3-18	Theoretical Pressure Distribution on Blades	4-99
4.7.3-19	Theoretical Velocity and Pressure Distributions vs Radius at 16,000 RPM, 0.1139 ϕ , and $\geq 0.2660 \tau$	4-100
4.7.3-20	Theoretical Velocity and Pressure Distributions vs Radius at 16,000 RPM, 0.1139 ϕ , and 0.2030 τ	4-100
4.7.3-21	Theoretical Velocity and Pressure Distributions vs Radius at 16,000 RPM, 0.1139 ϕ , and 0.1600 τ	4-100
4.7.3-22	Theoretical Velocity and Pressure Distributions vs Radius at 16,000 RPM, 0.1139 ϕ , and 0.1200 τ	4-100
4.7.3-23	Theoretical Velocity and Pressure Distributions vs Radius at 16,000 RPM, 0.1139 ϕ , and 0.0800 τ	4-100
C-1	Typical Blade Contour Gage Data for No. 1 Blade	C-2

LIST OF ILLUSTRATIONS (Continued)

		<u>Page</u>
C-2	Inducer, NASA Test Vehicle	C-3
C-3	NASA Design Data for Circular Arc Section of Referee Inducer .	C-4
D-1	Flow Diagram for Quasi Three -Dimensional Solution	D-19

LIST OF TABLES

	<u>Page</u>
4.4.4-1 Values of Fluid Thermodynamic Parameter	4-45
4.4.4-2 Conditions of Dynamic Similarity	4-46
4.5.4-1 Summary of Two Phase Hydrogen Flow Calculations	4-64
4.6.5-1 Water Depression Test	4-80
4.6.5-2 Liquid Hydrogen Depression Test	4-81
4.7.5.3 Liquid Hydrogen Depression Test	4-82
4.7.1-1 Test Results	4-84
4.7.3-1 Results of Theoretical Calculations	4-91
C-1 Blade Coordinates and Channel Boundaries Used to Analyze Referee Inducer	C-6

1.0 INTRODUCTION

The George C. Marshall Space Flight Center of the National Aeronautics and Space Administration at Huntsville, Alabama contracted with the Tapco Division of Thompson Ramo Wooldridge Inc. at Cleveland, Ohio for an advanced inducer study in keeping with NAS 8-4006 dated February 12, 1962. The results of the work performed to satisfy this contract are reported herein. They were conducted according to Tapco Plan 272-074700-08 under the Fluid Systems 512-009440-08 (basic) project assignment.

The cognizant NASA office for work under this contract was Liquid Propulsion Systems (RPL), with technical management by Messrs. Keith B. Chandler and Loren Gross (M-P&VE-PA). Mr. Mel Hartman and other members of the Pump Section of the LeRC Turbopump Branch acted as technical consultants on analytical methods, cryogenic procedures, and instrumentation techniques.

The purpose of this program was to establish advanced design criteria for high performance inducers and for their application to large rocket engine propellant pumps. To attain the objectives of this program, it was necessary to conduct concurrent analytical studies and experimental work as follows:

1. Analytical studies were made to determine the influence of fluid thermodynamic and hydraulic properties on the theoretical performance of an inducer. The effects of cavitation, bubble size, and physical characteristics of such things as blading profiles were also investigated to establish their effects on the velocity distribution in the flow field. This flow field was described by an analytical model which was programmed for numerical solution on a digital computer. Water, liquid oxygen, liquid hydrogen, and RP-1 were considered as the working fluids.
2. Referee inducer testing of a scaled model was conducted to provide data for comparison with analytical results. These data will also be usable for investigation of scaling factors and correlation laws among fluids. Water and liquid hydrogen were selected as the test fluids.

2.0 SUMMARY AND DISCUSSION

Three characteristic problems form the basis of an advanced inducer technology and of the work now being reported. First, an inducer is generally situated upstream of a high pressure pump impeller, and the proper design of the latter requires a knowledge of inducer outlet fluid state and velocity distributions. These distributions are the primary basis of judgment of inducer performance. They vary with inlet and other flow conditions, and analysis of the inducer flow field produces the desired information. This analysis can be achieved by (a) examination of test results, (b) the solution of a theoretical flow model by approximate methods, or (c) a three-dimensional solution of the flow model. Normally, all these methods are required during the course of study, and work was done in each area. Approach (a) has been generally used in other work, but much of the detailed information has been obtained in water tests on scale models. This brings up the second characteristic inducer problem; viz., the question of how to properly apply test results to different model sizes and fluids. A dimensional analysis of the process furnishes the requirements for similarity, and the solution of the equations involved - either analytically or empirically-provides the effects of departures from similarity. Analysis was conducted in both these areas, yielding some results in two-phase similarity. An understanding of the above two basic problems leads to the third one; viz., the establishment of inducer design criteria for operation at minimum NPSH conditions. In addition to criteria for pressure and velocity distributions on the blades of a low NPSH machine,¹ requirements imposed upon the geometry by the mass flow limitations of a vaporizing liquid need to be established. Studies of the flow of a vaporizing liquid were carried out and have led to new conclusions in this area.

Detailed descriptions of the technical studies and procedures are presented in Section 4.0.

Section 4.1 describes the theoretical flow model that was set up to form the basis of the studies. The model applies to cavitation since it assumes a homogeneous flow of a liquid and its gas under conditions of thermodynamic equilibrium. In other words, the state properties are assumed to be continuous functions of position. This assumes that any bubbles that exist are infinitesimal in size and infinitely many. Losses are accounted for by local application of friction and diffusion loss factors. On the basis of observations and of thermodynamic properties, hydrogen flow appears to conform most closely to this flow model as regards the homogeneity and equilibrium assumptions.

Section 4.2 treats the approximate or quasi three-dimensional solution of the flow model applied to the inducer flow field. Although the analysis was done for axially symmetric flow in an essentially axial-flow machine, adaptation to other arrangements is possible. It was programmed and run to solution for flow in an existing inducer. The solution gives pressure and velocity distributions on the blades within the inducer and at the outlet of the machine. The results are presented in Section 4.7.

¹ Superscript numerals denote references in Appendix B



Section 4.3 describes the work that was done on a three-dimensional solution of the flow field. The advantages of this solution over the approximate one discussed above are those obtained by a more exact analysis and the ability to treat secondary or corkscrew type flows in the inducer passages. Further work is required to complete this solution.

Section 4.4 describes the dimensional analysis that yielded the criteria for similarity and, therefore, scaling and correlation among various fluids. The approximate solution of the flow field was non-dimensionalized, also revealing the parameters whose effects are calculated in the program. The flow model was used as a basis for this work, and so the results cover only the homogeneous, equilibrium case. However, some work was done to provide insight into the effects of bubble size.

Section 4.5 discusses the inducer design criteria that are obtainable from the above studies. One-dimensional flow studies show how to obtain mass flow limits for a vaporizing liquid. When combined with the pressure and velocity distributions required within the inducer blade system, lower limits are imposed on the mass flow of such a fluid. Further work is required to show how the shifting of blade loading (and therefore the changes in these limits) under two-phase conditions lead to an optimum inducer geometry.

Section 4.6 is a detailed presentation of the test program, which was conducted to obtain data for evaluating the analytical approach. An existing inducer design as a referee unit was built and tested in water and hydrogen at speeds of 8,000 to 30,000 rpm. The test facility instrumentation and procedures are described, and the test data is presented.

Section 4.7 presents and discusses the theoretical and experimental results. These results of the quasi three-dimensional solution of the inducer flow field are presented for incompressible flow of water, liquid hydrogen, liquid oxygen, and RP-1. Two-phase solutions were also obtained in the leading portion of the inducer blading. The test results are presented and discussed in view of the theoretical understanding gained in the work of the previous sections.

3.0 CONCLUSIONS AND RECOMMENDATIONS

A flow model has been developed for describing inducer performance variations due to cavitation and other effects. An approximate or quasi three-dimensional solution of this model has been programmed and run on a digital computer. It describes the inducer flow field and its variations when pumping water, liquid hydrogen, liquid oxygen, and RP-1. Further work is required to improve the compressible iteration loop of this program. A three-dimensional method of solving the flow model has been developed to take into account the effects of secondary flows within the inducer as well as to obtain a more exact solution. This also has been programmed on the computer, but needs further numerical analysis before a solution can be achieved.

As discussed in Section 4.6.6, the test vehicle and equipment operated satisfactorily. Over ten hours continuous running time was accumulated in the water loop. During the cryogenic test series, 6200 gallons (3720 lb) of liquid hydrogen was expended to produce usable data runs of approximately thirty minutes total running time. Over 35,000 gallons of liquid hydrogen were circulated through the loop.

While the inlet and discharge probes produced usable data during the water tests, this instrumentation limited the cryogenic results. The failure of the discharge probe actuator precluded attempting a 40,000 rpm liquid hydrogen test run. Prior to any additional testing, this equipment should be modified to improve its application to the test vehicle and to permit the obtaining of more extensive flow survey data.

Scale and different fluid effects have been considered by dimensional analysis and study of the thermodynamics of vaporizing liquids. The requirements for similarity in a homogeneous, equilibrium flow have been obtained, and it has been shown that the effects of departure from such similarity (variation of the parameters) can be described by the computer solution of the flow model. These studies have led to some one-dimensional analysis of the vaporizing or two-phase flow, which in turn shows the type of design criteria that are required to obtain an optimum inducer geometry. Correlation of this with the test results and further work in this area is necessary to develop a set of criteria that are adequate for an ideal theoretical design.

4.0 TECHNICAL STUDIES AND PROCEDURES

4.1 INDUCER FLUID MECHANICS AND THERMODYNAMICS (THE FLOW MODEL)

4.1.1 Basic Flow Relations

Because inducers must operate in fluids which have pressures that are not always greater than the vapor pressure, a model that accounts for vaporization (cavitation) is required for adequate theoretical treatment of the fluid motion. To obtain information about performance of various blading configurations in a reasonable length of calculation time, a continuum method of describing the flow is required. Otherwise, one must use distinct cavity analysis, which must generally be applied to special cases of tractable geometrical arrangements and which in their present classical form do not take into account the thermodynamic effects of fluid vaporization.^{2,3} The simplest concept for describing the continuum appears to be one which treats the fluid as incompressible when the local state conditions indicate that it is liquid and as a compressible, homogeneous "cloud" of liquid and vapor when a quality mixture is indicated by these local state properties. In the work now being presented, this arrangement was employed with the assumption that available equilibrium thermodynamic relationships for fluid properties are applicable. As is generally done in turbomachinery analysis, heat transfer was neglected; however, friction and diffusion losses, which have considerable influence on such motion, were taken into account.

The equations used were for steady, adiabatic fluid motions in a rotating reference frame whose axis of rotation and angular velocity are respectively coincident with those of the inducer. For analysis in a fixed, inertial reference frame, it was necessary only to set the angular velocity equal to zero and to regard the relative fluid streamlines and velocity W as absolute. The equations are given as follows⁴:

Continuity

$$\vec{W} \cdot \nabla \rho + \rho \nabla \cdot \vec{W} = 0^{(*)} \quad (4.1.1-1)$$

Motion

$$\frac{g_0 \nabla p}{\rho} = \Omega^2 \vec{r} - (\vec{W} \cdot \nabla) \vec{W} - 2 \vec{\Omega} \times \vec{W} - \vec{F} \quad (4.1.1-2)$$

Energy (along streamlines)

$$g_0 dh = d\left(\frac{\Omega^2 r^2}{2}\right) - d\left(\frac{W^2}{2}\right) \quad (4.1.1-3)$$

where h is defined in equation (4.1.1-6).

(*) Symbols used throughout are defined in Appendix A.



State

$$\rho = \rho(p, s) \quad (4.1.1-4)$$

This system of equations must be solved to obtain a solution of the flow. The term \vec{F} in the motion equation (4.1.1-2) is the frictional force per unit mass experienced by the fluid because of velocity changes in the field. Since this vector is always in a direction tangent to the streamline (i.e., parallel to the streamline direction), and since the vector equation (4.1.1-2) has three component equations, we may write one of them for the streamline direction as follows:

$$\frac{g_0}{\rho} dp = d\left(\frac{\Omega^2 r^2}{2}\right) - d\left(\frac{W^2}{2}\right) - F d\lambda \quad (4.1.1-5)$$

where the last term is the work done against friction as a particle moves through a distance $d\lambda$ along the streamline. Here, the concept of energy will be noted, and since we have the three definitions

$$h = u + p v \quad (4.1.1-6)$$

$$T ds = du + p dv \quad (4.1.1-7)$$

$$\rho = \frac{1}{v} \quad (4.1.1-8)$$

the energy equation (4.1.1-3) may be rewritten as

$$\frac{g_0}{\rho} dp = d\left(\frac{\Omega^2 r^2}{2}\right) - d\left(\frac{W^2}{2}\right) - g_0 T ds \quad (4.1.1-9)$$

From equations (4.1.1-5) and (4.1.1-9) we see that

$$F d\lambda = g_0 T ds \quad (4.1.1-10)$$

Since we have assumed zero heat transfer, the work $F d\lambda$ is a loss of available energy. We may then define the loss⁵:

$$dL = g_0 T ds \quad (4.1.1-11)$$

Thus the energy equation (4.1.1-3) and the streamline component equation of motion (4.1.1-5) may be given by

$$\frac{g_0 dp}{\rho} = d\left(\frac{\Omega^2 r^2}{2}\right) - d\left(\frac{W^2}{2}\right) - dL \quad (4.1.1-12)$$

and the vector equation of motion becomes

$$\frac{g_0 \nabla p}{\rho} = \Omega^2 \vec{r} - (\vec{W} \cdot \nabla) \vec{W} - 2 \vec{\Omega} \times \vec{r} - \left(\frac{dL}{d\lambda}\right) \frac{\vec{W}}{|\vec{W}|} \quad (4.1.1-13)$$

from which the other two required component equations of motion can be obtained.

4.1.2 The Equation of State

As shown in equation (4.1.1-4), the problem of determining the state of the fluid is solved by finding one property, in this case the density (or specific volume), as a function of two other properties; viz., pressure and entropy. Since we are dealing with the possibility of a mixture of liquid and gaseous phases, let us examine the process to which a typical fluid particle is subjected in an inducer. Figure 4.1.2-1 shows the process beginning in the liquid state at the inducer inlet (point 1). Point 1 could also be in the quality state. As the pressure drops due to inlet losses, blade blockage, etc., the fluid reaches the saturated liquid condition at the point marked "sat". Further pressure drops take the fluid to successive points g in the quality region. Then as the pressure rises, the fluid becomes a liquid and leaves the inducer at the higher pressure of point 2.

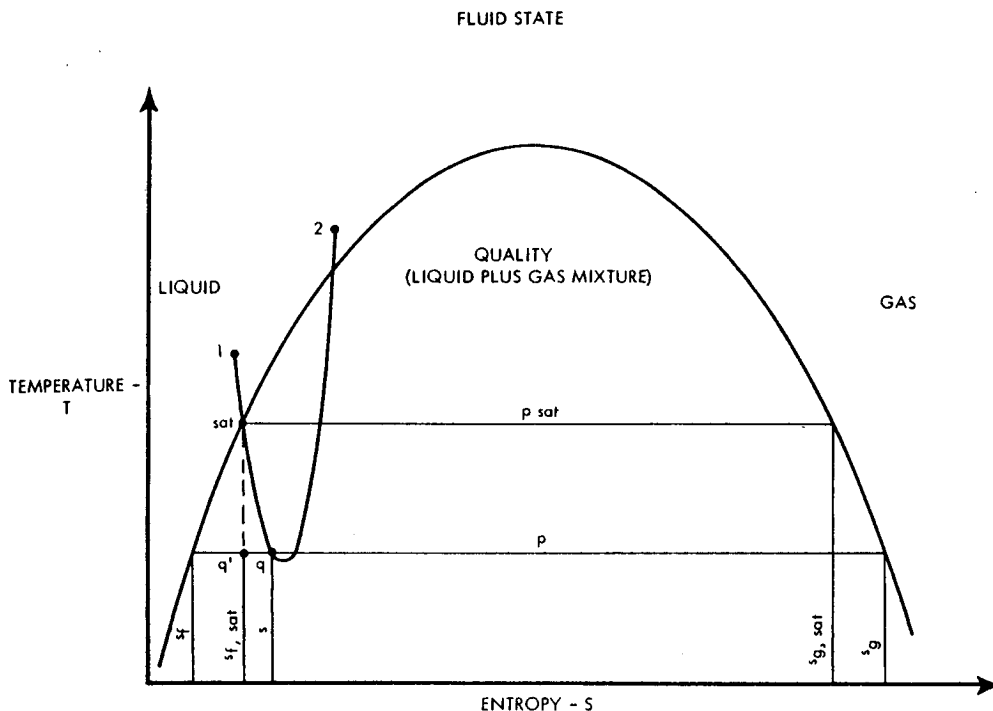


FIGURE 4.1.2-1



Pressure variations in inducers produce negligible density changes in liquid, and temperature changes that occur also result in very small density variations. Thus the liquid density (ρ_f or ρ_{sat}) is regarded as constant over the entire range of inducer fluid temperatures and pressures. Order-of-magnitude checks show that the highest-head, lowest-efficiency inducers produce values of loss L that result in small liquid temperature changes. For example, a 50% efficient, 700 ft/sec (blade tip speed) inducer with a head co-efficient

$$\psi = \frac{P_2 - P_1}{\rho_f U_{t,2}^2} = 0.1$$

has a value for $\int T ds$, from equation (4.1.1-11), of approximately 2 Btu/lbm. For the lowest operating temperatures (e.g., those of liquid hydrogen), $\Delta S = 0.06$ Btu/lbm-°R. The relation between state properties⁶ for liquid hydrogen dictates a corresponding temperature rise of 0.5 °R. Now it takes a temperature change of 5 °R at constant pressure to produce a 1% change in the specific volume of the liquid.)

For the quality region, the specific volume at the general point g is

(4.1.2-1)

$$v = v_f + x (v_g - v_f)$$

or, with equation (4.1.1-8), the density is

$$\rho = \rho_f \left[\frac{1}{1 + x \left(\frac{\rho_f}{\rho_g} - 1 \right)} \right] \quad (4.1.2-2)$$

where (see Figure 4.1.2-1),

$$x = \frac{s - s_f}{s_g - s_f} \quad (4.1.2-3)$$

For small entropy changes in the vaporization process, we may substitute for x at point g its value at point g' :

$$x = \frac{s_{f,sat} - s_f}{s_g - s_f} \quad (4.1.2-4)$$

That entropy changes are indeed small, insofar as their effect on the two-phase fluid density is concerned, may be seen as follows:

$$dv = \left(\frac{\partial v}{\partial p} \right)_s dp + \left(\frac{\partial v}{\partial s} \right)_p ds \quad (4.1.2-5)$$

$$(v = \frac{1}{\rho})$$

Checks similar to the one discussed above for the effects of entropy change on the incompressible density have revealed that the effects of the last term in equation (4.1.2-5) are of second order and may be neglected. Thus, for purposes of determining the state (density) of the fluid only, the movement in the quality region of the temperature-entropy diagram (Figure 4.1.2-1) is isentropic between the point sat and all other two-phase points. The value of p_{sat} is a function of the liquid temperature and is an input to the analysis. For reasons discussed above, when the pressure is greater than p_{sat} , neither entropy nor pressure are assumed to have any effect on the liquid density. Thus the two-phase fluid is barotropic (a function of pressure only), and equation (4.1.1-4) may be simplified to read,

$$\rho = \rho(p) \quad (p \leq p_{sat}) \quad (4.1.2-6)$$

The specific form of equation (4.1.2-6) is a combination of equations (4.1.2-2) and (4.1.2-4). However, the quality X (see equation (4.1.2-4) and Figure 4.1.2-1) may be written as follows for small values of $(p_{sat} - p)$:

$$X = \left(\frac{ds_f}{dp} \right)_{sat} \frac{(p_{sat} - p)}{s_{fg, sat}} \quad (4.1.2-7)$$

Now we can assume that $(p_{sat} - p)$ is always small enough for equation (4.1.2-7) to be applicable, since the quality X is still very low, even when the mixture density becomes quite small as compared to the liquid density ρ . Thus we may write equation (4.1.2-2) as follows:

$$\rho = \rho_f \left[\frac{1}{1 + \mathcal{J} (p_{sat} - p)} \right] \quad (4.1.2-8)$$

where

$$\mathcal{J} \equiv \left[\frac{ds_f}{dp} \frac{\left(\frac{\rho_f}{\rho_g} - 1 \right)}{s_{fg}} \right]_{sat}, (p < p_{sat}) \quad (4.1.2-9)$$

for the two-phase fluid. (The variations of \mathcal{J} with p could also be taken into account if desired). When \mathcal{J} is small (e.g., 0.00145 ft²/lbf in 20°K liquid hydrogen compared to 15 ft²/lbf in 80°F water), ρ is not so greatly reduced for a given $(p_{sat} - p)$. Thus a reasonably homogeneous two-phase flow over a wide range of pressure conditions may be expected to exist in liquid hydrogen. (Visual observations tend to confirm this assumption.) For single phase liquid, we have

$$\rho = \rho_f \quad (p \geq p_{sat}) \quad (4.1.2-10)$$



So, the state of the fluid as required by equation (4.1.1-4) is described by equations (4.1.2-8) and (4.1.2-10). When combined the other equations of the motion, this forms the basis for a reasonable description of the inducer flow field and for a whole range of one-dimensional, homogeneous, two-phase, duct flow studies, as reported in subsequent parts of this report.

4.1.3 Losses

A method of treating the losses that occur in an inducer and the variations in them that are caused by the presence of bubbles in different amounts are included in the flow model. The basic assumptions of this work prohibit heat transfer across streamlines and require an essentially continuum flow field in thermal equilibrium. In such a flow, bubbles are many and small and it is possible that the actual formation and dilation of these bubbles is reversible. Even if such is not the case, the amount of the mass affected by bubble formation is quite small. The energy added per unit mass is also small since bubbles exist primarily in the inlet regions of the inducer. (In this connection it was found that the rate of entropy increase due to heat transfer into and out of a bubble can be estimated with a knowledge of an average bubble radius r_b . This allowed a check of the loss, at least on an order-of-magnitude basis. The check was made for both hydrogen and water, and it justified the neglect of this loss.) However, the presence of the bubbles causes increased velocities in the channels and higher skin friction losses. Also their presence and eventual collapse downstream leads to larger relative velocity decelerations and greater diffusion or separation losses than those that occur when no bubbles are present.

Therefore, it was decided to neglect the bubble formation heat transfer and dilation losses (which can occur only in the absence of thermal equilibrium), and to treat the friction and diffusion losses as primary. Since the flow field is turbulent, no practical solution of the complete Navier-Stokes equations is possible. Because of the rather long flow passages and turbulent motion, it is possible to assume that the momentum losses due to friction and diffusion are immediately distributed multi-dimensionally across the flow passage, or from blade to blade; i.e., mixing of the low energy fluid with the free stream occurs rapidly, the idea being somewhat analogous to fully-developed flow in a duct. This is accomplished by use of "equivalent" one-dimensional turbulent pipe and diffuser flow losses applied locally to the flow along each streamline in the inducer.

These losses are separated into two categories, the first type being the loss essentially due to zero-pressure-gradient type skin friction and the second being any loss in addition to the first type that occurs when the pressure gradient is adverse (velocity decreasing). The basic difference between these two types is that one depends on the local Reynolds number of the passage (see equation 4.1.3-6) and the other is a separation or diffusion loss independent of Reynolds number. The first type is always applied at all points, but the second occurs only when the velocity is decreasing at the point in question.

We now write the loss term of equation (4.1.1-12) as follows:

$$dL = dL_a + dL_b \quad (4.1.3-1)$$

For the first type of loss, the conventional turbulent pipe-flow relation is used; viz.,

$$dL_a = \frac{f}{D_h} \frac{W^2}{2} d\lambda \quad (4.1.3-2)$$

where the hydraulic diameter D_h is that of the flow passage or inducer channel at the station in question:

$$D_h = 4 \frac{A}{p} \quad (4.1.3-3)$$

For the inducer channel, this is given by

$$D_h = \frac{2r_t (1 - \xi)}{1 + \left(\frac{1 - \xi}{1 + \xi}\right) \frac{nb}{\pi} \sec \beta} \quad (4.1.3-4)$$

where β is a function of r .

Examination of references⁷ and consideration of surface roughness⁸ allows us to use the empirical relation for f .

$$f = 0.00714 + \frac{0.6104}{(R)^{0.35}} \quad (4.1.3-5)$$

where

$$R = \frac{W D_h}{\nu} \quad (4.1.3-6)$$

and ν is the liquid kinematic viscosity.

The second loss is obtained by assuming that the fluid is flowing (locally) in a conical diffuser of approximately the channel cross-sectional area. Incompressible flow is assumed in obtaining this equivalent diffuser in order that the equivalent cone angle obtained can be directly related to a velocity change and not a density change. The loss is expressed by

$$dL_b = -k d\left(\frac{W^2}{2}\right) \quad (4.1.3-7)$$

so that k is the amount of the local velocity head change that results in a loss. The value of k is essentially that for a conical diffuser with the skin-friction or Reynolds-number-dependent portion of the loss subtracted, since we are allowing for this in dL_a .



Examination of conical diffuser data⁹ with this in mind indicates that for the range of diffuser cone half angle ϕ with which we are concerned,

$$k = 1 - \frac{a}{a + \tan \phi} \quad (4.1.3-8)$$

where

$$\tan \phi = -\frac{1}{2} \frac{dw}{d\lambda} \sqrt{\frac{Q(f)}{\pi n_b w^3}} \quad \left(\frac{dw}{d\lambda} < 0 \right) \quad (4.1.3-9)$$

$$\tan \phi = 0 \quad \left(\frac{dw}{d\lambda} \geq 0 \right) \quad (4.1.3-10)$$

$Q(f)$ is the volume flow that results where the entire mass flowing is liquid, and "a" is a constant now equal to 4/3, this value being determined by reference to diffuser loss data.⁹

Our reasons for neglecting direct bubble formation and dilation losses have been given. However, other losses can be added if it becomes apparent that they should be included. In this area, any "on-location" losses (i.e., those which occur at given points in the machine, such as leakage across the blade tips, etc.) could be added.

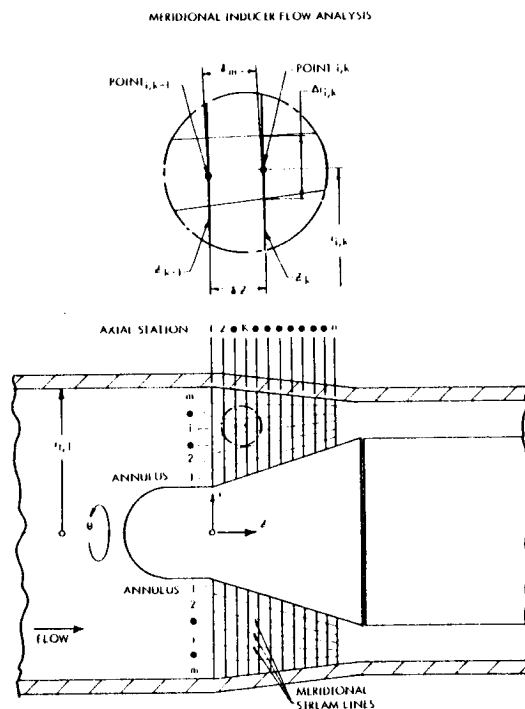
In its present form, the fluid flow model reflects the presence of vapor as long as the flow is continuum in nature. Thus we have the means for obtaining the differences in performance due to thermodynamic property variations among fluids. However, the question remains as to what constitutes deviation from this continuum concept. Primarily we can say that once bubble centrifuging across streamlines becomes paramount, the continuum concept needs either to be abandoned or approached in another way. Insofar as performance correlations between fluids having only different bubble sizes are concerned, the existing form of the flow model is not applicable. However, the present loss factors can be revised to reflect the influence of bubble size differences. It now remains to apply this in the specific areas of mathematical solution of the inducer flow field, dimensional analysis, and one-dimensional flow studies. These are described in the succeeding portions of the report.

4.2 QUASI THREE-DIMENSIONAL SOLUTION OF AXIAL INDUCER FLOW FIELD

4.2.1 Method of Analysis

To obtain the distributions of pressure and velocity at the inducer discharge as well as the values of these quantities within the rotor (both the average values and those on the blade surface), a quasi three-dimensional method of analysis has been developed. This has been programmed on a digital computer and adaptation to mixed-flow configurations is possible, although the immediate application is to a primarily axial-flow analysis.

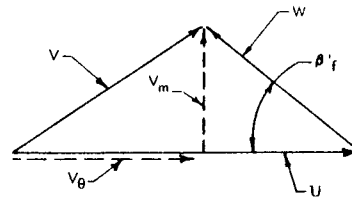
The solution is obtained by combining approximate two-dimensional analysis of an axisymmetric flow in the meridional plane (Figure 4.2.1-1) and of a blade-to-blade flow in an annulus formed by rotating two adjacent meridional streamlines about the Z axis (See Figure 4.2.1-2. The radial distributions of fluid pressure, density, saturation pressure, and meridional velocity at the blade leading edge are presently assumed constant but may be variable with some small adaptation. The flow is assumed to be restricted to the annuli, which have fixed locations at inlet, as shown in Figure 4.2.1-1. The problem is to adjust the meridional locations of these annuli as one proceeds through the machine from one axial station to the next. Because the flow is primarily axial, the major effect on the meridional solution is the blade-to-blade solution and its variation under cavitating conditions. Furthermore, shifting of the meridional streamlines is slight; therefore, to first order, no effect is assumed to be propagated upstream. This enables one to make the annulus adjustments in their entirety at each axial station so that only one pass through the machine is necessary in the analysis. However, subsequent passes could be made to provide higher-order adjustments.



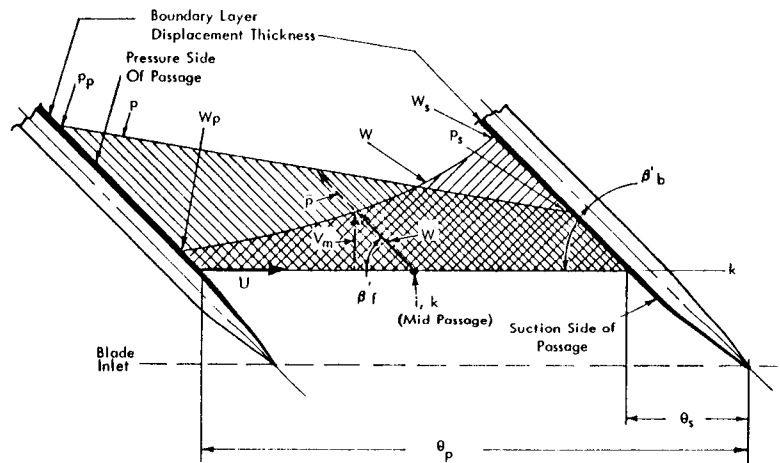
NOTE: SEE FIGURE 4.2.1-2 FOR BLADE-TO-BLADE ANALYSIS AT THE POINT i,k .

FIGURE 4.2.1-1

BLADE-TO-BLADE FLOW ANALYSIS



ANNULUS VELOCITY TRIANGLE



PRESSURE AND VELOCITY DISTRIBUTIONS

FIGURE 4.2.1-2

At each station, the average velocity triangle (Figure 4.2.1-2) for each annulus is first set up by procedures to be developed. The local pressure difference from blade to blade is then determined from the moment of momentum relation (Equation 4.2.2-7), and the pressure is assumed to vary linearly from blade to blade in the tangential direction, the one-dimensional pressure being halfway between the extremes. The state equation is then applied at several points from blade to blade to determine the attendant density distribution. Losses are taken into account only in calculating the average annulus properties; hence no loss is assumed in the tangential direction. The energy equation (Equations (4.1.1-3) and (4.2.2-9)) is used numerically in the tangential direction, starting with the average values of the properties in the middle, to give the relative velocity distribution across the passage. Now, a new average density is calculated from these distributions. This calculation is repeated for each annulus until the average density agrees closely with the preceding one that was used to set up the velocity triangle. This having been done for each annulus at the station, equilibrium in the radial direction (approximately normal to the meridional streamlines) is checked, using a simplified form of the radial equation of motion (Equation 4.2.2-10). The locations of the annuli are then adjusted as indicated by this check, and the process outlined above is repeated until the equilibrium is satisfied. This constitutes compatibility of the meridional and blade-to-blade solutions. Then one proceeds to the next station and begins again. Losses are taken into account in the calculation of the one-dimensional velocity triangles of the annuli, because the equation of motion along a streamline (4.1.1-12) is applied to average properties $\bar{\rho}$, \bar{p} , and \bar{W} of an annulus from one axial station to the next.

4.2.2 Procedure for Calculations

The solution begins with the specification of inlet state, velocities, and annulus radii r on the inducer inlet $r - \theta$ plane Z_1 (See Figure 4.2.1-1). Thus the mass flow rate \dot{m}_1 in each annulus i is fixed. The annulus radii on the next $r - \theta$ plane, Z_2 , are first assumed and the flow in each annulus at that plane is calculated according to the following steps (this same procedure is followed at the other Z planes):

- a. The continuity relation is applied first to obtain the average meridional velocity (See Figure 4.2.1-1 and 4.2.1-2).

$$V_{m,i,k} = \frac{\dot{m}_i}{\bar{\rho}_{i,k} r_{i,k} \Delta r_{i,k} (\theta_p - \theta_s)_{i,k}} \left(\frac{\delta m}{\delta z} \right)_{i,k} \quad (4.2.2-1)$$

where, for the first iteration, $\rho_{i,k} = \rho_f$ is assumed.

- b. Next the average velocity triangle (Figure 4.2.1-2) is obtained from the flow angle β_f' . This differs from the actual blade angle β_b' by the deviation angle δ . δ is empirically chosen at outlet for each annulus. To represent the blade unloading phenomenon, δ is assumed to increase rapidly from a negligible value as one proceeds through the final fraction of annulus length near outlet. Thus it is represented by

$$\delta_{i,k} = \delta_{i,n} \times \left(\frac{k}{n} \right)^6 \quad (4.2.2-2)$$

where the exponent 6 is used so that the deviation is essentially zero, except in the area of the inducer trailing edge.

The angle β_b' is found from the inducer channel co-ordinates, allowance being made for the local direction of the meridional streamline. At each axial station, the shape of the blade channel is described by polynomials of the form

$$\theta_p = \theta_p(r) \quad (4.2.2-3)$$

$$\theta_s = \theta_s(r) \quad (4.2.2-4)$$

In obtaining these relations, allowance is made for blade thickness and an assumed boundary layer displacement thickness of an equal amount δ^* on each side of the blade. This thickness is assumed to grow linearly with axial distance, approximately according to the known relation for two-dimensional, zero-pressure-gradient turbulent flow; viz.,¹⁰

$$\delta^* = K_{BL} \left(\frac{z_k - z_1}{z_n - z_1} \right) 0.0466 \frac{L^{4/5} V^{1/5}}{U_\infty^{1/5}} \quad (4.2.2-5)$$



where

$$U_{\infty} = \Omega r_{t,1} \sqrt{\frac{1 + \xi_1^2}{2}}$$

since the applicable inlet free stream relative velocity W is reasonably close to Ωr . The factor $\sqrt{\frac{1 + \xi_1^2}{2}}$ places this at the root mean square radius of the blade (between hub and tip).

$$l = \frac{z_n - z_1}{\tan \beta_{i,t}} \sqrt{\frac{1 + \xi_1^2}{2}}$$

Since l is the arc length of a straight helix on a cylinder of radius

$$r_{t,1} \sqrt{\frac{1 + \xi_1^2}{2}}$$

and axial length $z_n - z_1$, δ^* will be somewhat larger than for two-dimensional, zero-pressure-gradient, turbulent flow on the usual inducer blade for $\beta_n' > \beta_1'$. This is plausible, since an adverse pressure gradient gives larger values of δ^* than the smaller values arising from the favorable pressure gradient on the opposite side of the channel.

δ^* is assumed constant (as here defined) from hub to shroud at each z -station, z_k . K_{BL} is an empirical constant now taken equal to 1.0, but which can be increased in cases of heavy blade loadings due to the thicker boundary layers that would result. It is assumed that fluid which would contribute to the thick wakes suggested by prolonged and large adverse pressure gradients is immediately mixed with the free stream. (The resulting momentum losses are taken into account by the methods of Section 4.1).

- c. The average pressure of $\bar{p}_{i,k}$ is found from a finite difference version of of equation (4.1.1-12):

$$\frac{9_0(\bar{p}_{i,k} - \bar{p}_{i,k-1})}{(\frac{\bar{p}_{i,k-1} + \bar{p}_{i,k}}{2})} = \frac{\Omega^2}{2} (r_{i,k}^2 - r_{i,k-1}^2) - \frac{1}{2} (\bar{w}_{i,k}^2 - \bar{w}_{i,k-1}^2) - L_{i,(k-1 \text{ to } k)} \quad (4.2.2-6)$$

where $L_{i,(k-1 \text{ to } k)}$ is evaluated with finite difference forms of equations (4.1.3-1) to (4.1.3-10), if losses are desired. Otherwise the loss term is set equal to zero.

- d. The blade-to-blade solution is found by applying the tangential component equation of motion in a finite difference form which can be derived directly from it or from the application of the moment of momentum relation to the fluid in the annulus between the blades¹¹:

$$\frac{g_0(p_p - p_s)_{i,k}}{\bar{\rho}_{i,k}} = (\theta_p - \theta_s)_{i,k} V_{m,i,k} \left(\frac{r_k V_{\theta,k} - r_{k-1} V_{\theta,k-1}}{\delta m_k} \right) \quad (4.2.2-7)$$

At this point, four assumptions are made to simplify the calculations. First, the pressures p_p and p_s obtained from this calculation are assumed to exist on the plane z_k . Second, the average pressure from equation (4.2.2-6) is assumed to exist at mid-passage (half-way from one blade to the next). Next, a linear blade-to-blade pressure \bar{p} distribution is assumed as follows (Figure 4.2.1-2):

$$p = p_s + K_1 (\theta - \theta_s) \quad (4.2.2-8)$$

where K_1 is a constant. Further, with the fact that the total enthalpy is constant from blade-to-blade in a given annulus at a given radius, the entropy is assumed constant over the same area. (Although we are not regarding entropy from the standpoint of its effect on the fluid state (see equation 4.1.2-6), any differences in entropy from one station to another do affect the available energy or total pressure.) Thus we obtain an energy relation that holds from blade to blade at constant radius:

$$g_0 \frac{dp}{\rho} = -d\left(\frac{W^2}{2}\right) \quad (4.2.2-9)$$

This is obtained from equation (4.1.1-9). Thus equation (4.2.2-9) yields the relative velocity distribution W from blade to blade, with the density being determined by the pressure, from equations (4.1.2-8) to (4.1.2-10). Further remarks will be made about this blade to blade solution in Section 4.2.3.

- e. The θ - averaged density $\bar{\rho}$ is next found from the above results.
- f. Since the initial choice of $\bar{\rho}_{i,k}$ in equation (4.2.2-1) is the largest possible value, ρ_f , the average $\bar{\rho}$ of the (e) will be smaller. Thus it is necessary only to reduce the value of $\bar{\rho}_{i,k}$ to a value less than ρ_f , and repeat steps (a) through (e) above. This procedure is followed until the $\bar{\rho}$ from step (e) agrees closely with the assumed value of $\bar{\rho}_{i,k}$ in step (a).

Thus far, the flow from blade to blade in the given annulus at a particular radial and axial station is solved. It remains to be determined that all the annuli so solved at a given axial station in the inducer are in radial equilibrium.

- g. The radial locations (r_i) of the annuli are adjusted to provide conform-
ance of the resulting field to the following relation:

$$\frac{g_0}{\bar{\rho}} \frac{d\bar{p}}{dr} = \frac{V_{\theta}^2}{r} \quad (4.2.2-10)$$

This equation is obtained from equation (4.3.2-22) by assuming that radial accelerations of the fluid and the radial component of the friction forces (which are expressed in the loss term) are negligible. This amounts to the neglect of the effects of (1) meridional streamline curvature, (2) the variation of the radial component of the meridional velocity V_m , and (3) the radial component of the blade forces. The annulus radius adjustments are made in accordance with iteration procedures outlined in Section 4.2.4. Each time such an adjustment is made, the annulus flow at each affected station i, k is recalculated, following steps (a) through (e).

- h. Upon completion of steps (a) through (g) at each axial station z_k , the same procedure is followed at the next station z_{k+1} , the calculation at the outlet plane z_n completing the solution of the flow field.
- i. Finally, calculations of power and efficiency are made as follows: The shaft power input to the fluid is

$$P_S = \frac{\Omega}{g_0} \sum_{i=1}^m w_i (r_n V_{\theta, n} - r_i V_{\theta, i}) \quad (4.2.2-11)$$

and the efficiency is

$$\eta = \frac{P_H}{P_S} = \frac{\left(\sum_{i=1}^m w_i \right) \frac{\Delta P_{ave}}{\rho_f}}{P_S} \quad (4.2.2-12)$$

where ΔP_{ave} is the mass-averaged total pressure rise of the fluid in the inducer.

4.2.3 Blade-to-Blade Solution

The current method of obtaining the blade-to-blade flow field is outlined above. However, the question arises as to how well this method represents the actual flow pattern. Aside from the fact the the resulting density and velocity distributions should satisfy continuity, it is also necessary that they be reasonable when both single and two-phase flows exist from blade to blade. Two approaches have been considered, and they cover most of the possibilities for a practical description of such a flow. The first incorporates a linear distribution of pressure versus angle of rotation θ (as used in Section 4.2.2), with the assumption that the mean pressure \bar{p} and one-dimensional relative velocity \bar{W} lie in the middle of the passage¹² (see Figure 4.2.3-1). The second has a linear \bar{W} distribution with θ , and no assumption regarding the location of the mean values (see Figure 4.2.3-2). Both methods assume the flow direction given by the angle β_f'

at all points from blade to blade, and both assume constant entropy (or constant available energy) from blade to blade, at constant radius r . Remarks about the applicability and utilization of each method follow.

The mean value assumptions used with the linear pressure method eliminate the need for checking the resulting velocity and density distributions for blade-to-blade continuity. This does not mean that blade-to-blade continuity is necessarily satisfied; however, the calculation is straight-forward and leads, by the few simple steps previously outlined, to a blade-to-blade solution. (See equations (4.2.2-8) and (4.2.2-9)). Figure 4.2.3-1, however, qualitatively illustrates the shortcomings of this method if it must describe the flow that results when a change of phase occurs somewhere between the blades. Apart from the continuity question, one observes a reasonable distribution of pressure and velocity in the liquid region; but the two-phase region appears to have unrealistic pressures, densities, and velocities. In fact, one would expect to find very little change of pressure in a vaporous area. This imposed pressure variation produces excessive velocities (which in an actual machine could even be in the opposite direction) and a sudden decrease of density to an essentially zero value in that region. Because of this density behavior, the resulting solution is not very sensitive to \mathcal{J} in the equation of state (4.1.2-8) that varies from one fluid to another. Nevertheless, this linear pressure method does show the blade loading shift that occurs away from the upstream portions of an inducer when the fluid vaporizes.

In view of the above discussion, Figure 4.2.3-2 provides a very reasonable qualitative variation of properties from blade-to-blade for an average flow situation that is similar to that of Figure 4.2.3-1. Here, the linear relative velocity \bar{W} distribution gives rise to what may be expected to be a more realistic pressure variation in the two-phase region. Since this pressure drops only slightly below saturation, the resulting density decrease is less severe than in the previous case. Thus the fluid thermodynamic properties (expressed by \mathcal{J}) have a larger effect on the solution of the flow field. Established approximate methods¹³ assume the mean value of velocity \bar{W} to be halfway between the values \bar{W}_S and \bar{W}_P (at the suction and pressure sides of the channel respectively) and, therefore, at mid-passage. Such an assumption is strictly correct only for incompressible flow; and when the change to two-phase flow occurs somewhere across the passage, the mid-passage velocity will not necessarily be representative of all the fluid flowing in the passage. Hence the problem is not as simple as it appears in the linear pressure method. (If the mean values are assumed to exist at mid-passage, the calculation is nearly as simple as with the linear pressure method.) The equations for this blade-to-blade solution are:

Velocity distribution

$$W = W_S + K_2 (\theta - \theta_S) \quad (4.2.3-1)$$

Energy (from equation (4.2.2-9))

$$dp = \left(\frac{-\rho W}{g_o} \right) dW \quad (4.2.3-2)$$

ANALYSIS FOR LINEAR BLADE-TO-BLADE PRESSURE DISTRIBUTION

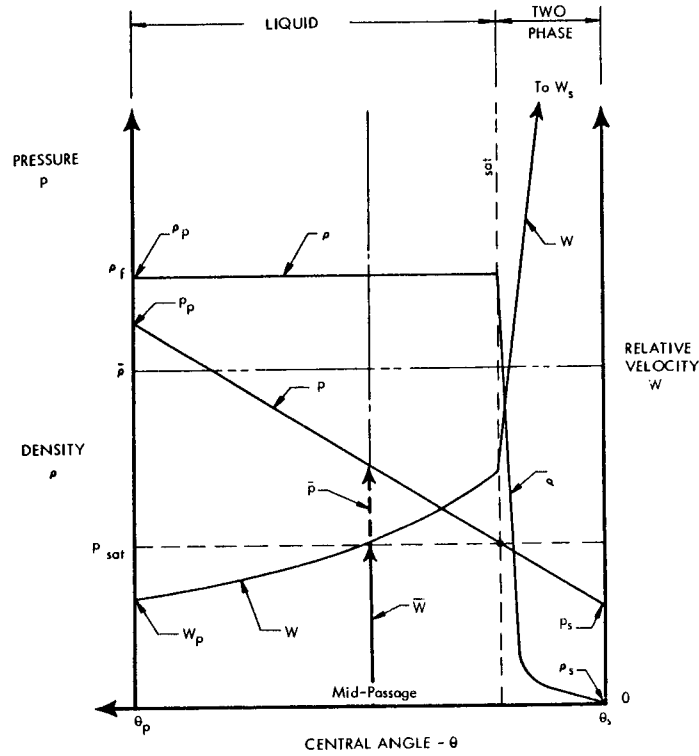


FIGURE 4.2.3-1

ANALYSIS FOR LINEAR BLADE-TO-BLADE RELATIVE VELOCITY DISTRIBUTION

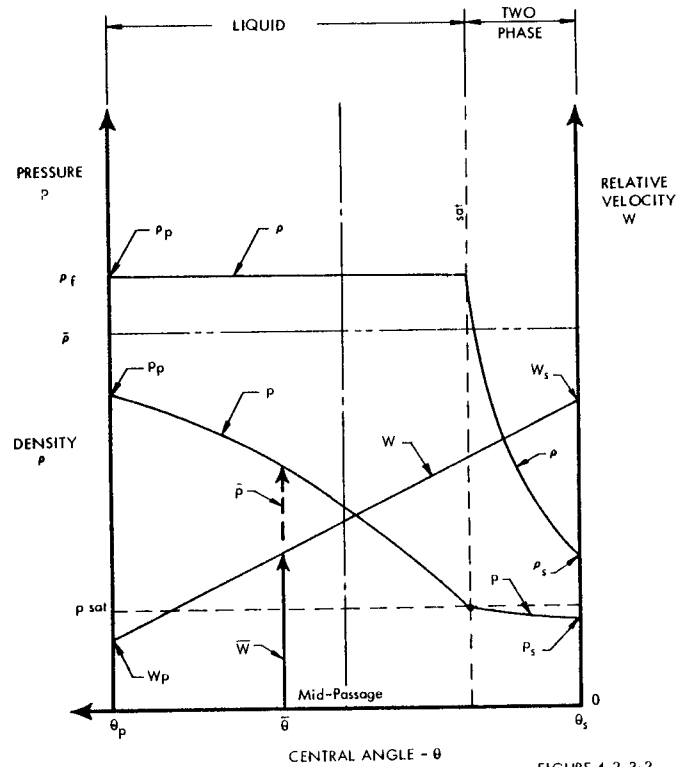


FIGURE 4.2.3-2

Continuity (in the annulus)

$$\int_{\theta_s}^{\theta_p} \rho W d\theta = (\theta_p - \theta_s) \bar{\rho} \bar{W} \quad (4.2.3-3)$$

State (equations (4.1.2-8) and (4.1.2-10))

$$\left. \begin{aligned} \rho &= \rho_f \quad (p \geq p_{sat}) \\ \rho &= \rho_f \left[\frac{1}{1 + f(p_{sat} - p)} \right] \quad (p \leq p_{sat}) \end{aligned} \right\} \quad (4.2.3-4)$$

Moment of momentum (from equation 4.2.2-7)

$$(p_p - p_s) = (\theta_p - \theta_s) \frac{\bar{\rho}}{g_0} V_m \frac{d(rV_\theta)}{dm} \quad (4.2.3-5)$$

Kinematics

$$\bar{W} \sin \beta_f' = V_m \quad (4.2.3-6)$$

Now equations (4.2.3-1) to (4.2.3-3) lead to

$$p_p - p_s = (W_s - W_p) \frac{\bar{\rho}}{g_0} \bar{W} \quad (4.2.3-7)$$

and equations (4.2.3-1), (4.2.3-5), (4.2.3-6), and (4.2.3-7) give

$$\frac{W_s - W_p}{\theta_p - \theta_s} = -K_2 = \sin \beta_f' \frac{d(rV_\theta)}{dm} \quad (4.2.3-8)$$

Also, as in equation (4.2.3-1),

$$W = \bar{W} + K_2 (\theta - \bar{\theta}) \quad (4.2.3-9)$$

To solve for the resulting distributions, one first finds K_2 from equation (4.2.3-8), after steps (a), (b), and (c) of Section 4.2.2 have been accomplished. Then one must perform an iteration using equations (4.2.3-2), (4.2.3-3), and (4.2.3-4) with (4.2.3-9) to obtain the correct $\bar{\theta}$. Then the calculation proceeds with the iteration of $\bar{\rho}$ as in Section 4.2.2 to obtain the blade-to-blade solution. The complication that arises in performing this additional iteration for $\bar{\theta}$, which is nested within the $\bar{\rho}$ iteration, is the reason that this linear velocity method is not currently employed. Further study is required to obtain a workable iteration which, like the others, must avoid the problems that arise due to the density discontinuity at the point of phase change in the passage. An initial future step, however, would be to assume $\bar{\theta}$ to be in the middle of the passage throughout the calculations. This should give a description of the flow that shows an improvement over that of the linear pressure method. It has been pointed out that a linear \bar{W} distribution provides results that are in close agreement with more nearly correct answers, in single-



phase flow¹³. Although exception is taken to the applicability of such results to the regions near the leading and trailing edges, we may state that light leading edge loading due to cavitation, and efforts to simulate the blade unloading phenomenon by assuming deviation angle distributions as one approaches outlet, are reasons for accepting these results.

4.2.4 Mathematical Methods for Solution

The problem of finding the correct location of the meridional streamlines introduces some iterative problems. We must solve the radial equilibrium equation (4.2.2-10)

$$\frac{\partial \bar{p}}{\partial r} = \frac{\rho}{g_0} \frac{\bar{V}_\theta^2}{r}$$

where, if we denote differentiation along a streamline by d ,

$$d\bar{p} = \frac{\rho}{g_0} \left[d \left(\frac{\bar{W}^2 - \Omega^2 r^2}{2} \right) + dL \right] \quad (\text{Motion Equation})$$

dL is the streamline loss term as defined before

$$\bar{W} = V_m / \sin \beta'$$

$$V_\theta = \Omega r - V_m / \tan \beta' = \Omega r - \bar{W} \cos \beta'$$

β' is a one dimensional flow angle and V_m is calculated from a one-dimensional continuity equation.

To describe the finite difference scheme constructed to solve this problem, consider two radially adjacent annuli numbered i and $i+1$ (see Figure 4.2.4-1). The one-dimensional mean velocities are calculated as

$$\bar{W}_i = V_{m_i} / \sin \beta'_i$$

$$V_\theta = \Omega r_i - V_{m_i} / \tan \beta'_i$$

where θ and V_θ are defined as positive in a direction opposite to $\vec{\Omega} \times \vec{r}$.

V_{m_i} is the meridional velocity as given by equation (4.2.2-1) and the static pressure p_i is calculated as in equation (4.2.2-6). Analogous velocities and pressure are calculated for $i+1$. A measure of the radial imbalance between the two annuli is now calculated by

$$Q = \frac{\bar{p}_{i+1} - p_i}{r_{i+1} - r_i} - \frac{1}{2} \left(\frac{\bar{p}_i}{g_0} \frac{V_{\theta_i}^2}{r_i} + \frac{\bar{p}_{i+1}}{g_0} \frac{V_{\theta_{i+1}}^2}{r_{i+1}} \right) \quad (4.2.4-1)$$

which is a finite difference analogue of equation (4.2.2-10).

AXIAL VIEW OF TWO RADially ADJACENT ANNULI

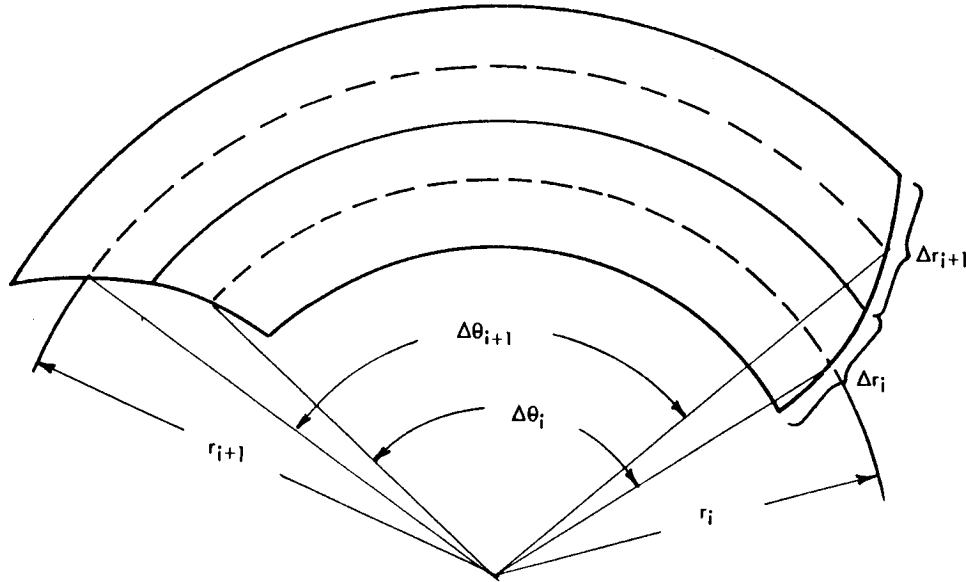


FIGURE 4.2.4-1

The scheme for reducing the numerical value of R is based on Newton's method for estimating the zeros of a function (See Figure 4.2.4-2). To accomplish this, a small perturbation, α , is introduced and the residual R is recalculated. That is V_m , \bar{W} , V_θ , dL , and \bar{p} are recalculated with r_i replaced by $(r_i + \alpha)$, r_{i+1} replaced by $(r_{i+1} + \alpha)$, Δr_i replaced by $(\Delta r_i + 2\alpha)$, and Δr_{i+1} replaced by $(\Delta r_{i+1} - 2\alpha)$. Note that this merely moves the boundary between annuli i and $(i + 1)$ by an amount 2α without altering the lower boundary of annulus i or the upper one of annulus $(i + 1)$. Denoting this perturbed value of R by R' , one can write the first order approximation

$$\frac{dR}{dr_i} = \frac{R' - R}{(r_i + \alpha) - r_i} = \frac{R' - R}{\alpha}$$

This enables one to calculate an adjustment δr of r_i , which will tend to reduce the numerical value of R , by writing

$$\delta r = -R' / \frac{dR}{dr_i} = \frac{-R' \alpha}{R' - R}$$

which is equivalent to the proportion

$$\delta r / \alpha = R' / (R - R')$$

This formula is illustrated geometrically in Figure 4.2.4-2.



HYPOTHETICAL RESIDUAL VS RADIUS CURVE

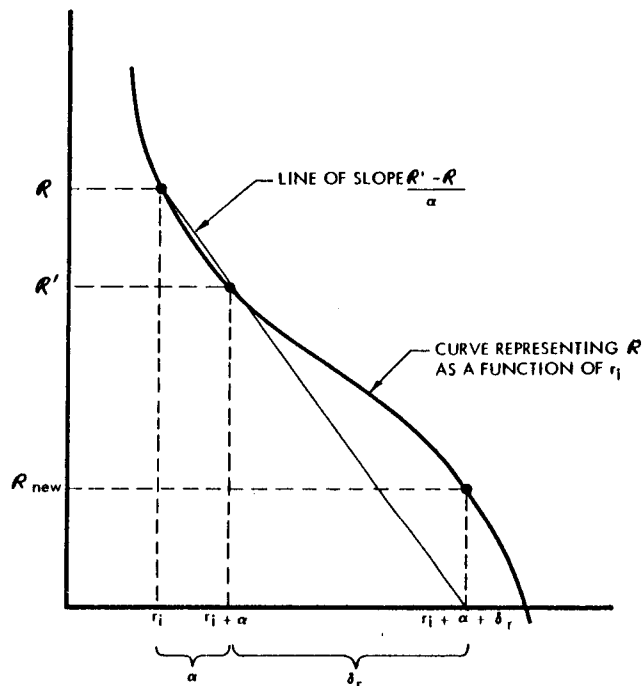


FIGURE 4.2.4-2

(Note that $(r_i + \alpha + \delta r)$ corresponds to R_{new} , a lower value than the original R).

Thus it is indicated that a further adjustment of the common boundary by an amount $2\delta r$ will reduce the numerical value of the radial imbalance between the two annuli. This adjustment having been made, the velocities, pressures, and densities are recalculated in annuli (i), (i + 1), and, if $i \geq 2$, annulus (i - 1). The new values of the three (or two) affected residuals are calculated and a search is made for the pair of annuli now displaying the numerically largest residual for that axial station. The common boundary of these two annuli is then adjusted by the scheme described above. The search continues until the numerical value of the largest residual meets some smallness criterion.

To derive such a smallness criterion, we compared the residual to the total pressure rise of the inducer, divided by the inlet tip radius, and required that

$$|R| \leq \epsilon' \frac{P_2 - P_1}{r_{i,t}} \quad (4.2.4-2)$$

be satisfied. ϵ' is a number expressing the percentage of the term $(P_2 - P_1)/r_{i,t}$, which we will allow as a deviation from radial equilibrium, expressed by R in Equation (4.2.4-1).

When the total pressure rise coefficient

$$\psi = \frac{P_2 - P_1}{\frac{\rho_f}{g_0} U_{1,t}^2} \quad (*)$$

is substituted, Equation (4.2.4-2), takes the form

$$|R| \leq \epsilon' \psi \frac{\rho_f}{g_0} U_{1,t}^2$$

Since the expected performance of an inducer gives some numerical estimate of ψ , we write

$\epsilon = \epsilon' \psi$ and have

$$|R| \leq \epsilon \frac{\rho_f}{g_0} \frac{U_{1,t}^2}{r_{1,t}} \quad (4.2.4-3)$$

as an accuracy criterion to be satisfied.

4.2.5 Results and Applicability to Design Methods

This quasi three-dimensional solution of the flow field has been run for water, liquid oxygen, liquid hydrogen, and RP-1 in an experimental inducer. The results are presented in Section 4.7.

The approximate method of solution has further value as a logical step in an inducer design program. The design criteria (e.g., in the form of desired pressure or velocity distributions) are not known exactly throughout the machine. It is possible to specify these distributions somewhat arbitrarily and to require conformance of the resulting design by monitoring the calculation with the three-dimensional program, which would be slightly adapted for design use. This approach undoubtedly would yield very complicated blade shapes and numbers that would need to be compromised and re-analyzed. Thus the practical design approach appears to be one which combines certain elementary types of blade elements with specified pressure or velocity distributions; e.g., along hub and shroud only. Therefore the problem of designing an inducer suggests the use of an advanced, design version of the more rapid and approximate type of solution.

However, in its present form as an analysis program, the quasi three-dimensional solution can be used in a step-by-step design procedure as follows:

(*) For a discussion of the nondimensionalization process, see Section 4.4.2.



- a. Specify channel shape
- b. Compute distributions of fluid properties and compare with design criteria
- c. Modify channel shape
- d. Repeat steps (b) and (c) until a satisfactory design is obtained.

4.3 THREE-DIMENSIONAL SOLUTION OF INDUCER FLOW FIELD

4.3.1 General Discussion

The equations of the flow model have been applied to the problem of solving the inducer flow field in three-dimensions. This method of solution takes into account the secondary or corkscrew motion in the passages. Such flows may be of importance in the case of vaporizing liquids, although three-dimensional studies of single-phase fluids have shown that these flows may be neglected¹². Also a complete three-dimensional solution, through the application of boundary conditions that must be employed to obtain a result, calculates such things as blade leading edge velocity and pressure distributions, outlet deviation angles, and upstream effects of downstream shifts of the flow field.

Because an inducer analysis must include losses and two-phase fluid effects, the classic method of a three-dimensional solution via a single variable, the velocity potential, is not possible. The method used follows streamlines for simplicity in specifying and keeping account of losses. (In this way, an equation of state that accounts for entropy changes could be employed.) At a chosen value of the axial co-ordinate Ξ , the equations are solved simultaneously in three unknowns; viz., the other two co-ordinates of the streamline and the velocity thereon. The method employs the same type of description of the channel boundaries as is used in Section 4.2. The mathematical methods and details for obtaining this three-dimensional solution follow.

4.3.2 Mathematical Methods for Three-Dimensional Solution of the Flow Model

4.3.2.1 Introduction

The generalized method of solving the flow model three-dimensionally can briefly be described as a solution of the system consisting of the three components of the vector motion equation, subject to restrictions of the state and continuity equations (see Section 4.1.1).

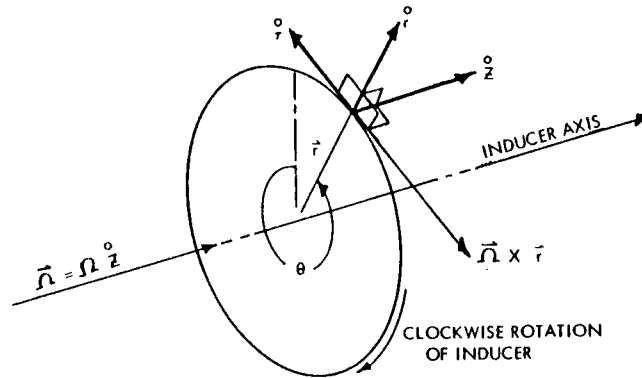
Before discussing the details of this method, we present the rotating (relative to the fixed, or absolute, frame) cylindrical coordinate system which was chosen for the resolution of the vector motion equation.

The orthonormal triad ($\hat{r}^o : \hat{z}^o : \hat{t}^o$) is defined as follows (see Figure 4.3.2-1):

$\hat{r}^o \equiv$ radial unit vector

$\hat{z}^o \equiv$ axial unit vector (pointing from inlet toward outlet
of inducer for clockwise rotation)

$\hat{t}^o \equiv -\frac{\vec{\Omega} \times \vec{r}}{\Omega r}$ tangential unit vector opposed to direction of rotation.



THE ORTHONORMAL TRIAD ($\hat{r} : \hat{z} : \hat{r} \times \hat{z}$)

FIGURE 4.3.2-1

This direction for \hat{z} was chosen for convenience and it is important to note that the angle θ will be measured in this direction (counterclockwise).

The basic equations are:

Motion: $\vec{a} + \frac{g_0}{\rho} \nabla p + \vec{F} = 0$ (4.3.2-1)

where \vec{a} is the absolute fluid acceleration and \vec{F} is a friction force vector (see equations (4.1.1-10), and (4.1.1-11)).

Continuity: $\nabla \cdot (\rho \vec{w}) = 0$ (4.3.2-2)

where \vec{w} is relative fluid velocity.

State:

$$\rho = \begin{cases} \rho_f & \text{if } p \geq p_{sat} \\ \frac{\rho_f}{1 + f(p_{sat} - p)} & \text{if } p < p_{sat} \end{cases} \quad (4.3.2-3)$$

(see Section 4.1.2)

4.3.2.2 Development of Equations

To facilitate the development of equation (4.3.2-1), we use, for an arbitrary vector \vec{A} , the linear operator:

$$(\vec{A} \cdot \nabla) \equiv A \frac{d}{d\alpha} \quad (4.3.2-4)$$

where $d/d\lambda$ is a directional derivative in the local direction of vector \vec{A} . With this notation, the acceleration for steady flow can be written as

$$\vec{a} = (\vec{V} \cdot \nabla) \vec{V}$$

Noting that the absolute velocity is

$$\vec{V} = \vec{W} + \vec{\Omega} \times \vec{r}$$

we obtain

$$\begin{aligned} \vec{a} &= [(\vec{W} + \vec{\Omega} \times \vec{r}) \cdot \nabla] (\vec{W} + \vec{\Omega} \times \vec{r}) \\ &= (\vec{W} \cdot \nabla) \vec{W} + (\vec{W} \cdot \nabla) (\vec{\Omega} \times \vec{r}) + [(\vec{\Omega} \times \vec{r}) \cdot \nabla] \vec{W} + [(\vec{\Omega} \times \vec{r}) \cdot \nabla] (\vec{\Omega} \times \vec{r}) \end{aligned} \quad (4.3.2-5)$$

If λ indicates the streamline direction (i.e. the local direction of \vec{W}) with

$$(d\lambda)^2 = (dr)^2 + (r d\theta)^2 + (dz)^2$$

and if the symbol d represents differentiation in the relative system, then the first two terms of (4.3.2-5) become, using equation (4.3.2-4),

$$(\vec{W} \cdot \nabla) \vec{W} = W \frac{d\vec{W}}{d\lambda} = \frac{d\lambda}{dt} \frac{d\vec{W}}{d\lambda} = \left(\frac{d\vec{W}}{dt} \right)_{\lambda} \quad (4.3.2-6)$$

$$(\vec{W} \cdot \nabla) (\vec{\Omega} \times \vec{r}) = \left(\frac{d\vec{\Omega}}{dt} \right)_{\lambda} \times \vec{r} + \vec{\Omega} \times \left(\frac{d\vec{r}}{dt} \right)_{\lambda} = \vec{\Omega} \times \vec{W} \quad (4.3.2-7)$$

The third term of equation (4.3.2-5) becomes

$$[(\vec{\Omega} \times \vec{r}) \cdot \nabla] \vec{W} = \Omega r \frac{d\vec{W}}{r\Omega dt} = \frac{d\vec{W}}{dt}$$

i.e., the time derivative of \vec{W} in the tangential direction, or

$$[(\vec{\Omega} \times \vec{r}) \cdot \nabla] \vec{W} = \vec{\Omega} \times \vec{W} \quad (4.3.2-8)$$

Similarly

$$\begin{aligned} [(\vec{\Omega} \times \vec{r}) \cdot \nabla] (\vec{\Omega} \times \vec{r}) &= \Omega r \left(\vec{\Omega} \times \frac{d\vec{r}}{r\Omega dt} \right) \\ &= \vec{\Omega} \times \left(\frac{d\vec{r}}{dt} \right) \end{aligned}$$



or, since in this case $\left(\frac{d\vec{r}}{dt}\right)$ is the tangential velocity

$$[(\vec{\Omega} \times \vec{r}) \cdot \nabla](\vec{\Omega} \times \vec{r}) = \vec{\Omega} \times (\vec{\Omega} \times \vec{r}) \quad (4.3.2-9)$$

Thus

$$\vec{a} = \left(\frac{d\vec{W}}{dt}\right)_{\lambda} + 2\vec{\Omega} \times \vec{W} + \vec{\Omega} \times (\vec{\Omega} \times \vec{r}) \quad (4.3.2-10)$$

Defining

$$\begin{aligned} \vec{W} &= W_r \dot{r} + W_{\theta} \dot{t} + W_z \dot{z} \\ &= \frac{dr}{dt} \dot{r} + r \frac{d\theta}{dt} \dot{t} + \frac{dz}{dt} \dot{z} \end{aligned}$$

and noting the following five results

$$\frac{d\dot{r}}{dt} = \frac{d\theta}{dt} \dot{t}$$

$$\frac{d\dot{t}}{dt} = -\frac{d\theta}{dt} \dot{r}$$

$$\vec{\Omega} \times \vec{r} = \begin{vmatrix} \dot{r} & \dot{z} & \dot{t} \\ 0 & \Omega & 0 \\ r & 0 & 0 \end{vmatrix} = -r\Omega \dot{t}$$

$$\vec{\Omega} \times (\vec{\Omega} \times \vec{r}) = \begin{vmatrix} \dot{r} & \dot{z} & \dot{t} \\ 0 & \Omega & 0 \\ 0 & 0 & -r\Omega \end{vmatrix} = -r\Omega^2 \dot{r}$$

$$\Omega \times \vec{W} = \begin{vmatrix} \dot{r} & \dot{z} & \dot{t} \\ 0 & \Omega & 0 \\ W_r & W_z & W_{\theta} \end{vmatrix} = \Omega W_{\theta} \dot{r} - \Omega W_r \dot{t}$$

the radial, tangential, and axial components of acceleration are

$$\vec{a} \cdot \dot{r} = \frac{dW_r}{d\lambda} W - \frac{1}{r} (r\Omega - W_{\theta})^2 \quad (4.3.2-11)$$

$$\vec{a} \cdot \dot{t} = \frac{dW_{\theta}}{d\lambda} W + \frac{W_r W_{\theta}}{r} - 2\Omega W_r \quad (4.3.2-12)$$

$$\vec{a} \cdot \vec{\epsilon} = \frac{dW}{d\lambda} \vec{\epsilon} \quad (4.3.2-13)$$

It was mentioned earlier (see equations (4.1.1-2) through (4.1.2-10)) that the friction forces are given by a vector term of the form

$$\vec{F} = \frac{dL}{d\lambda} \frac{\vec{W}}{W} = \left(\frac{dL}{d\lambda} \frac{W_r}{W} \right) \vec{r} + \left(\frac{dL}{d\lambda} \frac{W_\theta}{W} \right) \vec{t} + \left(\frac{dL}{d\lambda} \frac{W_z}{W} \right) \vec{z} \quad (4.3.2-14)$$

We now have the mechanism for writing the component equations of the motion equation (4.3.2-1) by a proper combination of equations (4.3.2-11), (4.3.2-12), (4.3.2-13) and (4.3.2-14) with

$$\nabla p = \frac{\partial p}{\partial r} \vec{r} + \frac{1}{r} \frac{\partial p}{\partial \theta} \vec{t} + \frac{\partial p}{\partial z} \vec{z}$$

One special component of the motion equation is its component in the streamline (or \vec{W}) direction, because of the way in which the friction forces and the losses are defined. To obtain it, we merely form the dot product of equation (4.3.2-1) with \vec{W} . From equation (4.3.2-10),

$$\begin{aligned} \vec{a} \cdot \vec{W} &= \frac{d\vec{W}}{dt} \cdot \vec{W} + 2(\vec{\Omega} \times \vec{W}) \cdot \vec{W} + [\vec{\Omega} \times (\vec{\Omega} \times \vec{r})] \cdot \vec{W} \\ &= \frac{1}{2} \frac{d}{dt} (W^2 - \Omega^2 r^2) \end{aligned}$$

or, since $W = \frac{d\lambda}{dt}$

$$\vec{a} \cdot \vec{W} = (\vec{a} \cdot \vec{W}) \frac{dt}{d\lambda} = \frac{1}{2} \frac{d}{d\lambda} (W^2 - \Omega^2 r^2) \quad (4.3.2-15)$$

From equation (4.3.2-14),

$$\vec{F} \cdot \vec{W} = \frac{dL}{d\lambda} \vec{W} \cdot \vec{W} = \frac{dL}{d\lambda} \quad (4.3.2-16)$$

We also note that

$$\nabla p \cdot \vec{W} = \frac{dp}{d\lambda} \quad (4.3.2-17)$$

Thus

$$\left(\frac{g_0}{\rho} \nabla p + \vec{a} + \vec{F} \right) \cdot \vec{W} = 0$$

or

$$\frac{g_0}{\rho} \frac{dp}{d\lambda} - \frac{1}{2} \frac{d}{d\lambda} (W^2 - \Omega^2 r^2) + \frac{dL}{d\lambda} = 0 \quad (4.3.2-18)$$



which is the streamline component of the motion equation. This equation may be combined with any two of the other three components of the motion equation, so long as these two are independent of equation (4.3.2-18).

For the continuity equation (4.3.2-2), we write

$$\nabla \cdot (\rho \vec{W}) = \nabla \rho \cdot \vec{W} + \rho \nabla \cdot \vec{W} = 0$$

Since $\nabla \rho \cdot \vec{W} = \frac{d\rho}{d\lambda} W$, this may be written as

$$\frac{d\rho}{\rho} = \frac{\nabla \cdot \vec{W}}{W} d\lambda \quad (4.3.2-19)$$

where the velocity divergence is given by

$$\nabla \cdot \vec{W} = \frac{W_r}{r} + \frac{\partial W_r}{\partial r} + \frac{1}{r} \frac{\partial W_\theta}{\partial \theta} + \frac{\partial W_z}{\partial z} \quad (4.3.2-20)$$

As mentioned earlier, the method is to solve the system of equations

$$\left\{ \begin{aligned} dp &= \frac{-\rho}{g_0} \left[\frac{1}{2} d(W^2 - \Omega^2 r^2) + dL \right] \text{ along streamlines} \end{aligned} \right. \quad (4.3.2-21)$$

$$\left\{ \begin{aligned} \frac{g_0}{\rho} \frac{\partial p}{\partial r} &= - \frac{dW_r}{d\lambda} W + \frac{1}{r} (r\Omega - W_\theta)^2 - \frac{dL}{d\lambda} \frac{W_r}{W} \end{aligned} \right. \quad (4.3.2-22)$$

$$\left\{ \begin{aligned} \frac{g_0}{\rho r} \frac{\partial p}{\partial \theta} &= - \frac{dW_\theta}{d\lambda} W - \frac{W_r W_\theta}{r} + 2\Omega W_r - \frac{dL}{d\lambda} \frac{W_\theta}{W} \end{aligned} \right. \quad (4.3.2-23)$$

subject to

$$\frac{d\rho}{\rho} = - \frac{\nabla \cdot \vec{W}}{W} d\lambda \quad (4.3.2-19)$$

and

$$\rho = \begin{cases} \rho_f & \text{if } p \geq p_{sat} \\ \rho_f / [1 + \mathcal{J}(p_{sat} - p)] & \text{if } p < p_{sat} \end{cases} \quad (4.3.2-3)$$

where dL is as given in equations (4.1.3-1) through (4.1.3-9), and

$$W^2 = W_r^2 + W_\theta^2 + W_z^2$$

4.3.2.3 Numerical Methods

A number of points are selected on the inlet plane perpendicular to the axis of the rotating flow channel. These may be thought of as belonging to streamlines about to enter the channel. As a starting approximation, the radial and circumferential positions of the points where these streamlines pierce the various axial planes are in the same hub-to-tip and blade-to-blade ratio, respectively, as are those for the corresponding points immediately upstream. At these points, throughout the flow channel, a one-dimensional axial velocity is calculated to satisfy continuity in the large, i.e., W_z inversely proportional to cross-sectional area, normal to the z -axis. The other two velocity components are then determined by the local streamline direction, by a finite difference form of

$$W_r = \frac{dr}{dz} W_z \quad (4.3.2-24)$$

and

$$W_\theta = r \frac{d\theta}{dz} W_z \quad (4.3.2-25)$$

When this initial estimate of streamline position and velocity components is made, the pressures and densities along these various streamlines are determined by a simultaneous solution of equations (4.3.2-3) and (4.3.2-21). If K denotes the number of the z -station and i the streamline number, it is first determined if the fluid is a single phase liquid at point (i, K) by seeing if

$$p_{i,K} = p_{i,K-1} - \left(\frac{\rho_{i,K} + \rho_f}{2g_0} \right) \left[\frac{W_{i,K}^2 - W_{i,K-1}^2 - \Omega^2(r_{i,K}^2 - r_{i,K-1}^2)}{2} + dL_{i,K} \right] \geq p_{sat} \quad (4.3.2-26a)$$

If this is so, then $p_{i,K}$ is accepted as the static pressure at that point and $\rho_{i,K} = \rho_f$. Otherwise the quadratic equation resulting from

$$p_{i,K} = p_{i,K-1} - \frac{1}{2g_0} \left[\rho_{i,K} + \frac{\rho_f}{1 + \mathcal{T}(p_{sat} - p_{i,K})} \right] \left[\frac{W_{i,K}^2 - W_{i,K-1}^2 - \Omega^2(r_{i,K}^2 - r_{i,K-1}^2)}{2} + dL_{i,K} \right] \quad (4.2.3-26b)$$

is solved for $p_{i,K}^{(*)}$, which pressure is then substituted into the state equation to calculate the corresponding two-phase density

$$\rho_{i,K} = \frac{\rho_f}{1 + \mathcal{T}(p_{sat} - p_{i,K})}$$

(*) Note how the use of equation (4.3.2-21) makes the calculations follow streamlines. These streamlines are characteristic directions of the solution.



Thus far the state equation and the streamline component of the motion equation have been satisfied simultaneously; i.e., the velocities, pressures, and densities along each individual streamline are consistent with each other. When considering the interaction of neighboring streamlines, however, continuity as well as radial and tangential equilibrium (see equations (4.3.2-22) and (4.3.2-23) have yet to be checked. To do this, three residuals which are the kernel of the iteration scheme are formed.

One residual is the difference between the density indicated by the state equation (4.3.2-3) and the density indicated by the continuity equation (4.3.2-19). Symbolically,

$$R_1 = (\rho)_{state} - (\rho)_{cont} \quad (4.3.2-27)$$

$(\rho)_{cont}$ is calculated by solving equation (4.3.2-19) in finite difference form:

$$\frac{(\rho_{i,k})_{cont} - (\rho_{i,k-1})_{state}}{(\rho_{i,k})_{cont}} = - \frac{(\nabla \cdot \vec{W})_{i,k} d\lambda_{i,k}}{\sqrt{\frac{W_{i,k}^2 + W_{i,k-1}^2}{2}}}$$

where numerical methods require the use of the root-mean-square \bar{W} .

Thus

$$(\rho_{i,k})_{cont} = (\rho_{i,k-1})_{state} \left[1 + \frac{(\nabla \cdot \vec{W})_{i,k} d\lambda_{i,k}}{\sqrt{\frac{W_{i,k}^2 + W_{i,k-1}^2}{2}}} \right]^{-1} \quad (4.3.2-28)$$

where

$$(d\lambda_{i,k})^2 = (r_{i,k} - r_{i,k-1})^2 + \left(\frac{r_{i,k} + r_{i,k-1}}{2} \right)^2 (\theta_{i,k} - \theta_{i,k-1})^2 + (z_k - z_{k-1})^2$$

and where the partial derivatives in $(\nabla \cdot \vec{W})_{i,k}$ (cf. equation (4.3.2-20)) are calculated by the special algorithm discussed in Section 4.3.3.3. Thus R_1 is an indication of how well the streamline density change, as indicated by the velocity divergence, agrees with the change indicated by the fluid state properties(*).

The other residuals can also be represented symbolically as

$$R_2 = \frac{g_0}{(\rho)_{state}} \left(\frac{\partial p}{\partial r} \right)_{state} - \left(\frac{g_0}{\rho} \frac{\partial p}{\partial r} \right)_{motion}$$

(*) It should be noted that the state equation (4.3.2-3) is represented by a continuous, though not smooth, curve. The effects of this discontinuity in the first derivative upon R_1 , and upon convergence in general, have not yet been investigated.

$$\text{and } R_3 = \frac{g_0}{r(\rho)_{state}} \left(\frac{\partial p}{\partial \theta} \right)_{state} - \left(\frac{g_0}{\rho r} \frac{\partial p}{\partial \theta} \right)_{motion}$$

i.e., as measures of the agreement between the fluid state properties and the velocity field. Specifically,

$$R_2 = \frac{g_0}{\rho} \frac{\partial p}{\partial r} + \frac{dW_r}{d\lambda} W - \frac{1}{r} (r\Omega - W_\theta)^2 + \frac{dL}{d\lambda} \frac{W_r}{W} \quad (4.3.2-29)^*$$

$$R_3 = \frac{g_0}{r\rho} \frac{\partial p}{\partial \theta} + \frac{dW_\theta}{d\lambda} W + \frac{W_r W_\theta}{r} - 2\Omega W_r + \frac{dL}{d\lambda} \frac{W_\theta}{W} \quad (4.3.2-30)^*$$

where the various streamline total derivatives (e.g. $\frac{dW_r}{d\lambda}$) are obtained as backward differences and where the partial radial and tangential derivatives, $\left(\frac{\partial p}{\partial r} \right)$ and $\left(\frac{\partial p}{\partial \theta} \right)$, are calculated by a special algorithm (discussed in Section 4.3.3.3) from the actual pressure distribution given by the simultaneous solution of the streamline motion and state equations (see equations (4.3.2-26a) and (4.3.2-26b)).

4.3.2.4 Iteration Methods

A velocity-pressure-density distribution for which $|R_1|$, $|R_2|$, and $|R_3|$ are less than some predetermined quantity is considered a solution. Since the starting assumptions consisted of estimates of streamline locations and velocities, it is these quantities which have to be adjusted in order to bring about a solution. Hence r , θ , and W_z were chosen as the basic variables of the problem (also see Section 4.3.3.2).

Variations of two iteration methods, which might be classified as methods of steepest descent¹⁴, were tried. Both of these involve the partial derivatives $\partial R_j / \partial r$, $\partial R_j / \partial \theta$, $\partial R_j / \partial W_z$ ($j = 1, 2, 3$). First order approximations of these partial derivatives are calculated by successive perturbations of the three independent variables, similar to the way in which the derivative dR/dr was estimated for the quasi three-dimensional solution in Section 4.2.3.

Method A consists of simultaneously reducing the numerical values of the three separate residuals. If $R_j = R_j(r, \theta, W_z) \neq 0$ adjustments δr , $\delta \theta$, and δW_z must be found such that

$$R_j(r + \delta r, \theta + \delta \theta, W_z + \delta W_z) = 0$$

(*) Compare with equations (4.3.2-22) and (4.3.2-23).



But a first order Taylor series expansion gives

$$R_j(r+\delta r, \theta+\delta \theta, W_z+\delta W_z) = R_j(r, \theta, W_z) + \frac{\partial R_j}{\partial r} \delta r + \frac{\partial R_j}{\partial \theta} \delta \theta + \frac{\partial R_j}{\partial W_z} \delta W_z$$

Writing this expression for $j = 1, 2, 3$, and equating it to zero yields the linear system

$$\frac{\partial R_1}{\partial r} \delta r + \frac{\partial R_1}{\partial \theta} \delta \theta + \frac{\partial R_1}{\partial W_z} \delta W_z = -R_1,$$

$$\frac{\partial R_2}{\partial r} \delta r + \frac{\partial R_2}{\partial \theta} \delta \theta + \frac{\partial R_2}{\partial W_z} \delta W_z = -R_2$$

$$\frac{\partial R_3}{\partial r} \delta r + \frac{\partial R_3}{\partial \theta} \delta \theta + \frac{\partial R_3}{\partial W_z} \delta W_z = -R_3$$

which must be solved for δr , $\delta \theta$, and δW_z . The condition for this system to be soluble is

$$\begin{vmatrix} \frac{\partial R_1}{\partial r} & \frac{\partial R_1}{\partial \theta} & \frac{\partial R_1}{\partial W_z} \\ \frac{\partial R_2}{\partial r} & \frac{\partial R_2}{\partial \theta} & \frac{\partial R_2}{\partial W_z} \\ \frac{\partial R_3}{\partial r} & \frac{\partial R_3}{\partial \theta} & \frac{\partial R_3}{\partial W_z} \end{vmatrix} \neq 0$$

Once these adjustments have been calculated, the position of the streamline is shifted from (r, θ, z) to $(r+\delta r, \theta+\delta \theta, z)$, and the axial velocity is changed from W_z to $(W_z + \delta W_z)$.

Method B minimizes a single, non-negative function composed of the three residuals. Specifically

$$E = R_1^2 + R_2^2 + R_3^2$$

is minimized. This is equivalent to Method A since $E = 0$ if, and only if, $R_1 = 0$, $R_2 = 0$, and $R_3 = 0$ simultaneously. The minimization method is essentially that of Newton and Raphson^(14, p 349) and the required adjustments are calculated from

$$\delta r = E' \left(\frac{\partial E}{\partial r} \right)$$

$$\delta \theta = \frac{E'}{r} \left(\frac{\partial E}{\partial \theta} \right)$$

$$\delta W_z = E' \left(\frac{\partial E}{\partial W_z} \right)$$

where,

$$E' = - \frac{E}{\frac{1}{2} \left[\left(\frac{\partial E}{\partial r} \right)^2 + \frac{1}{r^2} \left(\frac{\partial E}{\partial \theta} \right)^2 + \left(\frac{\partial E}{\partial W_z} \right)^2 \right]}$$

and, again, streamlines are shifted and velocities changed exactly as in Method A(*).

The computer makes one pass (or cycle) through the flow channel, locating the streamlines and assigning axial velocities. In a second pass the remaining velocity components, pressures, and densities are calculated. Following this, there are three cycles through the flow channel for each iteration. In the first, the three residuals are calculated at each point and the required adjustments δr , $\delta \theta$, and δW_z are obtained. (These are stored and not executed in this cycle.) The second cycle is for actually making the adjustments which were indicated in the first. In the last cycle, W_r , W_θ , ρ , and ρ are recalculated at each point, thus changing the flow field. The next cycle, which is the first of a new iteration, is for calculating the new residuals, etc. A new iteration (3 cycles) is started as long as there is a residual which is "too large", anywhere in the channel.

4.3.2.5 General Boundary Conditions

Figure 4.3.2-2 shows a developed view of an inducer flow channel. The boundaries are as follows:

The Fixed Boundaries are the hub and shroud (respectively below and above the plane of the drawing) and the pressure suction sides of the channel. These are obtained from the blades by allowing for their thickness t and the boundary layer displacement thickness δ^* . Also included are Z_0 and Z_{n+1} , which are planes of constant z , or axial stations, across fluid flows.

The Quasi Boundaries are the stream-surfaces denoted by a, b, c, and d, and must be located so as to include only the fluid which flows between the blades from Z_0 to Z_{n+1} . Several upstream and downstream stations might be required, but only one of each was used to avoid further iteration complexity.

The placement of the blades is accomplished by the method outlined in Section 4.2.2. On the hub and shroud, as well as on the boundaries comprising the pressure and suction sides of the channel, the condition

$$\vec{W} \cdot \vec{n} = 0$$

must be satisfied, where \vec{n} is a unit vector normal to any of the four boundaries mentioned.

(*) For a comparative discussion of Methods A and B, see Section 4.3.3.4.

DEVELOPED VIEW OF INDUCER FLOW CHANNEL SHOWING BOUNDARIES

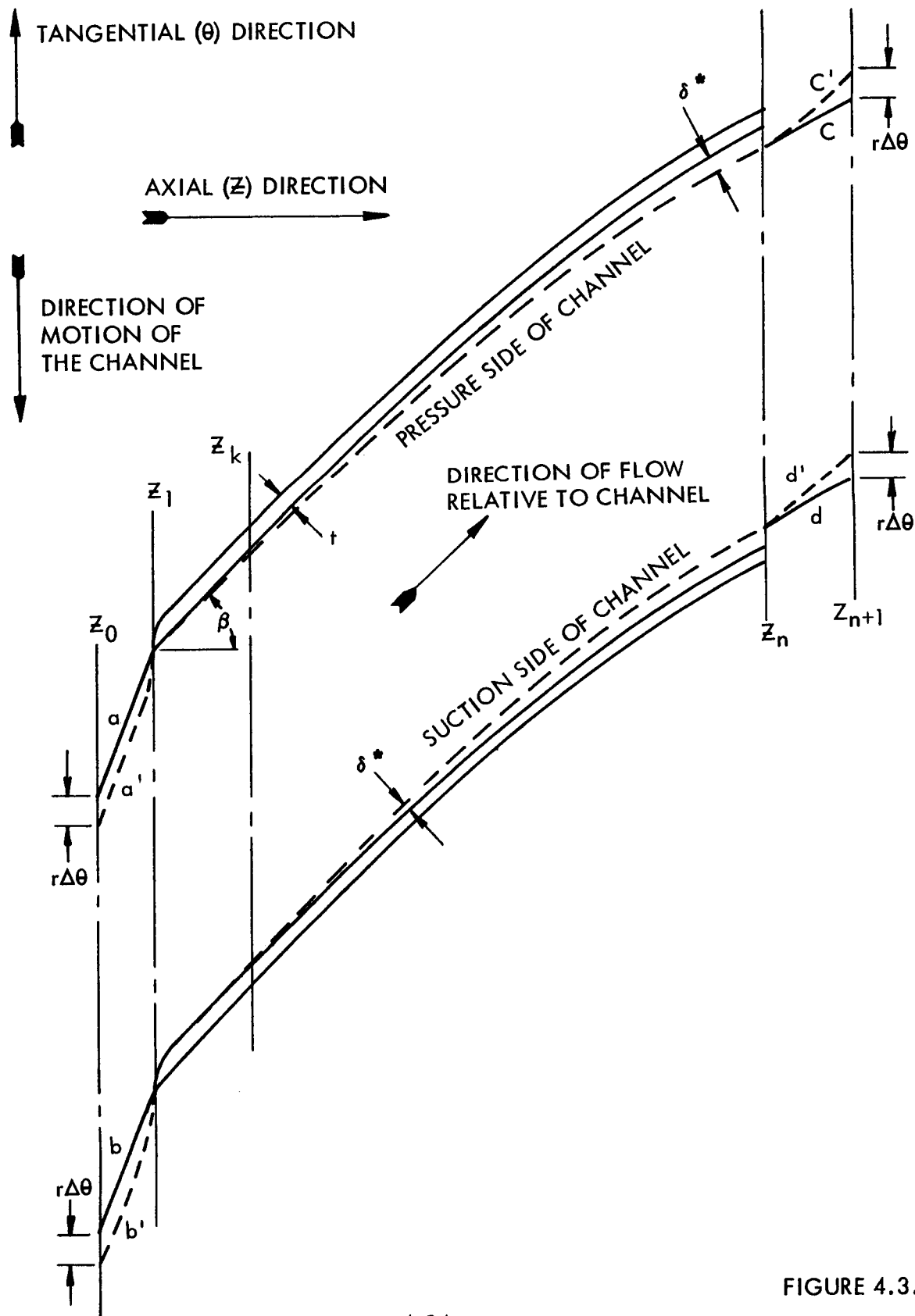


FIGURE 4.3.2-2

The fixed boundary Z_0 , a short but sufficient distance upstream of the blade leading edges, must meet the requirement at each radius that all fluid flow across it at a tangentially uniform velocity and in the direction prescribed by the input absolute velocity and the blade speed. The points where the quasi-boundaries a and b (stream surfaces) intersect the Z_0 plane are determined in the iteration from the condition that pressure be continuous across a and b. After each iteration of the flow field, the pressures at Z_1 on a and b are compared. If, for example, a discontinuity exists such that $p_{b,1} > p_{a,1}$, their upstream (Z_0) locations are moved from the initially assumed ones (a and b) to those of a' and b', or vice versa. The amount of correction $r \Delta \theta$ is the same for both a and b because of symmetrical considerations. The condition on a and b is that no velocity can exist normal to them.

The fixed boundary Z_{n+1} and the quasi-boundaries c and d require conditions and iterations similar to those of the inlet. However, within the channel, between boundaries c and d, the downstream velocity and its direction (assumed for the first iteration) is found at the end of each iteration by calculating the mass-averaged velocity versus radius at the Z_n station. The flow from Z_n to Z_{n+1} is assumed to be restricted to annuli. The streamline locations at Z_{n+1} are obtained by continuity considerations applied from Z_n to Z_{n+1} to the sizes of a fixed number of segments within each annulus.

The resulting streamline positions and velocities constitute the boundary conditions for the next iteration. Note that a non-pressure-discontinuity-supporting wake of thickness $t + 2\delta_n^*$ is thus assumed to exist off the trailing edge of each blade, in the direction of the quasi-boundaries c and d (see Figure 4.3.2-2).

4.3.2.6 Simplified Boundary Conditions

For practical reasons involving computer time and because involvement in these general boundary conditions tended to obscure the numerical examination of the method between inlet and outlet, the following simplified boundary conditions were imposed upon the problem:

No streamline is permitted to cross the hub, shroud, suction, or pressure surfaces. If numerical calculations of δr or $\delta \theta$ at a point indicate that the streamline would pierce one of these boundary surfaces, the point is left unaltered (i.e., the indicated adjustments are ignored) and the calculation proceeds to the next point. This roughly corresponds to the condition

$$\vec{W} \cdot \vec{n} = 0$$

where \vec{n} is a unit vector normal to the boundary surface.

At the upstream boundary of the flow field, uniform axial flow is assumed and no subsequent adjustments are made on this boundary.



At the downstream boundary, the locations of the stagnation streamlines are fixed and the streamlines from the interior of the channel are extended downstream at constant β .

4.3.3 Comments on the Three-Dimensional Solution and Recommendations

4.3.3.1 General Observations

The grid for the finite difference equations of the three-dimensional solution floats (i.e., the locations of the points at which calculations are made) varies from one iteration to the next. This is a direct consequence of the fact that the grid points are the locations at which the streamlines, which have to be shifted in order to satisfy radial and tangential equilibrium, pierce the fixed Z-planes. Functionally, however, one might consider the subscripts i and k as the true independent variables.

4.3.3.2 W_θ As Independent Variable

Since W_θ is the dominant velocity component, r, θ , and W_θ were tried as the basic variables instead of r, θ , and W_z . Thus, in the residual reduction (Section 4.3.2.4) $\partial R_j / \partial W_\theta$ was calculated instead of $\partial R_j / \partial W_z$. This was desirable since a small inaccuracy in the value of W_z is magnified four or five times in W_θ (and hence also in W). The iteration scheme is not as sensitive to a small inaccuracy in W_θ , however. The remaining velocity components are then calculated from finite difference analogues of

$$W_z = \frac{1}{r} \frac{dz}{d\theta} W_\theta$$

and

$$W_r = \frac{1}{r} \frac{dr}{d\theta} W_\theta$$

4.3.3.3 Special Algorithm for Calculating Partial Derivatives

Partial derivatives are necessary in the continuity equation (4.3.2-19) and (4.3.2-20), and in the reduction of residuals R_2 and R_3 (Section 4.3.2.4). For calculating the radial and tangential partial derivatives of static pressure, for example, a special algorithm is constructed as follows (see Figure 4.3.3-1)^(*):

(*) Note that the usual direct method is not applicable since the points do not, in general, fall into a uniform (r, θ) grid.

CONFIGURATION FOR PARTIAL DERIVATIVE ALGORITHM

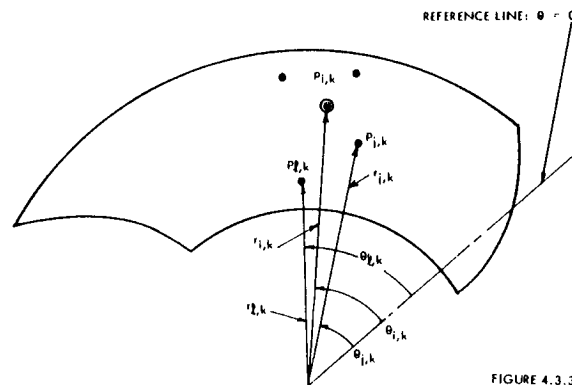


FIGURE 4.3.3-1

The computer selects the two closest points to (i, k) in the plane $Z = Z_k$. These might be labeled (j, k) and (l, k) . The directional derivative of p from (i, k) to (j, k) can be approximated by

$$p_{j,k} - p_{i,k} = \left(\frac{\partial p}{\partial r} \right)_{i,k} (r_{j,k} - r_{i,k}) + \left(\frac{\partial p}{\partial \theta} \right)_{i,k} (\theta_{j,k} - \theta_{i,k}) \quad (4.3.3-1)$$

Similarly

$$p_{l,k} - p_{i,k} = \left(\frac{\partial p}{\partial r} \right)_{i,k} (r_{l,k} - r_{i,k}) + \left(\frac{\partial p}{\partial \theta} \right)_{i,k} (\theta_{l,k} - \theta_{i,k}) \quad (4.3.3-2)$$

If the polar coordinates of points (i, k) , (j, k) , and (l, k) are known, together with the values of p at those points, these equations may be solved simultaneously for $(\partial p / \partial r)_{i,k}$ and $(\partial p / \partial \theta)_{i,k}$. If, however, the three points lie on a curve (spiral) for which $dr/d\theta$ is constant, equations (4.3.3-1) and (4.3.3-2) will no longer be independent and a solution with these points is impossible. Even if these points lie close to such a spiral, gross inaccuracies occur in the calculation of the partial derivatives. Thus the points (j, k) and (l, k) must be replaced by other points, whose distance from (i, k) might introduce new inaccuracies. Hence, restrictions are placed on the relative positions of the "close" points selected by the computer. Inaccuracies, however, are still present in the calculations and introduce unwarranted instabilities into the iteration scheme.

Much greater accuracy can be achieved by fitting a second degree surface through point (i, k) and four surrounding points. For this, the equation

$$p_{i,k} = a_1 r_{i,k}^2 + a_2 r_{i,k} \theta_{i,k} + a_3 \theta_{i,k}^2 + a_4 r_{i,k} + a_5 \theta_{i,k} + a_6$$



would be written for the five points and then, solving these five equations simultaneously for a_1, a_2, a_3, a_4 , and a_5 , the following calculations made:

$$\left(\frac{\partial p}{\partial r}\right)_{i,K} = 2a_1 r_{i,K} + a_2 \theta_{i,K} + a_4 \quad (4.3.3-3)$$

and

$$\left(\frac{\partial p}{\partial \theta}\right)_{i,K} = a_2 r_{i,K} + 2a_3 \theta_{i,K} + a_5 \quad (4.3.3-4)$$

If $(\partial W_Z / \partial r)_{i,K}$ and $(\partial W_Z / \partial \theta)_{i,K}$ are obtained in this way, $(\partial W_Z / \partial Z)_{i,K}$ may be calculated from

$$\begin{aligned} W_{Z,i,K+1} - W_{Z,i,K} = & \left(\frac{\partial W_Z}{\partial r}\right)_{i,K} (r_{i,K+1} - r_{i,K}) \\ & + \left(\frac{\partial W_Z}{\partial \theta}\right)_{i,K} (\theta_{i,K+1} - \theta_{i,K}) + \left(\frac{\partial W_Z}{\partial Z}\right)_{i,K} (Z_{K+1} - Z_K) \end{aligned} \quad (4.3.3-5)$$

This latter algorithm has not yet been incorporated into the computer program.

4.3.3.4 Comparison of Iteration Methods A and B

It was found empirically that Method B (minimizing $E = R_1^2 + R_2^2 + R_3^2$ with respect to r, θ , and W_θ) was somewhat less stable than Method A (minimizing $|R_1|, |R_2|, |R_3|$ individually but simultaneously). Fewer points tended to be pushed through the boundary surfaces (cf. Section 4.3.2.5) with Method A than with Method B. Analytical reasons for this difference have not been established.

4.3.3.5 Recommendations

Since fluid flow in the particular inducer analyzed is dominantly tangential, it is recommended that the Z -component of the motion equation,

$$\frac{\partial p}{\partial Z} = - \frac{dW_Z}{d\lambda} W - \frac{dL}{d\lambda} \frac{W_Z}{W}$$

be used in residual calculations instead of the θ -component, as used in the calculation of R_3 (equation 4.3.2-30). The streamline component (equation 4.3.2-18) is less dependent on the Z -component than it is on the θ -component and faster convergence might result.

An analysis should be made of ways of resolving the vector motion equation (equation 4.3.2-1) into components other than axial, radial, and tangential, so that such a solution might also be applicable to radial and mixed-flow machines. This may necessitate replacing the fixed Z -planes with surfaces of general curvature, possibly normal to the meridional streamlines.

4.4 STUDIES OF SCALE AND FLUID EFFECTS

4.4.1 Introduction

To determine the requirements for applying test results of one fluid in a given geometry to a different fluid and scale size, two facts must be established. First, one must find the parameters that establish similarity between the two situations. This is accomplished by a dimensional analysis of the process involved. Secondly, recognizing that direct scaling of results is possible only if all these parameters are held constant for both cases, one must find the effects of departure from dynamic similarity; i.e., one must know how to modify the test results to account for differences in one or more of the parameters for the two cases. This knowledge is obtained either by further tests or, with an adequate theoretical flow model, by calculation of the performance at the different values of these parameters. Work has been accomplished in both these areas. This has led to some interesting conclusions about NPSH requirements, which are also discussed.

4.4.2 Dimensional Analysis

A complete dimensional analysis includes all the physical variables known to affect the flow process. The early work in this area yielded a large number of parameters, and an effort was made to eliminate the insignificant ones so that the problem of finding the primary scale and fluid effects could be approached. This led, through the studies of Section 4.1, to a restriction of this analysis to the process described by the flow model.

Since this dimensional analysis of the flow model omits some of the real fluid effects, such as relative motion between the phases and heat transfer losses, work has been done to determine, with certain assumptions, an important additional parameter which might include most of these phenomena. This additional quantity is the ratio of the equilibrium bubble diameter to the inducer inlet diameter.

The dimensional analysis was started by an examination of the equations in the flow model to determine what variables should be included. The physical equation was then obtained:

$$P_2 - P_1 = f \left[U_{1,t}, V_1, r_{1,t}, \nu, (P_1 - p_{sat}), \frac{\rho_f}{\rho_o}, \frac{\rho_g}{\rho_o}, s_{f,sat}, \left(\frac{ds_f}{dp} \right)_{sat} \right] \quad (4.4.2-1)$$

This leads to the dimensionless parameters that affect performance for a given geometry:

$$\frac{\rho_o (P_2 - P_1)}{\rho_f U_{1,t}^2} = f \left[\frac{V_1}{U_{1,t}}, \frac{U_{1,t} r_{1,t}}{\nu}, \frac{2 \rho_o (P_1 - p_{sat})}{\rho_f U_{1,t}^2}, \left(\frac{ds_f}{dp} \frac{\rho_f U_{1,t}^2}{s_{fg} \rho_o} \right)_{sat}, \left(\frac{\rho_f}{\rho_g} \right)_{sat} \right] \quad (4.4.2-2)$$



Introducing new symbols for each of these terms respectively, we obtain:

$$\psi = f \left[\phi, Re, \tau, X, \left(\frac{\rho_f}{\rho_g} - 1 \right)_{sat} \right] \quad (4.4.2-3)$$

The head coefficient ψ , flow coefficient ϕ , Reynolds number Re , and the cavitation parameter τ are the conventional ones that appear in a pump analysis. The last two terms, a quality parameter X and the saturated liquid-vapor density ratio, account for the thermodynamic effects of cavitation when it occurs. They appear together as a product in the non-dimensionalized equation of state, and so we henceforth denote $X \left(\frac{\rho_f}{\rho_g} - 1 \right)$ by Θ . Thus equation (4.4.2-3) becomes

$$\psi = f(\phi, Re, \tau, \Theta) \quad (4.4.2-4)$$

These constitute the inducer similarity parameters contained in the flow model.

Now we obtain the non-dimensional form of the equation of the flow model, utilizing dimensionless groups of the form obtained above.

Denoting
$$\hat{p} = \frac{(p - p_i) g_o}{\rho_f u_{i,t}^2} \quad (4.4.2-5)$$

$$\hat{Y} = \frac{Y}{u_{i,t}} \quad (4.4.2-6)$$

where Y is any velocity (W or V);

$$\hat{\Lambda} = \frac{\Lambda}{r_{i,t}} \quad (4.4.2-7)$$

where Λ is any length (λ, r, D_h)

$$\hat{Q} = \frac{Q}{u_{i,t} r_{i,t}^2} \quad (4.4.2-8)$$

$$\hat{\rho} = \rho / \rho_f \quad (4.4.2-9)$$

we obtain the non-dimensionalized equations as follows:

a. Continuity

$$\hat{\vec{W}} \cdot \nabla \hat{\rho} + \hat{\rho} \nabla \cdot \hat{\vec{W}} = 0 \quad (4.4.2-10)$$

b. Motion

The component equation in the streamline direction is

$$\frac{d\hat{p}}{d\hat{s}} = d\left(\frac{\hat{r}^2}{2}\right) - d\left(\frac{\hat{w}^2}{2}\right) - d\hat{L} \quad (4.4.2-11)$$

where
$$d\hat{L} = \frac{f}{\hat{D}_h} \frac{\hat{w}^2}{2} d\hat{\lambda} - k \frac{d\hat{w}^2}{2} \quad (4.4.2-12)$$

$$f = 0.00714 + \frac{0.6104}{(\hat{w} \hat{D}_h Re)^{0.35}} \quad (4.4.2-13)$$

$$k = 1 - \frac{a}{a - \frac{1}{2} \frac{d\hat{w}}{d\hat{\lambda}} \sqrt{\frac{\hat{Q}_i}{\pi n_b \hat{w}^3}}} \quad (4.4.2-14)$$

$$(k = 0 \text{ for } \frac{d\hat{w}}{d\hat{\lambda}} \geq 0)$$

The components in the radial and the tangential directions are obtained from

$$\frac{\hat{\nabla} \hat{p}}{\hat{\rho}} = \hat{r} - (\hat{w} \cdot \hat{\nabla}) \hat{w} - 2 \hat{u}_3 \times \hat{w} - \frac{d\hat{L}}{d\hat{\lambda}} \frac{\hat{w}}{|\hat{w}|} \quad (4.4.2-15)$$

where \hat{u}_3 is a unit vector in the direction of the vector $\vec{\Omega}$ (axial direction).

c. Energy (See equation (4.4.2-11).)

d. State
$$\hat{\rho} = 1 \quad (\hat{p} \geq \hat{p}_{sat}) \quad (4.4.2-16)$$

$$\hat{\rho} = \frac{1}{1 - \Theta \left(\frac{\tau}{2} + \hat{p} \right)} \quad \begin{aligned} &(\hat{p} \leq \hat{p}_{sat}) \\ &(\hat{p}_{sat} \equiv -\frac{\tau}{2}) \end{aligned} \quad (4.4.2-17)$$

The last equation shows how the quantity $\Theta = \mathbf{X} \left(\frac{\hat{p}_f}{\hat{p}_g} - 1 \right)$ enters the calculation. The limitations of the state equation simplifications discussed in Section 4.1.2 are understood, and if necessary, equation (4.4.2-17) can take a more complex form which could include, among other things, several Θ 's each multiplied by a different fraction of the quantity $\left(\frac{\tau}{2} + \hat{p} \right)$.



It will be recognized in view of equation (4.4.2-4) that for a given geometry it is possible to obtain the complete performance description for all scales, fluids, and flow coefficients by simply running the computer program calculations for all desired values of the independent dimensionless quantities on the right hand side of the equation.

The quasi three-dimensional solution of the flow fluid (Section 4.1) in its present form can be run either with dimensional or dimensionless inputs. (See Appendix D.) The dimensionless solution, therefore, registers a change only when one or more of the four independent parameters of equation (4.4.2-4) are changed. In this way, the effects of departure from similarity are obtained. Section 4.7 shows calculations and test results for variation of these quantities.

4.4.3 Bubble Studies

The real, additional effects of the two phase motion not covered in the existing flow model need to be considered for a complete discussion of the subject of similarity. Assuming that a known characteristic equilibrium bubble radius ratio, $r_b/r_{i,t}$, implicitly contains departure from thermal equilibrium and most of the remaining parameters that influence the flow, we may rewrite the equation (4.4.2-4) to represent very closely the actual flow process in a cavitating inducer:

$$\psi = f\left(\phi, Re, \tau, \Theta, \frac{r_b}{r_{i,t}}\right) \quad (4.4.3-1)$$

Note that the last three parameters have no influence when vaporization (cavitation) is absent. The calculation of the last quantity, $r_b/r_{i,t}$, is complicated. However, with certain assumptions, we can estimate at least how it varies from one fluid to another. For this we assume that no temperature difference exists between the vapor and liquid, that the liquid is in the presence of its own vapor, and that the bubble is in a state of mechanical equilibrium. The relation between the pressure ratio across the bubble surface and the equilibrium bubble radius r_b is given by the Kelvin relation¹⁵:

$$r_b = \frac{\chi}{\ln \frac{p_i}{p_o}} \quad (4.4.3-2)$$

where

$$\chi = \frac{2\sigma}{\rho_f RT} \quad (4.4.3-3)$$

This relation is plotted in Figure 4.4.3-1. With some small error, ρ_f is assumed to be that of the saturated liquid corresponding to the mixture condition. This, together with the need to evaluate p_i/p_o , introduces the problem of metastable states in the two phases within the quality regions of thermodynamic property diagrams. With extensive work in this area, p_i/p_o could be determined; however, for the present we shall have to estimate p_i/p_o , possibly as a constant number close to 1 for all fluids. On such a basis, Figure 4.4.3-1 immediately yields r_b , and the final parameter of equation (4.4.3-1) is then obtained.

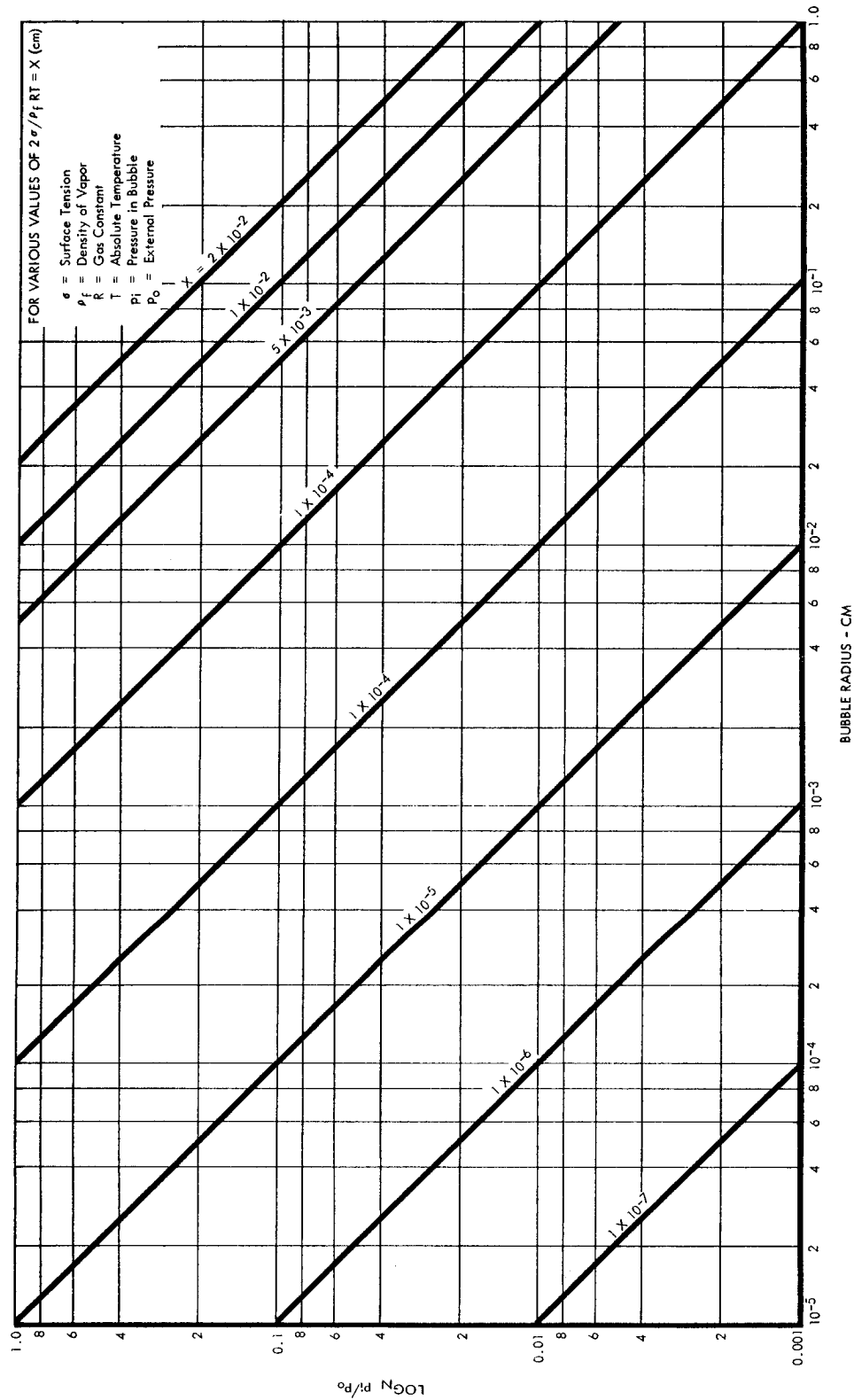


FIGURE 4.4.3-1



4.4.4 Applications of the Similarity Parameters

A demonstration of the usefulness of the similarity parameters obtained above will now be presented. Because of the difficulty of evaluating $r_b/r_{i,t}$ (from Section 4.4.3), we concentrate on the independent quantities in equation (4.4.2-4); viz.,

$$\phi = \frac{V_{m,i}}{U_{i,t}} = \frac{Q}{r_{i,t}^3 N \times 2\pi^2 (1 - \xi_i^2)} \quad (4.4.4-1)$$

$$Re = \frac{U_{i,t} r_{i,t}}{\nu} = \frac{r_{i,t}^2 N \times 2\pi}{\nu} \quad (4.4.4-2)$$

$$\tau = \frac{2g_o(P_i - p_{sat})}{\rho_f U_{i,t}^2} = \frac{2g_o NPSH}{r_{i,t}^2 N^2 \times 4\pi^2} \quad (4.4.4-3)$$

$$\Theta = \left(\frac{ds_f}{dp} \right)_{sat} \frac{\rho_f}{g_o} \frac{U_{i,t}^2}{s_{fg,sat}} \left(\frac{\rho_f}{\rho_g} - 1 \right)_{sat} = \frac{\rho_f \mathcal{F}}{g_o} N^2 r_{i,t}^2 \times 4\pi^2 \quad (4.4.4-4)$$

These give the flow field results which are characteristically represented by:

$$\psi = \frac{g_o (P_2 - P_1)}{\rho_f U_{i,t}^2} = \frac{g_o (P_2 - P_1)}{\rho_f r_{i,t}^2 N^2 \times 4\pi^2} \quad (4.4.4-5)$$

For complete similarity, the four independent quantities listed above must be respectively identical in the case of the scale model tests and of the prototype. Now a practical problem arises: If we hold ϕ , Re , and τ constant, we must look around for a fluid which will give the same Θ in the two cases. We need not be so stringent if we have some knowledge of Reynolds number effects and if we observe that small changes in large values of Re have very little influence on the results. (See Section 4.7.3). Thus, with some caution in this regard, we may require that only ϕ , τ , and Θ be maintained constant. As is usually the case, the test and prototype fluids are already chosen; so, to maintain Θ constant, equation (4.4.4-4) indicates the need for a speed (N) change only, for chosen fluids and scales (values of \mathcal{F} and $r_{i,t}$). As equations (4.4.4-1) and (4.4.4-3) show, the required values of Q and $NPSH$ to maintain ϕ and τ can then be selected without changing Θ .

Other restrictions on freedom of selection for the model test and the prototype conditions are the avoidance of excessive Reynolds number differences and possible bubble diameter effects. Approximate values of $\rho_f T / g_0$ computed from tables of thermodynamic properties in references 6, 16, 17 are as follows:

TABLE 4.4.4-1

VALUES OF FLUID THERMODYNAMIC PARAMETER

<u>Fluid and Temperature</u>	$\frac{\rho_f T}{g_0} \left(= \frac{\Theta}{v_{1,t}^2} \right)$ sec ² /ft ²
Oxygen at 162°R (= 90°K)	0.020
Hydrogen at 36°R (= 20°K)	0.00020
Water at 82°F	26.7
Water at 105°F	7.38
Water at 200°F	0.118
Water at 300°F	0.0063
Water at 400°F	0.00053
Water at 450°F	0.00021
Water at 500°F	0.00009

As a basic example, we might ask that tests be run to predict the performance of the following:

PROTOTYPE INDUCER

Inlet Diameter	8 in.
Inlet Hub-Tip Ratio	0.4
Fluid	36°R Liquid Hydrogen
Speed, N	30,000 rpm
Outlet Volume Flow Rate	14,000 gpm
Net Positive Suction Pressure	5 psi
Expected Total Pressure Rise	150 psi

We could then choose (on the basis of test facility availability, etc.) the following tests:

- Test No. 1 - Run the 8 inch diameter prototype in 300°F water.
(Different Fluid)
- Test No. 2 - Run a 4 inch diameter scale model in 36°R liquid hydrogen.
(Different Scale)
- Test No. 3 - Run the 4 inch diameter scale model in 300°F water.
(Different scale and fluid)



Two questions then arise:

What values of flow, speed, and $(P_1 - P_{sat}) (= \rho_f NPSH)$ are required for similarity of these tests with the prototype 30,000 rpm hydrogen requirement, and what pressure rises may be expected? As discussed above, since the operating fluids (and, therefore, ρ) are chosen, we shall satisfy similarity only in ϕ , τ , and Θ and shall simply note the Re difference in each case. Application of equations (4.4.4-1) through (4.4.4-5), using the values of $\frac{\rho_f \mathcal{I}}{\rho_o}$ in Table 4.4.4-1, yielded the following set of requirements and results for these tests:

TABLE 4.4.4-2

CONDITIONS OF DYNAMIC SIMILARITY

Test	Fluid @ Temp.	Scale	Outlet Volume Flow Q gpm	Speed N rpm	NPSP ($P_1 - P_{sat}$) psi	Expected Pressure Rise $P_2 - P_1$ psi
Prototype	36°R Hydrogen	Full	14,000	30,000	5.00	150
No. 1	300°F Water	Full	2,520	5,400	0.42	12.6
No. 2	36°R Hydrogen	1/2	3,500	60,000	5.00	150
No. 3	300°F Water	1/2	630	10,800	0.42	12.6
No. 4*	450°F Water	1/2	3,500	60,000	11.6	348

Test	Flow Coefficient ϕ	Cavitation Parameter τ	Thermodynamic Parameter Θ	Reynolds Number Re
Prototype	0.1015	0.00950	0.440	17×10^7
No. 1	"	"	"	3.1×10^7
No. 2	"	"	"	8.5×10^7
No. 3	"	"	"	1.5×10^7
No. 4*	"	"	"	17×10^7

*Test No. 4 is discussed in the next paragraph.

The results of Table 4.4.4-2 show Test No. 3 to have one order of magnitude in R_e lower than the prototype. If it is necessary to run a 1/2 scale water test with R_e equal to that of the prototype, we need to substitute Test No. 4 for Test No. 3. However, the very hot high-pressure water and the high-pressure rise of Test No. 4 could be prohibitive from an expense standpoint, for simply duplicating Reynolds numbers. $\frac{\rho_f g}{\gamma_o}$ is the same in 450°F water as in 36°R liquid hydrogen; and if it is felt that different values of this number lead to performance variations due to other real fluid effects, such as that of the bubble parameter $r_b/r_{i,t}$, Test No. 4 might indeed be justifiable.

4.4.5 Net Positive Suction Head Requirements

The rather simple form of the state equation (4.4.2-17) suggests the existence of a criterion for \mathcal{T} (and, therefore, NPSH) in various fluids having different values of the thermodynamic properties contributing to Θ . (Θ is affected by inducer tip speed also.) The theory has been advanced that the volume ratio of vapor to liquid V/L that exists at some point in the machine, say at the point of minimum pressure co-efficient \hat{p}_{min} , is the primary variable controlling head rise during cavitating operation, regardless of the fluid used¹⁸. The V/L ratio is defined as follows:

$$\frac{V}{L} = \frac{\rho_f}{\rho_g} \left(\frac{\chi}{1-\chi} \right) \quad (4.4.5-1)$$

or with equation (4.1.2-7) for χ , this becomes

$$\frac{V}{L} = \left(\frac{\rho_f}{\rho_g} \right)_{sat} \left\{ \frac{\left[\left(\frac{ds_f}{dp} \right)_{sat} \frac{(p_{sat} - p)}{s_{fg, sat}} \right]}{1 - \chi} \right\} \quad (4.4.5-2)$$

and with the definitions of Section 4.4.2,

$$\frac{V}{L} = \frac{-\Theta \left(\frac{\mathcal{T}}{2} + \hat{p} \right)}{(1-\chi)} \times \frac{\frac{\rho_f}{\rho_g}}{\left(\frac{\rho_f}{\rho_g} - 1 \right)} \quad (4.4.5-3)$$

Now, if $\frac{\rho_f}{\rho_g} \gg 1$ and $\chi \ll 1$, we may simplify equation (4.4.5-3) to obtain

$$\frac{V}{L} = -\Theta \left(\frac{\mathcal{T}}{2} + \hat{p} \right) \quad (4.4.5-4)$$

This and equation (4.4.2-17) yield the relationship between mixture density and the $\frac{V}{L}$:

$$\hat{\rho} = \frac{1}{1 + \frac{V}{L}} \quad (4.4.5-5)$$

or

$$\frac{V}{L} = \frac{\rho_f}{\rho} - 1 \quad (4.4.5-6)$$

It must be noted that this concept of the vapor-to-liquid ratio being a form of the two-phase mixture density ρ holds only if the mass of the vapor present is a negligible fraction of the mixture mass ($\frac{\rho_v}{\rho} \gg 1$ and $X \ll 1$).

VAPOR-TO-LIQUID VOLUME RATIO DISTRIBUTIONS ON INDUCER BLADES
(FOR SAME V/L MAX, \hat{p} , BUT FOR TWO DIFFERENT VALUES OF Θ
AND, THEREFORE, FOR TWO DIFFERENT VALUES OF τ .)

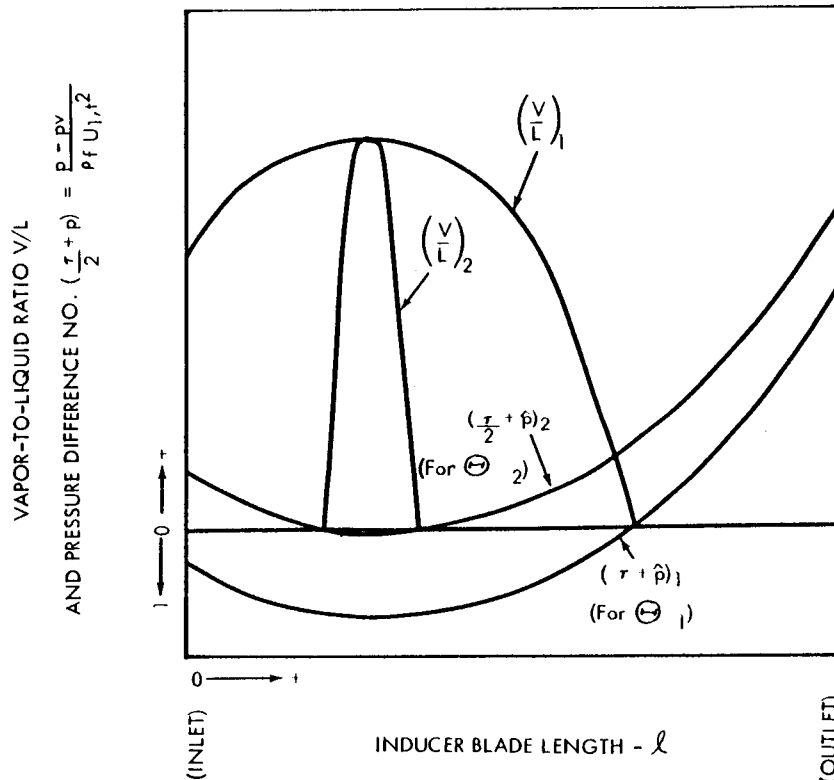


FIGURE 4.4.5-1

Figure 4.4.5-1 shows the $\frac{V}{L}$ vs l (blade length along a streamline) distributions along an inducer blade that can be obtained for two different values of Θ , but for the same maximum $\frac{V}{L}$ and minimum \hat{p} . The shape of the pressure curve is maintained constant although its level is different, as determined by the τ requirement which is obtained from equation (4.4.5-4) as follows:

$$\frac{\tau}{2} = \frac{V}{L} - \hat{p} \quad (4.4.5-7)$$

where $\hat{p} = \hat{p}_{min}$ in the present discussion. Under these conditions (different τ and Θ), it can be seen that the inducer flow field is quite different, even though the maximum $\frac{V}{L}$ is the same. It must be admitted that the shapes of the pressure vs l curves must also be different under the conditions pictured due to cavitation, however, $\frac{V}{L}$ differences along the blades and from blade to blade still exist. This simply leads to the statement that is implicit in equation (4.4.2-4); i.e., complete dynamic similarity requires that all the parameters be alike, including τ and Θ .

Thus, there is some difficulty with the $\frac{V}{L}$ criterion. However, if the portion of the flow channel that experiences vaporization were very small (i.e., if the pressure drop were sudden, but existed for only a short period), the $\frac{V}{L}$ theory would be more acceptable. This is more likely to be the case in a conventional pump impeller with a short, heavily loaded blade, as opposed to the long inducer type of blading.

Stepanoff has applied this criterion of constant $\frac{V}{L}$ to a set of test results to determine the change in NPSH requirements of the same machine when it is to operate at the same speed and volume flow rate in a different fluid¹⁹. He uses the symbol "B" for $\frac{V}{L}$.

If satisfactory dynamic similarity could be obtained, the value of the $\frac{V}{L}$ method would be unquestioned, both from the standpoint of additional flexibility in scaling and in correlation of performance among fluids and from the viewpoint of the resulting NPSH criterion (equation (4.4.5-7)).

At present, the $\frac{V}{L}$ method is the only analytical approach to the problem of NPSH requirements in different fluids; i.e., to the problem of describing the effects of variation in the thermodynamic parameter Θ .

4.5 ADVANCED DESIGN CRITERIA

4.5.1 Introduction

The optimum inducer configuration is one that is capable of operating at the lowest inlet pressure and the highest speed (and efficiency) possible for a given flow rate. To a systems engineer, the state of the art is best expressed in these terms. Much work has been done to determine the approximate values of inducer design parameters that are required to maximize these capabilities and many of the conclusions have been reached on the basis of single-phase flow studies; however, a fortuitous combination of circumstances makes them generally applicable to the two-phase or cavitating flow that ordinarily occurs in an inducer.²⁰ As will be shown, this enables one to size and, with some further skill, to design an inducer that will have reasonable performance. However, more particular studies of the internal flow and blading are required if further progress is to be achieved. The ability to analyze the flow field has led to the results that are presented in Section 4.7. These, together with studies of two-phase flow, will make possible the creation of required distributions of such fluid properties as density, pressure, and relative velocity as are necessary for optimum performance. These very basic design criteria then lead to a blading that can produce such distributions. The work discussed further along in this connection includes the two-phase flow studies that were made and indicates how they must be applied to obtain information on such design criteria.

4.5.2 Relations of Parameters and Sizing Methods

The main objectives of an inducer design are imposed by the system requirements that weight and upstream pressurization be minimized. The degree to which these ideals are achieved is generally well expressed by the maximum obtainable value of the suction specific speed, S :

$$S = \frac{N \sqrt{Q}}{\left(\frac{P_i - P_{sat}}{\rho_f / g_0} \right)^{3/4}} \quad (4.5.2-1)$$

This can be expressed in terms of parameters more closely associated with the actual inducer design by substitution of equations (4.4.4-1) and (4.4.4-3) into equation (4.5.2-1):

$$S = \frac{\sqrt{\frac{\phi}{4\pi} (1 - \xi_1^2)}}{\left(\frac{\tau}{2} \right)^{3/4}} \quad (4.5.2-2)$$

Furthermore, since

$$\tau = k (1 + \phi^2) + \phi^2 \quad (4.5.2-3)$$



where k , the blade to tip cavitation number, is defined as

$$k = \frac{2g_0 (p_i - p_{sat})}{\rho_f W_{1,t}^2} \quad (4.5.2-4)$$

We may rewrite equation (4.5.2-2) as follows:

$$S = \frac{\sqrt{1 - \xi_1^2}}{\phi \sqrt[4]{2\pi^2 \left[1 + k \left(1 + \frac{1}{\phi^2}\right)\right]^{3/4}}} \quad (4.5.2-5)$$

Differentiating this with respect to ϕ enables us to find the optimum value of ϕ that will give maximum S for given k :

$$\phi_{opt} = \sqrt{\frac{k}{2(k+1)}} \quad (4.5.2-6)$$

The accompanying optimum value of τ for this k is found by introducing equation (4.5.2-6) into equations (4.5.2-3) and (4.5.2-5):

$$\tau_{opt} = \frac{3k}{2} \quad (4.5.2-7)$$

And so

$$S_{max} = \sqrt{\frac{1 - \xi_1^2}{\pi k}} \sqrt{\frac{2}{27(1+k)}} \quad (4.5.2-8)$$

Now we are able to size the inducer for given Q and NPSH $\left(= \frac{p_i - p_{sat}}{\rho_f}\right)$ by selecting ξ (usually held to a minimum dictated by mechanical considerations) and k .

This sizing is accomplished by obtaining the speed and the inlet radius, which determine the basic design. We obtain the speed N from equation (4.5.2-1) using S_{max} from equation (4.5.2-8):

$$N = \frac{S_{max} (g_0 \text{ NPSH})^{3/4}}{\sqrt{Q}} \quad (4.5.2-9)$$

The radius is obtained from equation (4.4.4-1) as follows:

$$r_{1,t} = \sqrt[3]{\frac{Q}{2\pi^2 \phi_{opt} N (1 - \xi_1^2)}} \quad (4.5.2-10)$$

where ϕ_{opt} is found from equation (4.5.2-6).

These results (equations (4.5.2-9) and (4.5.2-10)) are based on the idea that there is a minimum positive value of k below which the inducer operation is unsatisfactory because of cavitation. This minimum k depends on the fluid and on the design of the blading. For single phase flow at the inducer inlet, $k \geq 0$. If it is possible to operate at $k = 0$, equation (4.5.2-5) becomes

$$S_{(k=0)} = \frac{\sqrt{1 - \xi_1^2}}{\phi \sqrt{2\pi^2}} \quad (4.5.2-11)$$

where, by reason of its definition, ϕ cannot be zero. If ϕ is too small and the blades are set a correspondingly small angle β_b , the blade thickness will result in a blockage that increases the required k .

Note that the case of $k = 0$ amounts to the condition that

$$V_{m,1} = \sqrt{\frac{2 g_0 (P_1 - P_{sat})}{\rho_f}} = \sqrt{2 g_0 NPSH} \quad (4.5.2-12)$$

and so the minimum possible inlet size for single-phase flow is obtained by combining equations (4.4.4-1) and (4.5.2-12) to obtain

$$r_{1,t,min} = \sqrt{\frac{Q}{\pi (1 - \xi^2) \sqrt{\frac{2 g_0 (P_1 - P_{sat})}{\rho_f}}}} \quad (4.5.2-13)$$

(single phase at inlet)

Experience has shown that fluids with large \mathcal{F} values (see Table 4.4.4-1) have little ability to be handled in the two-phase state ($k \geq 0$). Thus $r_{1,t}$ cannot be smaller than the single-phase minimum value of equation (4.5.2-13). When two-phase flow can be accommodated at inlet ($k < 0$, low \mathcal{F}), $r_{1,t}$ can be smaller, and $(P_1 - P_{sat})$ can be zero or even negative. In such a case, the idea of S becomes meaningless. However, the system requirement of reducing tank pressurization and pump weight still applies. Thoughts on the two-phase flow criteria for inducer design are discussed in Section 4.5.3.

4.5.3 Design Considerations for the Internal Flow Field

The basic design problem is to prevent vapor-choking of the flow passages due to sharp pressure drops, below vapor pressure,¹. These drops occur because of blade thickness blockage or localized high blade loadings that create low pressures on the suction sides of the blades. The problem is to make the proper compromise between blockage and loading. To make this compromise, one must consider the question of what loading should be used, because when NPSH is low enough, the inlet portion of the blade unloads due to fluid vaporization. (The resulting lower average density raises V_m (See Figure 4.2.1-2), reducing V_θ and, therefore, the loading.) The downstream portions then



begin to load instead, as must occur if the fluid there is being compressed and the density raised. It is interesting to note that inducer passages are long and narrow because of the high solidity that results from the low value of blade angle β_b' (discussed above). It appears that such passages are in turn conducive to the necessarily steady, controlled motion of vaporizing fluid in the upstream, unloaded portions of the blading.

The loading-shift phenomenon introduces the problem of avoiding excessive loading that causes separation and its attendant inefficiency, which is due to marked decreases in the fluid relative velocity W in the areas affected. Section 4.7.3 shows some typical blade loadings and what may be expected when these shifts occur (see Figures 4.7.3-2 to 4.6.3-5).

If the fluid entering the inducer is two-phase, conditions arise that limit the mass flow rate²¹. It is of interest to note that if the meridional velocity V_m ever gets large enough (due to vaporization), the resulting negative loading would produce a general pressure drop and consequently a density drop, a V_m increase, and a further pressure drop. This limiting situation of negative loading in a quality mixture means that V_m must be limited at inlet to its value for zero loading, and a corresponding limit on the two-phase inlet volume flow rate results.

This leads to useful conclusions about inducers which must handle quality mixtures. For example, in a given inducer operating at a fixed speed, the lower the outlet volume flow rate, the higher is the quality that is possible at inlet. The important thing is that the inlet volume flow rate is limited quite sharply by the negative loading criterion.

The following two-phase flow cases can exist in an inducer and also impose mass flow limits similar to that of the special case illustrated above:

- a. Flow with zero energy addition in a constant area duct for a given rate of loss.
- b. Flow with zero energy addition and negligible loss in a duct of decreasing cross sectional area.
- c. Flows for various rates of energy addition in a constant area duct for different amounts of loss.

These limiting mass flow situations have direct bearing on inducer sizing and blading, and they need to be investigated in detail during the formulation of design criteria. For example, the decision of how much to load the inlet portion of the inducer depends on the trade-off between case (a) (no loading) and case (c) which has the adverse effects of vapor formation due to pressure differences on the two sides of the channel. The influence of case (b) also needs to be considered, since it gives the contribution of the inevitable increasing blade thickness at inlet. Case (b) has another more comprehensible application to the sizing of inducer inlets. For tank-mounted applications, this gives the minimum diameter for a given mass flow, assuming that the resulting two-phase fluid could be handled by the inducer.

4.5.4 One-Dimensional Homogeneous Two-Phase Flow

Two illustrations of the utility of the equations of the flow model in obtaining conclusions about equilibrium, homogeneous two-phase duct flow have been made. The first gives a summary of the fluid properties at various conditions of flow through the throat of a nozzle; the other calculates the fluid state properties for a fixed mass flow from a tank through a length of inlet line to an inducer inlet. There are many other possibilities with different loss distributions, etc., which could lead to answers for the three flow cases outlined in Section 4.5.3.²²

4.5.4.1 Two-Phase Flow in a Nozzle

The nozzle flow problem that was solved assumes that a saturated liquid starts from stagnation upstream and proceeds isentropically to the throat of the nozzle. For this, one starts with the energy equation for absolute motion along a streamline with zero loss (see Equation (4.1.1-12)):

$$g_0 \frac{dp}{\rho} = -V dV \quad (4.5.4-1)$$

and from equation (4.1.2-8), we obtain the state relation between pressure and density:

$$\rho = \rho_f \left[\frac{1}{1 + g(p_{sat} - p)} \right] \quad (4.5.4-2)$$

or

$$p = p_{sat} + \frac{1}{g} - \frac{1}{\rho} \left(\frac{\rho_f}{g} \right) \quad (4.5.4-3)$$

Equation (4.5.4-3) substituted into (4.7.4-1) gives

$$\frac{g_0 \rho_f}{g} \frac{d\rho}{\rho^3} + V dV = 0 \quad (4.5.4-4)$$

Now since continuity states that

$$\frac{w}{A} = \rho V \quad (4.5.4-5)$$

we may integrate equation (4.5.4-4) as follows:

$$\frac{g_0 \rho_f}{g} \int_{\rho_f}^{\rho_T} \frac{d\rho}{\rho^3} = - \int_0^{\frac{w}{A_T \rho_T}} V dV \quad (4.5.4-6)$$



This gives the mass flow per unit area at the throat; viz.,

$$\frac{w}{A_T} = \sqrt{\frac{g_0 \rho_f}{g} \left(1 - \frac{\rho_T^2}{\rho_f^2}\right)} \quad (4.5.4-7)$$

It is quite possible for a flow passage of this type to be required to handle the same mass flow rate under single-phase liquid and two-phase liquid conditions because of variation in upstream pressure. Thus it is desired to express this $\frac{w}{A_T}$ in terms of the velocity that would exist if this flow were in liquid form. This is especially required for design purposes when the throat is the inlet to an inducer. For this reason we may write equation (4.5.4-7) as

$$\rho_f V_{T,(f)} = \sqrt{\frac{g_0 \rho_f}{g} \left(1 - \frac{\rho_T^2}{\rho_f^2}\right)} \quad (4.5.4-8)$$

The corresponding maximum exists for $\rho_T \rightarrow 0$ as follows:

$$\left(\frac{w}{A_T}\right)_{\max} \quad (\rho_T \rightarrow 0) = \rho_f V_{T,(f),\max} = \sqrt{\frac{g_0 \rho_f}{g}} \quad (4.5.4-9)$$

Of course this limit also gives

$$\lim_{\rho_T \rightarrow 0} V_T = \infty \quad (4.5.4-10)$$

a situation which, for reasons of the two-phase volume flow limit discussed in Section 4.5.3, cannot be accepted at an inducer inlet. Of course, ρ cannot be zero unless $p_{sat} - p$ is infinite (see equation (4.5.4-2)). Also, this hypothetical condition of zero ρ is not physically possible and represents a limitation of the assumptions made in Section 4.1.2 for the equation of state (4.1.2-8). However, practical applications for inducers are for ρ_T not very much smaller than ρ_f (low quality). Figure 4.5.4-1 illustrates the results of plotting equation (4.5.4-7). Numerical calculations of equation (4.5.4-7) in Figure 4.5.4-1 yield the following:

$$\frac{w}{A_T} = 314 \sqrt{1 - \left(\frac{\rho_T}{\rho_f}\right)^2} \quad \frac{\text{lbm}}{\text{sec-ft}^2}$$

or

$$V_{T,(f)} = 70.7 \sqrt{1 - \left(\frac{\rho_T}{\rho_f}\right)^2} \quad \frac{\text{ft}}{\text{sec}}$$

TWO-PHASE FLOW IN THE THROAT OF A NOZZLE

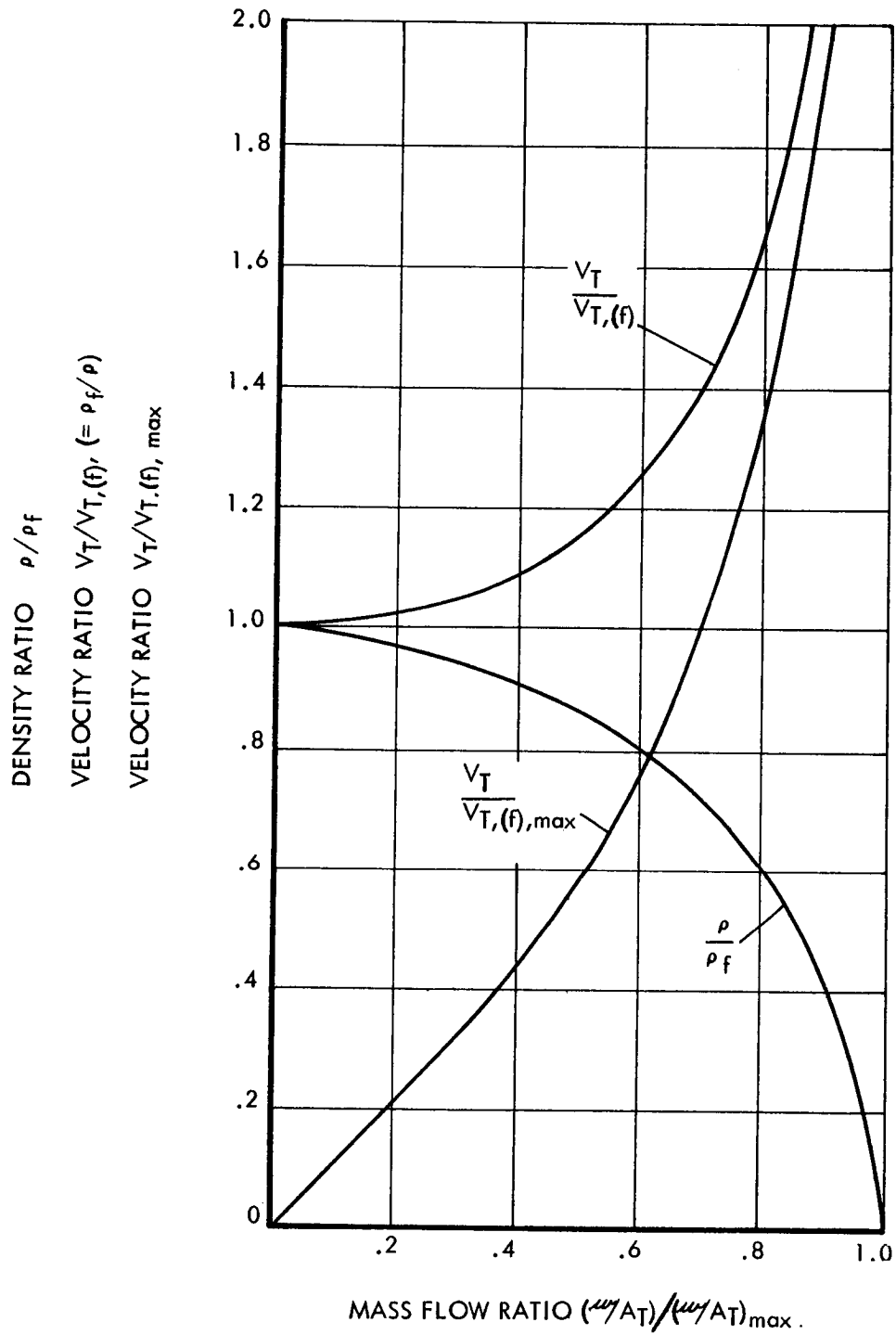


FIGURE 4.5.4-1



whereby

$$V_T = \left(\frac{\rho_f}{\rho_T} \right) \times 70.7 \sqrt{1 - \left(\frac{\rho_T}{\rho_f} \right)^2} \frac{ft}{sec}$$

Specifically, if we require $\left(\frac{V}{L} \right)_T = 1$, equation (4.4.5-6) yields $\frac{\rho_f}{\rho_T} = 2$ and

$$\frac{w}{A_T} = 261 \frac{lbm}{sec-ft^2}$$

$$V_{T,(f)} = 61 \text{ ft/sec}$$

$$V_T = 122 \text{ ft/sec}$$

It is this latter number V_T which governs the inducer inlet blade angle setting (rather than $V_{T,(f)}$) if the limiting, two-phase negative-loading situation described in Section 4.5.3 is to be avoided.

4.5.2.2 Two-Phase Flow in an Inducer Test Set Up

Determination of the two-phase fluid flow properties upstream of the inducer for an actual test in a set-up of the type used in Section 4.6 will now be made. The problem is to find the state properties at inducer inlet when a given fluid undergoes the following process (see Figure 4.5.4-2):

- A lossless acceleration of fluid from stagnation in the tank at a given pressure (on the pump centerline) into the inlet line just outside the tank, from (o) to (a).
- Two-phase flow with one-dimensional pipe loss from (a) to (b) (upstream of the inducer).
- Lossless one-dimensional acceleration over the hub to the inducer blade leading edges from (b) to (1).

This example is the most general case with regard to the type of two-phase flow calculations involved.

By a procedure similar to the one discussed above, the answer to step (a) is obtained from

$$\frac{\rho_a}{\rho_f} = \sqrt{\frac{1 - \frac{\rho_f g}{g_o} \left(\frac{w}{\rho_f A_a} \right)^2}{1 - \frac{\rho_f g}{g_o} (V_{sat})^2}} \quad (4.5.4-11)$$

ANALYSIS OF FLUID STATE AT INDUCER INLET FOR TWO-PHASE FLOW

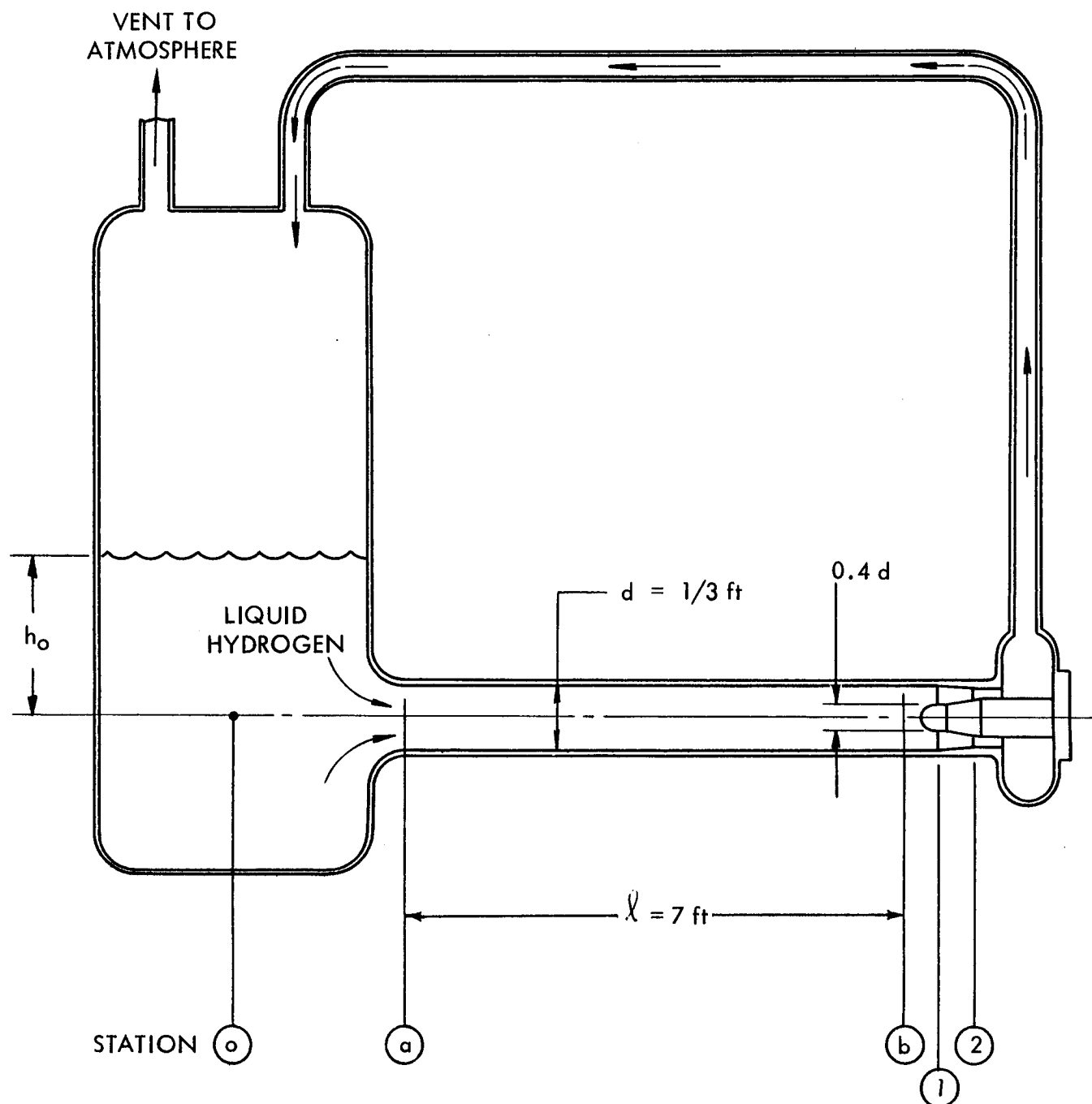


FIGURE 4.5.4-2



The other variables p_a and V_a are obtained from equations (4.5.4-3) and (4.5.4-5) respectively, and where

$$V_{sat}^2 = \frac{2g_o}{\rho_f} (p_o - p_{sat}) \quad (4.5.4-12)$$

Step (b) is determined by first adding the loss term to equation (4.5.4-1) and, therefore, to (4.5.4-4) (cf. equation (4.1.1-12)). As in equation (4.1.3-2), the loss is given by

$$dL = \frac{f}{2d} V^2 d\ell \quad (4.5.4-13)$$

and so in place of equation (4.5.4-4), we now need to integrate the following: ($A_a = A_b$)

$$\frac{f}{2d} \left(\frac{w}{A_b} \right)^2 \int_0^{\ell} d\ell = \left[\left(\frac{w}{A_b} \right)^2 - \frac{g_o \rho_f}{g} \right] \int_{p_a}^{p_b} \frac{dp}{\rho} \quad (4.5.4-14)$$

which gives (for constant f),

$$\frac{p_b}{p_a} = \frac{1}{\exp \left[\frac{f\ell / (2d)}{\frac{g_o \rho_f}{g} \times \frac{A_b^2}{w^2} - 1} \right]} \quad (4.5.4-15)$$

or, if we use the equivalent liquid volume flow rate $Q(f)$ (that exists at inducer outlet), where

$$Q(f) = \frac{w}{\rho_f} \quad (4.5.4-16)$$

$$\frac{p_b}{p_a} = \frac{1}{\exp \left[\frac{f\ell / (2d)}{\frac{g_o}{\rho_f g} \frac{A_b^2}{Q(f)^2} - 1} \right]} \quad (4.5.4-17)$$

We may now combine equations (4.5.4-11), (4.5.4-12), and (4.5.4-17) to obtain

$$\frac{\rho_b}{\rho_f} = \frac{\sqrt{\frac{1 - \frac{\rho_f g}{g_o} \left(\frac{Q(f)}{A_b} \right)^2}{1 - \frac{\rho_f g}{g_o} \left[\frac{2 g_o (\rho_o - \rho_{sat})}{\rho_f} \right]}}}{\exp \left[\frac{f l / (2 d)}{\frac{1}{\frac{\rho_f g}{g_o} \left(\frac{Q(f)}{A_b} \right)^2} - 1}} \right]} \quad (4.5.4-18)$$

where the range of flow per unit area is found from the following mathematical requirement on equation (4.5.4-18)

$$\frac{2 g_o (\rho_o - \rho_{sat})}{\rho_f} \leq \left(\frac{Q(f)}{A_b} \right)^2 \leq \frac{1}{\left(\frac{\rho_f g}{g_o} \right)} \quad (4.5.4-19)$$

This combines steps (a) and (b) of the problem.

Step (c) is solved by integrating equation (4.5.4-4) as follows:

$$\frac{g_o \rho_f}{g} \int_{\rho_b}^{\rho_1} \frac{d\rho}{\rho^3} = - \int_{\frac{w}{\rho_b A_b}}^{\frac{w}{\rho_1 A_1}} \frac{1}{V} dV \quad (4.5.4-20)$$

whereby, with equation (4.5.4-16),

$$\frac{\rho_1}{\rho_b} \sqrt{\frac{\left(\frac{\rho_f Q(f)}{A_1} \right)^2 - \frac{g_o \rho_f}{g}}{\left(\frac{\rho_f Q(f)}{A_b} \right)^2 - \frac{g_o \rho_f}{g}}} \quad (4.5.4-21)$$

We now assume that these results are adequate for numerically evaluating the state of the liquid hydrogen at the inducer inlet for the test conditions of Data Point No. 19 of Table 4.6.5-2.



Given:

$$\frac{p_o - p_{sat}}{\rho_f} = 2.4 \frac{\text{ft} \cdot \text{lbf}}{\text{lbfm}} \quad (h_o = 2.4 \text{ ft})$$

$$Q(f) = 1120 \text{ gpm} = 2.5 \frac{\text{ft}^3}{\text{sec}}$$

$$f = 0.00145 \frac{\text{ft}^2}{\text{lbf}}$$

$$\frac{\rho_f f}{g_o} = 0.0002 \frac{\text{sec}^2}{\text{ft}^2}$$

$$g_o = 32.2 \frac{\text{lbfm} \cdot \text{ft}}{\text{lbf} \cdot \text{sec}^2}$$

$$L = 7 \text{ ft}$$

$$d = 1/3 \text{ ft}$$

$$f = 0.015$$

$$A_a = A_b = \frac{\pi}{36} \text{ ft}^2$$

$$A_i = 0.84 \times A_b$$

$$\rho_f = 4.45 \frac{\text{lbfm}}{\text{ft}^3}$$

First we solve steps (a) and (b) by substituting the necessary values into equation (4.5.4-18)

$$\frac{p_b}{p_f} = \frac{\sqrt{\frac{1 - 0.0002 \left(\frac{2.5}{\pi/36} \right)^2}{1 - 0.0002 (64.4 \times 2.4)}}}{\exp \left[\frac{\frac{0.015 \times 7}{2 \times 1/3}}{\frac{1}{0.0002 \left(\frac{2.5}{\pi/36} \right)^2} - 1} \right]} \quad (4.5.4-22)$$

$$\frac{\rho_b}{\rho_f} = \frac{0.930}{e^{0.309}} \quad (4.5.4-23)$$

$$\frac{\rho_b}{\rho_f} = 0.900 \quad (4.5.4-24)$$

Finally we proceed to step (c), using equation (4.5.4-21):

$$\frac{\rho_i}{\rho_b} = \sqrt{\frac{\left(\frac{2.5 \times 4.45}{0.84 \times \pi/36}\right)^2 - \frac{(4.45)^2}{0.0002}}{\left(\frac{2.5 \times 4.45}{\pi/36}\right)^2 - \frac{(4.45)^2}{0.0002}}} \quad (4.5.4-25)$$

and

$$\frac{\rho_i}{\rho_b} = 0.957 \quad (4.5.4-26)$$

Thus equations (4.5.4-24) and (4.5.4-26) give

$$\begin{aligned} \frac{\rho_i}{\rho_f} &= 0.861 \\ \text{or } \rho_i &= 3.75 \frac{\text{lbm}}{\text{ft}^3} \end{aligned} \quad (4.5.4-27)$$

The inlet static pressure is obtained from equation (4.5.4-3)

$$p_i - p_{\text{sat}} = \left(\frac{1}{0.00145} - \frac{1}{0.861 \times 0.00145} \right) \frac{\text{lbft}}{\text{ft}^2} \quad (4.5.4-28)$$

whereby

$$p_i - p_{\text{sat}} = -110 \frac{\text{lbft}}{\text{ft}^2} = -0.764 \text{ psi}$$

The velocity at inlet is obtained from equation (4.5.4-5), (4.5.4-16), and (4.5.4-27):

$$\begin{aligned} V_i &= \frac{\rho_f}{\rho_i} \frac{Q(f)}{A_i} = \left(\frac{2.5}{0.861 \times 0.84 \times \pi/36} \right) \frac{\text{ft}}{\text{sec}} \\ V &= 39.6 \frac{\text{ft}}{\text{sec}} \end{aligned} \quad (4.5.4-29)$$



Other properties such as the temperature can be obtained from these results, using tables⁶.

The total inlet pressure is found by calculating the end pressure of a lossless process of stagnation from the state conditions at (1). Equation (4.5.4-6), integrated between the limits of such a process and combined with equation (4.5.4-3) gives

$$P_1 = P_{sat} + \frac{1}{g} \left[1 - \frac{\rho_f}{\rho_1} \sqrt{1 - \frac{\rho_f g}{g_0} \left(\frac{\rho_1}{\rho_f} \right)^2 V_1^2} \right] \quad (4.5.4-30)$$

This holds only if $P_1 \leq P_{sat}$. Otherwise one obtains

$$P_1 = P_{sat} + \frac{\rho_f}{2g_0} \left[V_1^2 + \frac{g_0}{\rho_f g} \left(1 - \frac{\rho_f^2}{\rho_1^2} \right) \right] \quad (4.5.4-31)$$

for $P_1 \geq P_{sat}$. For our case, equation (4.5.4-30) yields

$$P_1 - P_{sat} = -11.5 \frac{\text{lb f}}{\text{ft}^2} = -0.08 \text{ psi}$$

So the net positive suction head (NPSH) at the inducer inlet is

$$\frac{P_1 - P_{sat}}{\rho_f} = -2.6 \frac{\text{ft-lb f}}{\text{lb m}}$$

The results of these calculations are summarized in Table 4.5.4-1. Note that the actual two-phase volume flow rate at the inducer inlet Q_1 was 1300 gpm compared to the outlet liquid flow $Q(f)$ of the 1120 gpm obtained from the data. Since the optimum flow coefficient of the inducer required 1310 gpm at the speed of the test (cf. Table 4.6.5-2), we conclude that Q_b could have been a little larger before the flow limiting feature of negative loading would have prevented a still further increase (cf. Section 4.5.3).

As a matter of interest, the results of similar calculations for the hypothetical case where $P_0 - P_{sat} = 0$ also are presented in Table 4.5.4-1. That the effect of $(P_0 - P_{sat})$ is so small in this case may be seen by examination of equations (4.5.4-18) and (4.5.4-22). Results for this zero NPSH case also are given in Table 4.5.4-1.

In conclusion, the question remains as to the applicability of this theory from a standpoint of thermodynamic equilibrium, which we have assumed exists. Recent data obtained in static tests of liquid hydrogen²³ seem to indicate that in the dynamic case of turbulent flow which we are treating here, there is very little departure from equilibrium. This applies only to the special case of hydrogen flow.

TABLE 4.5.4-1

SUMMARY OF TWO PHASE HYDROGEN FLOW CALCULATIONS

Case	Description	Liquid Level Above Inlet	Density Ratios (see Figure 4.7.4-2)			
			$\frac{\rho_o}{\rho_f}$	$\frac{\rho_a}{\rho_f}$	$\frac{\rho_b}{\rho_f}$	$\frac{\rho_i}{\rho_f}$
I	Data Point No. 19 of Table 4.6.5-2	2.4	1	0.930	0.900	0.861
II	(Hypothetical)	0	1	0.915	0.885	0.847

Case	Outlet	Inlet Conditions			
	Liquid Volume Flow Rate	NPSH	Static Pressure Above Saturation	Velocity	Two-Phase Volume Flow Rate
	$Q(f)$ gpm	$\frac{P_i - P_{sat}}{\rho_f}$ ft-lbf/lbm	$P_i - P_{sat}$ psi	V_i $\frac{ft}{sec}$	Q_i gpm
I	1120	-2.6	-0.764	39.6	1300
II	1120	-5.1	-0.865	40.3	1322

4.6 TEST PROGRAM

To provide a base for verification and/or correlation of the theoretical results produced by the computer solution of the analytical flow model, a parallel test program was conducted to obtain performance data on a "referee" inducer. This testing was accomplished in a four-inch test vehicle operated in two test loops, one loop set up for water and the other for cryogenic fluids.

In the following discussion of the test vehicle, test program, and procedures, we will limit ourselves to those areas which concern only data output and neglect such items as detailed mechanical construction of the test vehicle, test loops, and operating controls. While significant engineering effort was required in these areas, this information does not concern the analytical technology aims of the program. Wherever practical, the mechanical configuration of the test vehicle, set-up, and instrumentation will be presented by figures in the form of photographs, schematics, or reduced drawings.

4.6.1 Test Vehicle

The overall design of the test vehicle is shown by Figure 4.6.1-1. Detail components are presented by an exploded view photo, Figure 4.6.1-2, while photographs of the assembled unit (with and without impeller shroud) are shown in Figures 4.6.1-3 and 4.6.1-4.

Basic design objectives to provide a "work horse" pump assembly that would not require significant mechanical development were as follows:

- a. The deep groove impeller thrust bearing and drive end roller bearing are submerged in the fluid and mounted in a rigid pintle that is directly aligned to the drive flange.
- b. The impeller shroud is a separate part that may be replaced and/or modified for various inducer configurations.
- c. The external construction is of light gage sheet metal so that deflections, caused by test loop piping or the thermal gradients that occur during cool down, will not be transmitted to the bearing suspension system.
- d. Dual back to back shaft seals are incorporated to provide a purge chamber for a helium gas barrier.

4.6.2 Test Inducer

To obtain test data that had the broadest possible application in regard to correlation and scaling laws, the referee inducer selected was based on a 6.5 inch, three bladed impeller suggested by NASA-LeRC.



INDUCER TEST VEHICLE

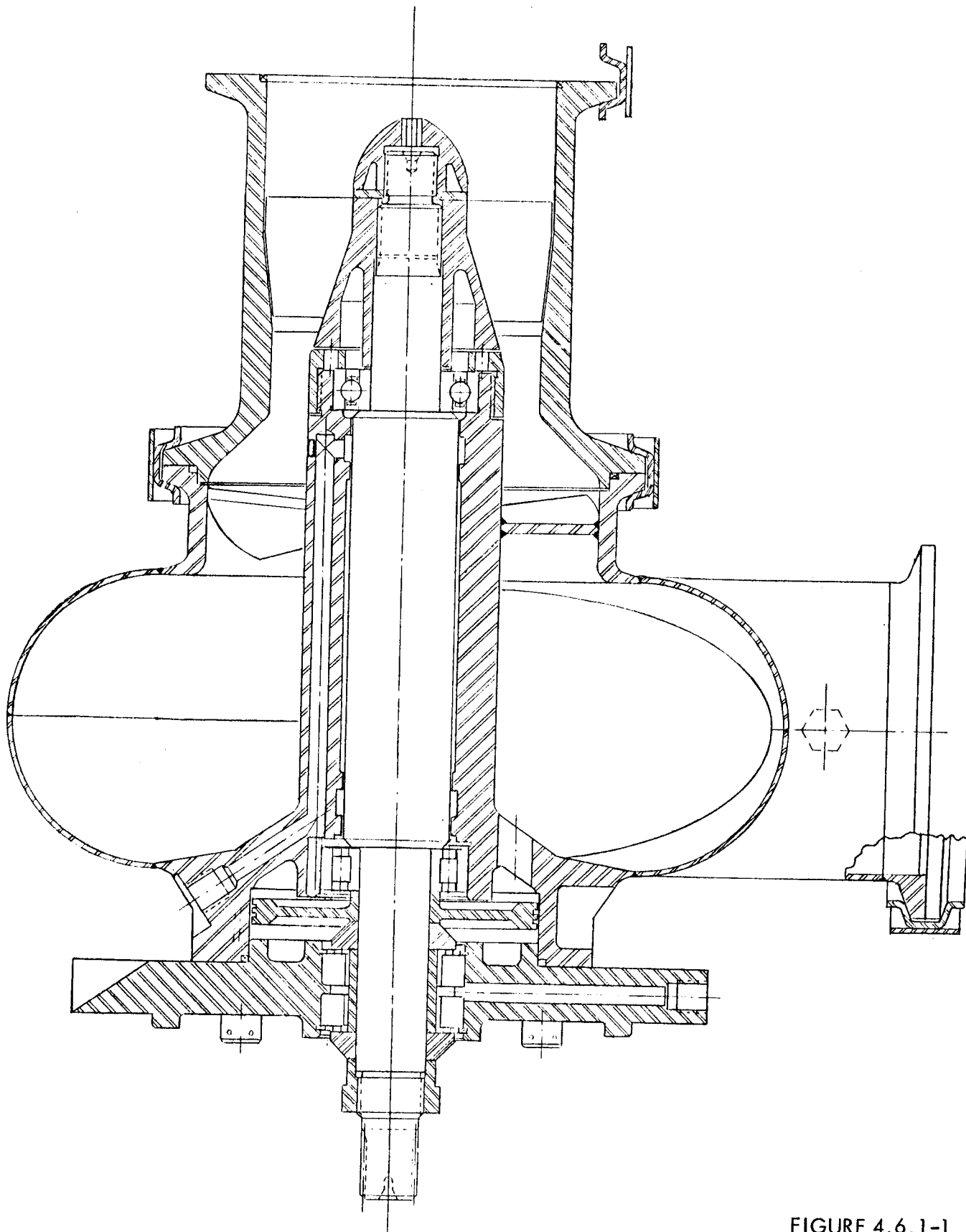
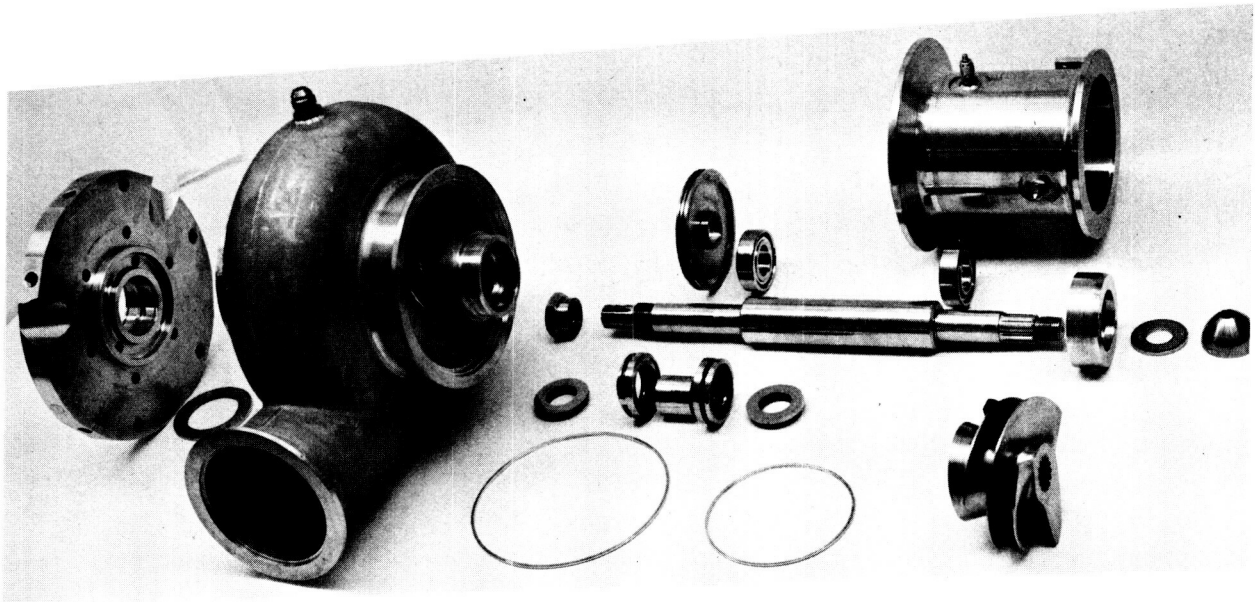
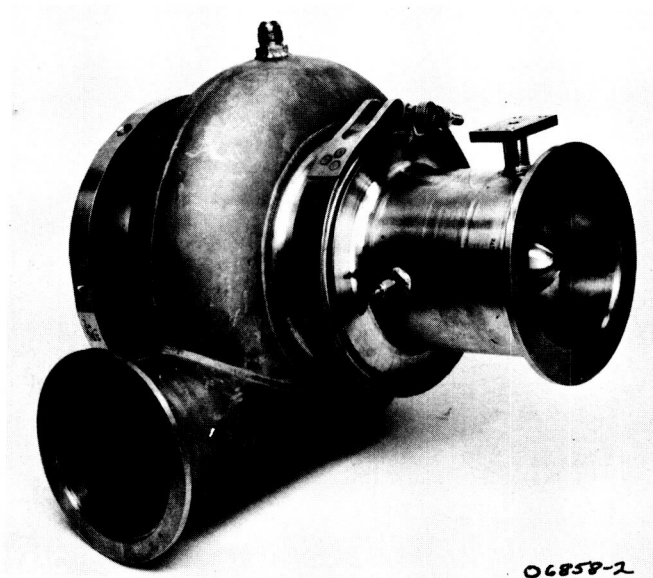


FIGURE 4.6.1-1



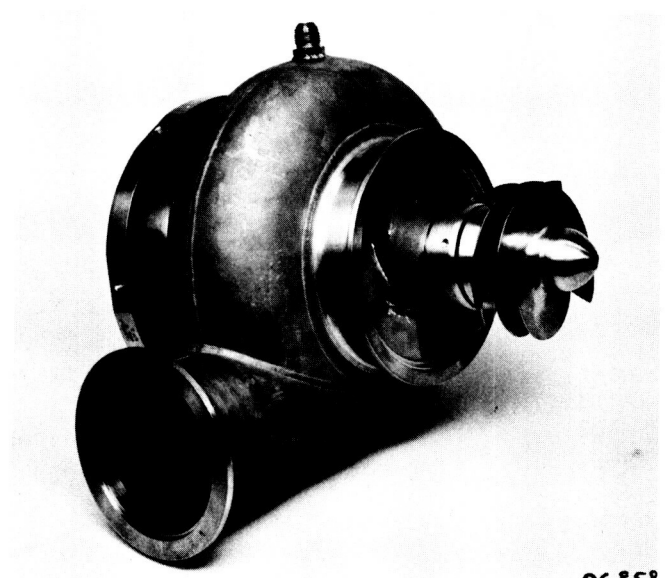
TEST VEHICLE DISASSEMBLED

FIGURE 4.6.1-2



TEST VEHICLE WITH SHROUD

FIGURE 4.6.1-3



TEST VEHICLE WITHOUT SHROUD FIGURE 4.6.1-4



The blade shape, composed of a flat plate inlet section faired into stacked circular arc blade elements, was produced by generating a 4/6.5 reduced master, NASA-LeRC supplied the 6.5 diameter sample impeller. The master was then used to produce the test part. Appendix C gives detailed information on the exact configuration and gage data.

4.6.3 Test Set-Up

As previously mentioned, two loops were installed, one for water and one for cryogenic testing. The test vehicle was directly coupled to a 500 horsepower dynamometer equipped with a cradled gear box capable of driving the unit to speeds over 40,000 rpm (see Figure 4.6.3-1).

4.6.3.1 Water Loop

The water loop was essentially a closed loop for deaeration purposes (see Figure 4.6.3-3). Both the tank suction and return lines incorporated low velocity sieve sections to prevent the creation of vortices and their propagation into the pump inlet.

During the initial layout of the test loops, the inlet line for the cryogenic set-up was optimized. The suction line in the water loop was consequently compromised, since a 90 degree bend was required. To minimize the effects of this bend, the suction line was enlarged to 6 inches and a long radius elbow located upstream from the 6 x 4 reducer and/or pump inlet. Figure 4.6.3-4 shows an overhead photo of the water loop installation.

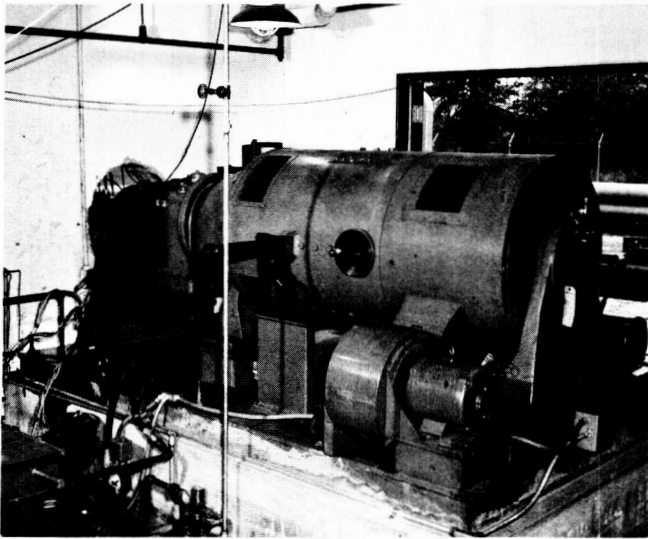
4.6.3.2 Cryogenic Loop

Figure 4.6.3-5 is a scaled schematic of the inlet line configuration, showing not only its mechanical construction but also the location of such instrumentation elements as vapor bulb and probes. These items will be discussed in detail in Section 4.6.4.

To provide optimum suction characteristics for a line mounted pump, the Dewar was modified to incorporate a 6-inch access port through the vacuum jacket. This permitted the use of a straight 4-inch inlet line with a submerged suction sieve inside the Dewar. Both the emergency shut-off valve and the bellows assembly were selected so that the continuity of the flow passage was maintained at 4 inches.

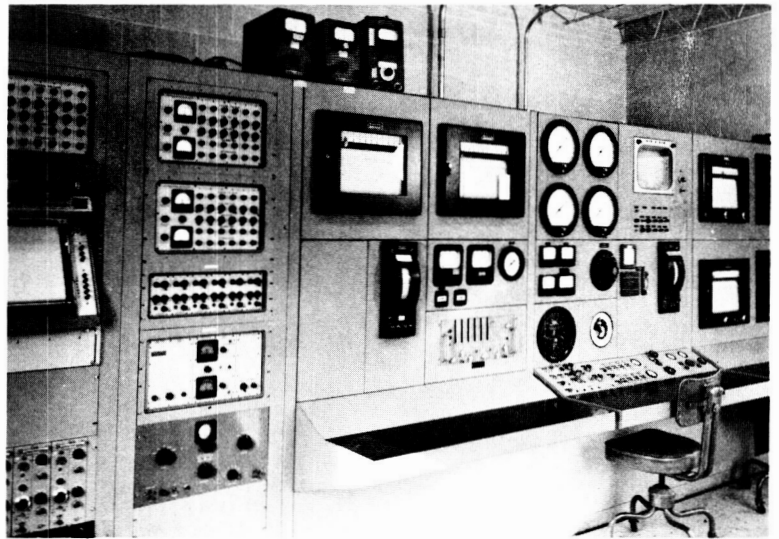
The pump discharge line (not shown on Figure 4.6.3-5) was routed to the top of the Dewar where another sieve was located. As mentioned in the description of the water loop, these sieves are for the purpose of eliminating vortices. Actually the vortex problem is more critical in the cryogenic test loop since there is a "free surface" in the Dewar at all times.

Figure 4.6.3-6 is a detail photo of the test vehicle installed in the cryogenic loop prior to the application of insulation. Figure 4.6.3-7 is an overall view of facility during filling, with the steam ejector activated. Figure 4.6.3-8 also shows the pump installation with the polyethylene insulation foamed in place.



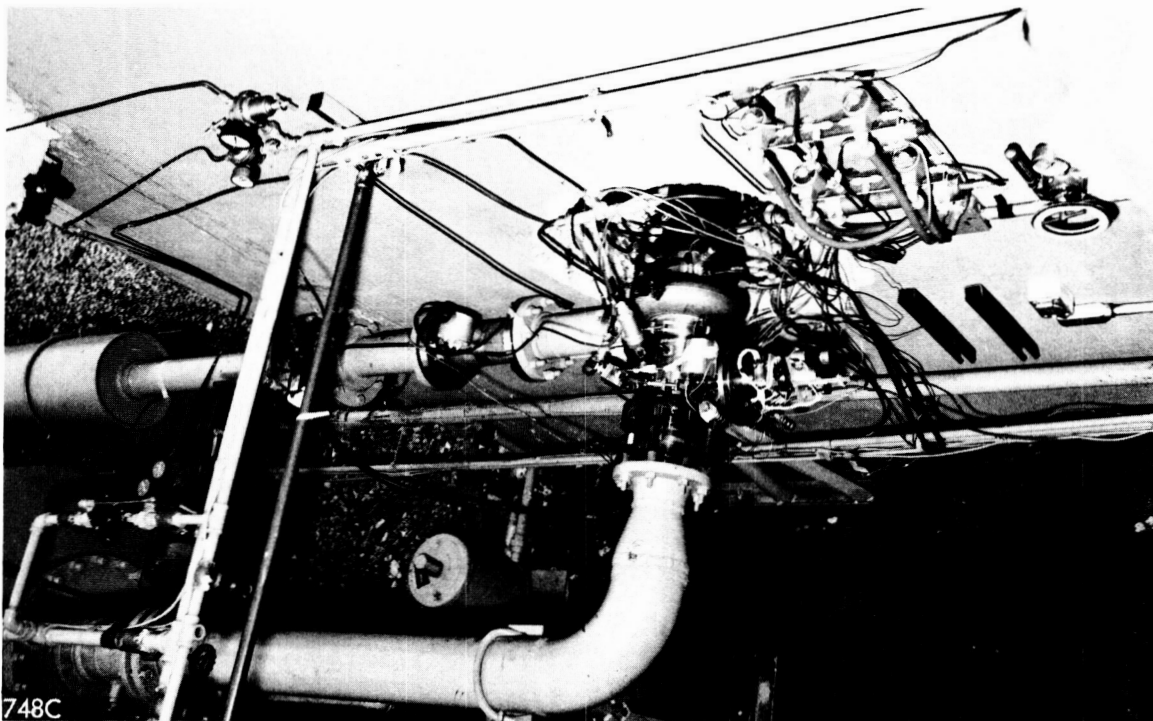
DYNAMOMETER INSTALLATION (BLDG. 43)

FIGURE 4.6.3-1



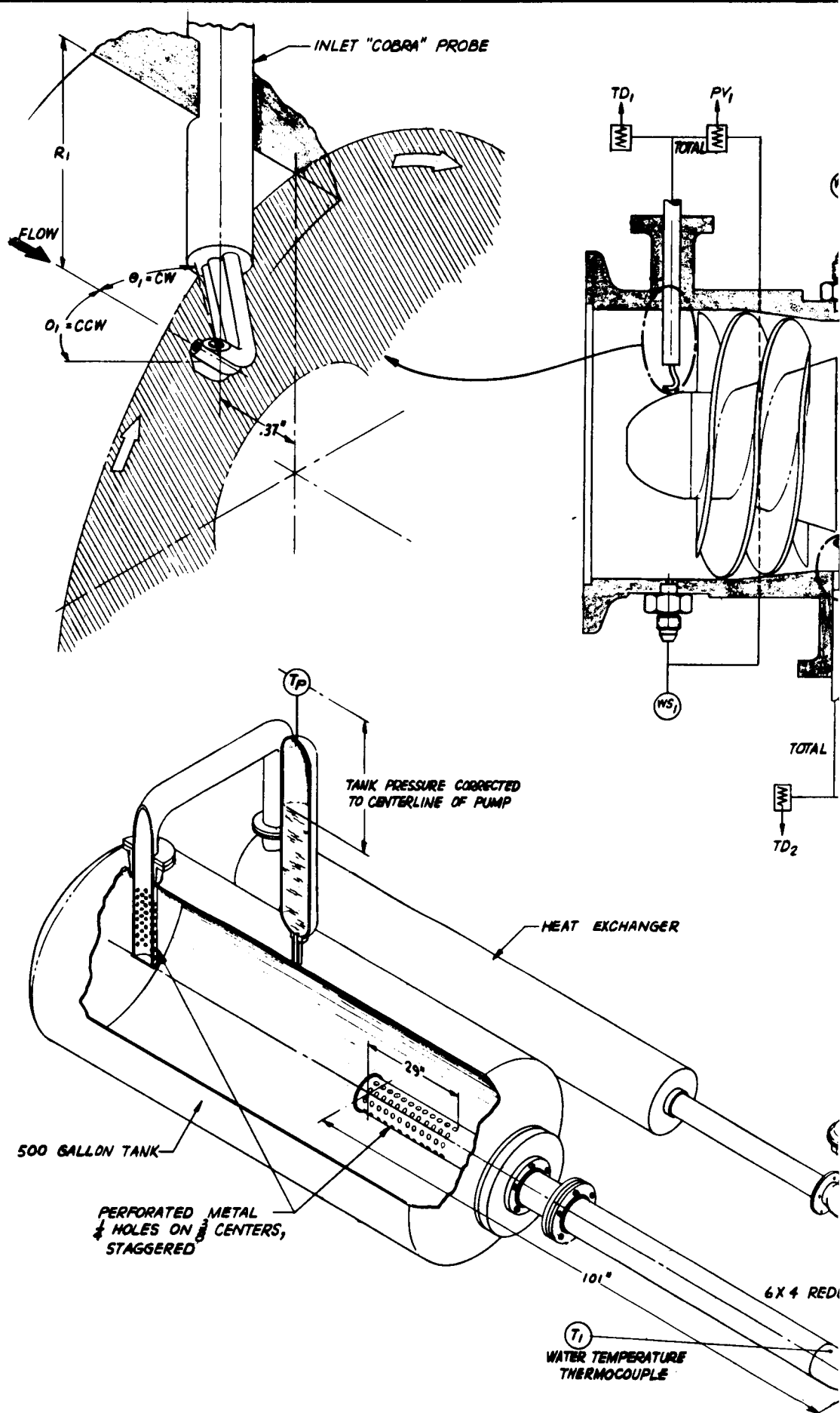
CONTROL ROOM (BLDG. 42)

FIGURE 4.6.3-2



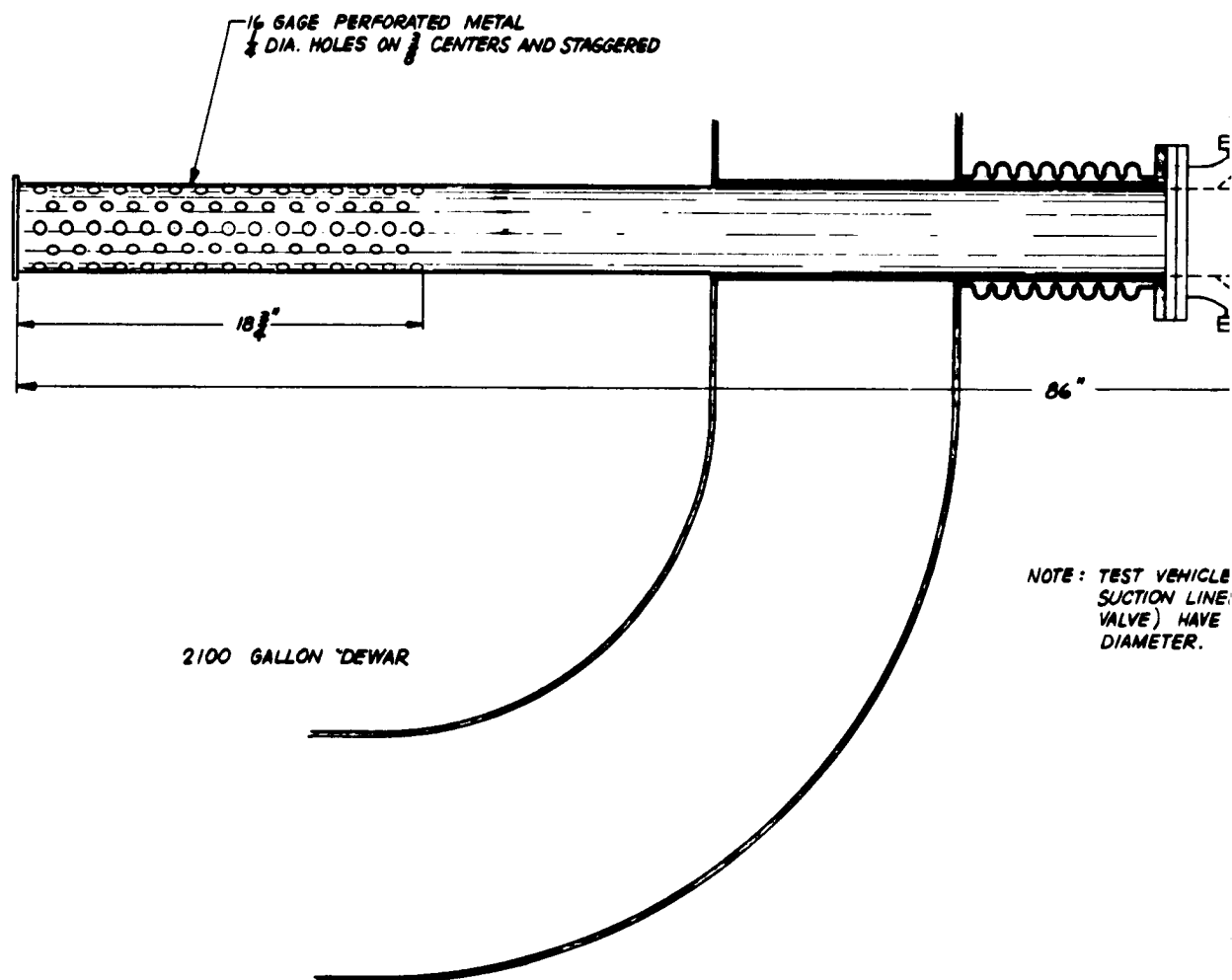
WATER LOOP SET-UP

FIGURE 4.6.3-4





CRYOGENIC TEST SET-UP SCHEMA



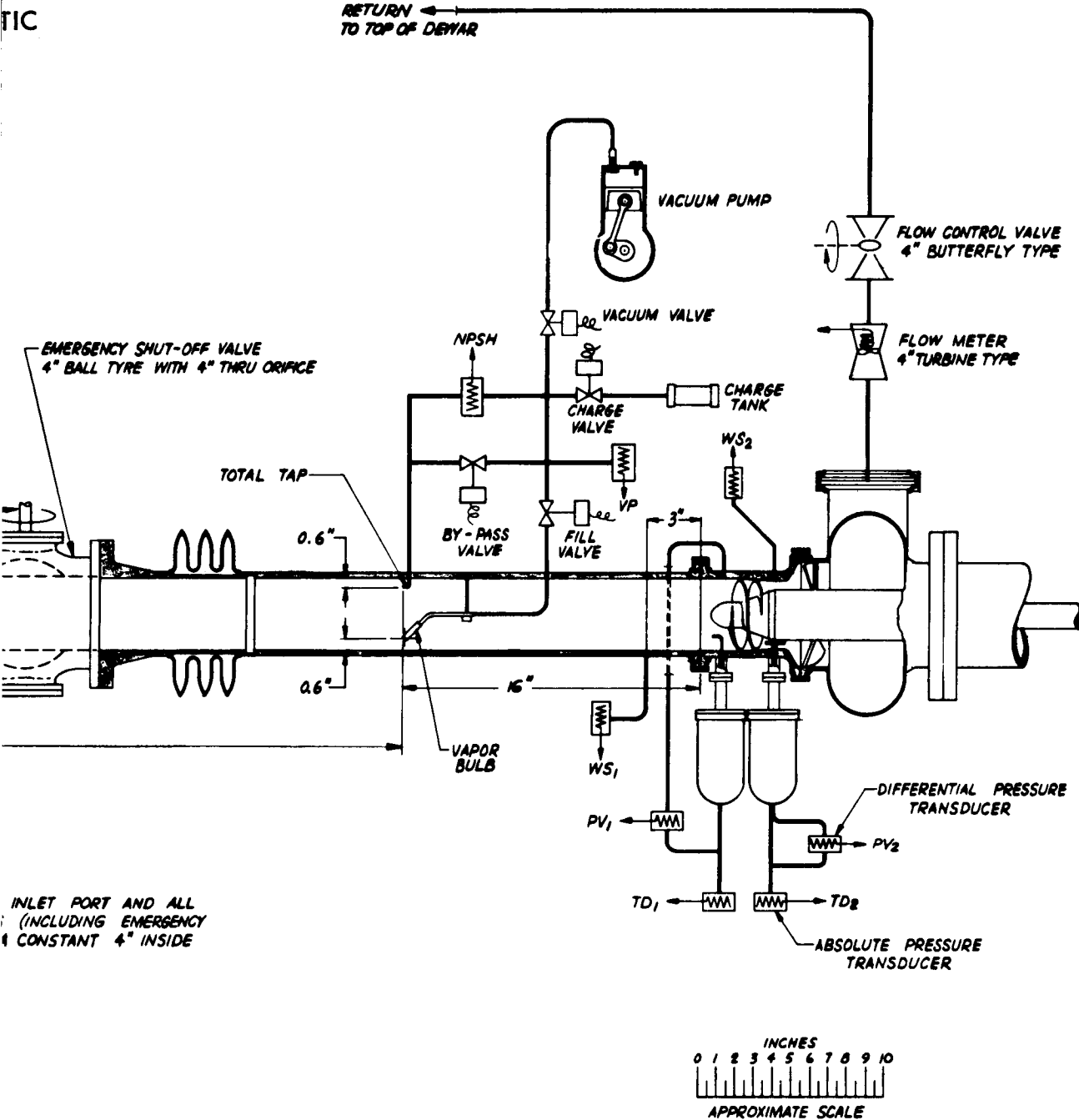
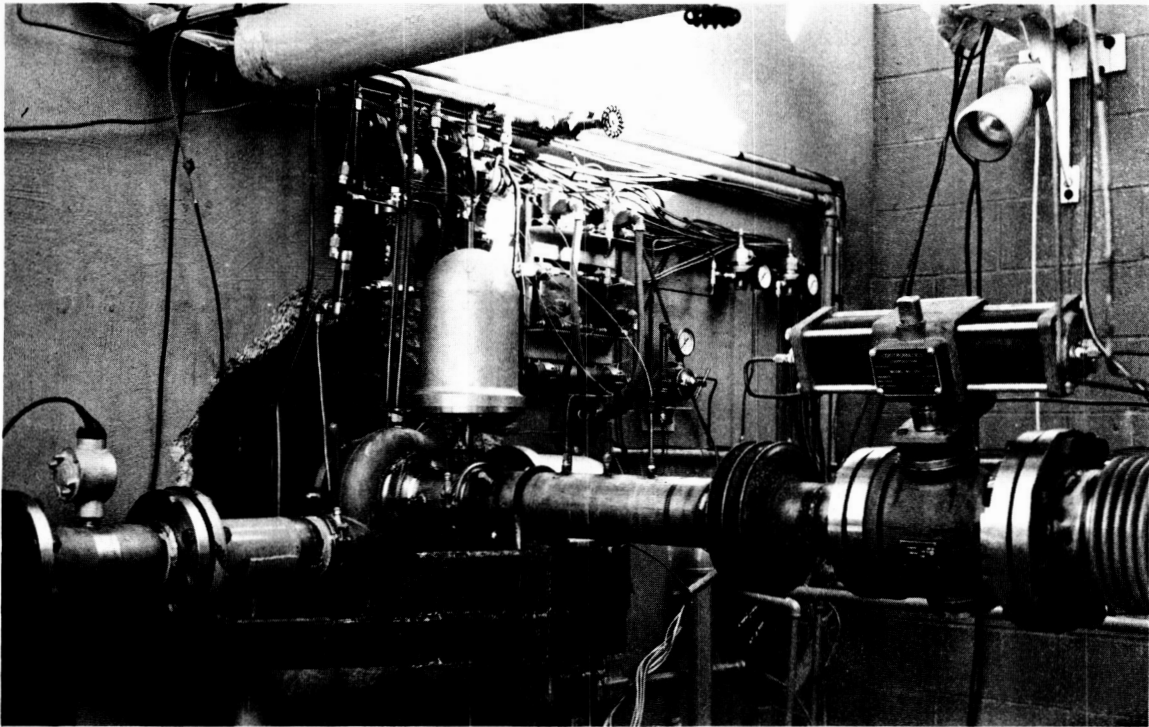


FIGURE 4.6.3-5



CRYOGENIC SET-UP

FIGURE 4.6.3-6



FACILITY

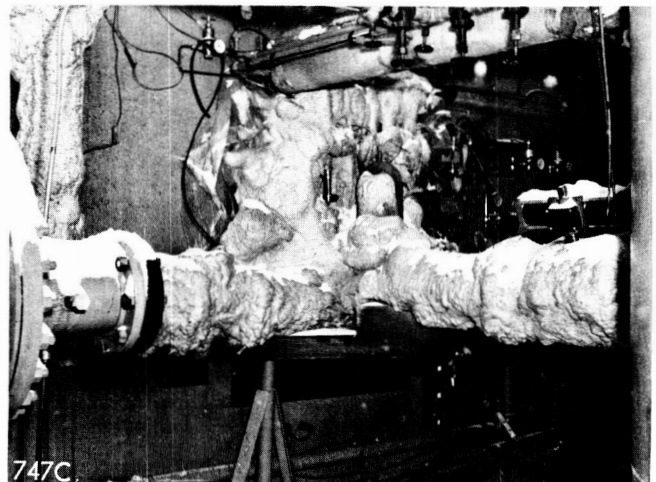


FIGURE 4.6.3-7 CRYOGENIC SET-UP WITH INSULATION

FIGURE 4.6.3-8



4.6.4 Test Instrumentation

To obtain the data required by the analysis phase of this program, it was necessary to survey both the inlet and discharge streams as close to the blade path as practical. To accomplish this survey, probes that could be traversed radially from hub to shroud were installed through the impeller housing and rotated in a tangential plane. Figure 4.6.3-3 shows orientation and general geometry of these probes plus a schematic of the transducer connections (data output only).

The total and static pressure taps at both inlet and discharge were connected to transducers, as shown in Figure 4.6.3-3. The output of these transducers and the probe position potentiometers were fed into a multi-point oscillograph. This oscillograph provided simultaneous data traces as follows:

θ_1	Inlet flow angle
R_1	Inlet radial position
TD_1	Inlet total pressure
PV_1	Inlet velocity pressure referenced to wall static
θ_2	Discharge flow angle
R_2	Discharge radial position
TD_2	Discharge total pressure
PV_2	Discharge velocity pressure referenced to probe static

(For information regarding orientation, refer to Figure 4.6.3-3).

4.6.4.1 Water Tests

In addition to oscillograph traces recording probe data, the following visual readings were taken from indicating panel instruments and recorded on data sheets:

CP	Casing pressure
TP	Tank pressure corrected to pump center line
T_1	Water temperature
WS_2	Discharge wall static pressure

Additional instrumentation was applied to the set-up for the purpose of monitoring the mechanical operation of the test vehicle. Flowmeters were included in the bearing and balance drum return lines. These indicated the unmetered flow that by-passed the four-inch meter. Only average readings from these auxiliary flowmeters are recorded in Table 4.6.5-1.

4.6.4.2 Cryogenic Tests

Figure 4.6.3-5 pictorially describes the application of instrumentation to the liquid hydrogen test set-up. The probe installation and orientation was identical to that

described for the water tests. The major difference in regard to instrumentation is the incorporation of a vapor bulb system that will sense, transmit, and record the NPSH and vapor pressure in the inlet line. In addition to the probe data previously described, the following traces were added to the oscillograph record:

NPSH Net positive suction head
VP Vapor pressure
WS₁ Inlet wall static pressure
WS₂ Discharge wall static pressure

During each run the following additional data readings were noted and transcribed on a tape recorder:

- a. Running time
- b. Flow
- c. Torque
- d. Speed
- e. Tank liquid level

The vapor bulb charging procedures as each item of the detail sequence was performed was also transcribed prior to each run. The playback was then rechecked for proper charging procedure before reducing the data.

4.6.4.3 Instrument Accuracy

Neglecting effects of detail instrumentation application (probe position, tap location, etc.), the overall accuracy of the oscillograph traces produced data points with an error less than plus or minus two percent of the value reported (See Table 4.6.5-1, 4.6.5-2, and 4.6.5-3). This was accomplished by calibrating each recording data channel as a complete system; i.e., the transducer, amplifier (or bridge balance), and galvanometer were statically calibrated together for both displacement and linearity. This was done not only before each test date but also before and after each run, so that dual calibration traces were available for comparison during data reduction.

The "hammer head" probe used in the discharge actuator (see Figure 4.6.3-3) was supplied and calibrated in a free air jet by NASA-LeRC. Figure 4.6.4-1 is the calibration curve supplied for this probe. The data reported in Tables 4.6.5-1, 4.6.5-2, and 4.6.5-3 do not have this correction applied; the velocity pressures noted (PV₂) are indicated values.

4.6.5 Test Procedure and Results

4.6.5.1 Water Run

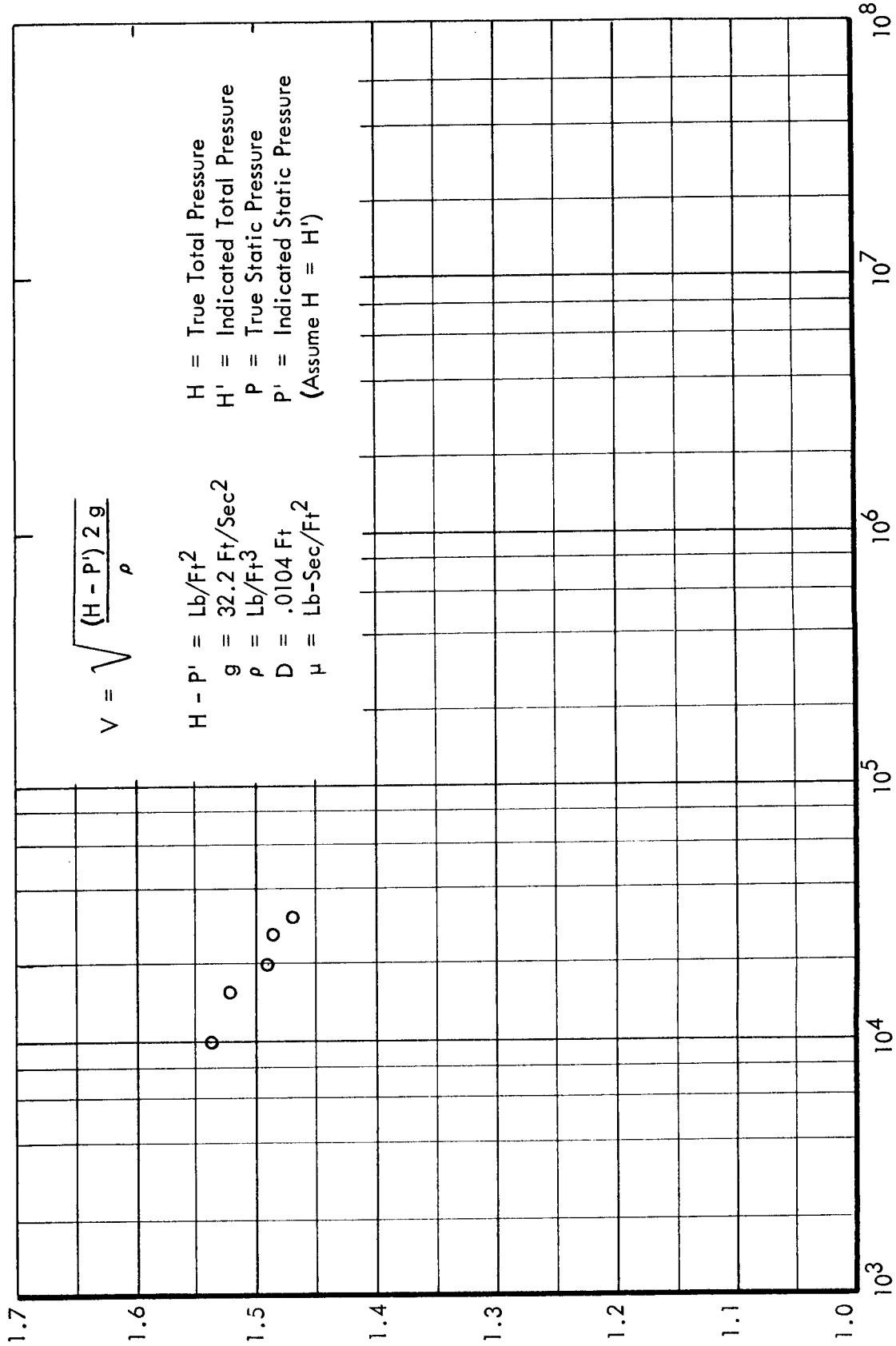
Prior to the actual run, an estimated performance map was established for non-cavitating conditions. From this curve, we selected the following operating points for inlet depression test runs:



TOTAL-STATIC ANGLE PROBE CALIBRATION

PROBE #9 AT NASA-LeRC ON 10-24-62

$$\frac{H' - P'}{H' - P}$$



<u>Speed</u>	<u>Flow</u>	<u>Flow Coefficient</u>
16,000 rpm	1050 gpm	0.1139
12,000	785	0.1139
8,000	525	0.1139
16,000	720	0.0785
12,000	540	0.0785
8,000	360	0.0785

After deaeration, the dome was pressurized with nitrogen to provide an inlet pressure above anticipated cavitation conditions and the pump brought up to the selected flow and speed. With the test vehicle operating at constant flow, speed, and tank pressure, an inlet and discharge survey was conducted while the following data were recorded on the log sheet:

- a. Actual speed and torque
- b. Inlet water temperature (T_1)
- c. Discharge static at shroud (WS_2)
- d. Casing pressure (CP)

When the probe surveys were completed and all data taken, the tank pressure was reduced and the previous procedure repeated. The tank pressure was reduced in increments until the minimum tank pressure noted on the data sheet (Table 4.6.5-1) was reached.

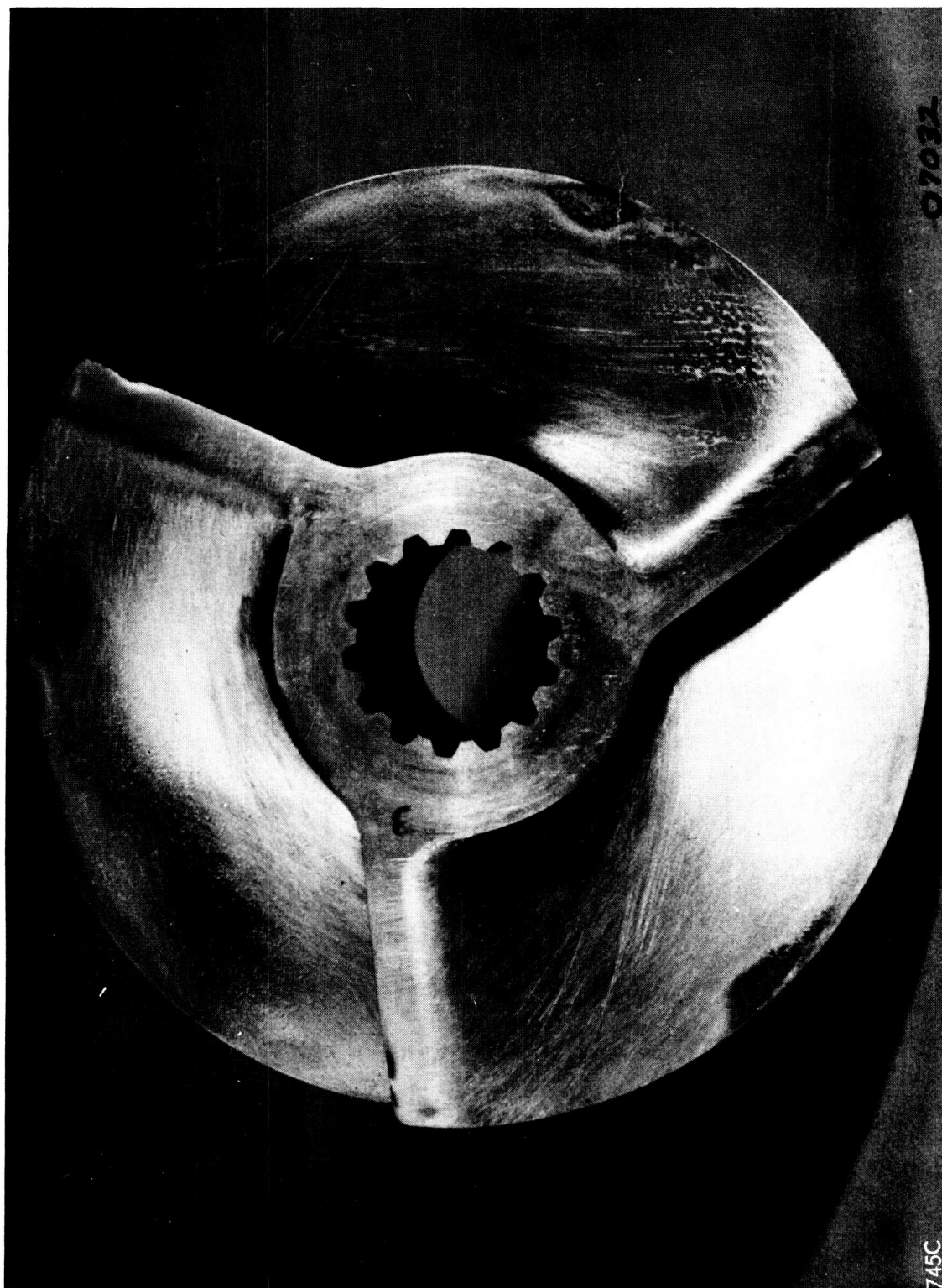
When the unit was first disassembled, the impeller blades were pitting on their suction surfaces toward the inlet. This pitting increased with additional running time until over one-half of the K-Monel blade thickness had been locally removed. Figure 4.6.5-1 shows a photo of the referee inducer after approximately ten hours total running time (see Section 4.7.3).

In addition to the pitting, the leading edges of all blades were noted to have been "nicked" in a uniform manner at the tips. These "nicks" do not have the eroded appearance normally associated with cavitation, but rather a "peened" or "battered" blunting of the edge. Since the inlet probe did not suffer mechanical damage, we are unable to ascertain the exact cause.

4.6.5.2 Cryogenic Runs

After the cryogenic loop was completed, the whole set-up was cooled down with liquid nitrogen. However, the rupture of a high pressure helium line precluded a trial run with nitrogen.

At this point, it was decided to delete the liquid nitrogen runs and proceed with a preliminary liquid hydrogen cool down and idle check-out of all equipment and instrumentation. Liquid hydrogen data were a mandatory requirement for correlation of analytical results.



IMPELLER PITTING AFTER TEN HOURS OF WATER OPERATION

Table 4.6.5-2 and 4.6.5-3 present all usable data obtained from four successful liquid hydrogen runs. They are summarized for reference below:

5 February	600 gpm at 20,000 rpm	3 mins-52 secs run time
25 February	1200 gpm at 20,000 rpm	4 mins-07 secs run time
26 February	1950 gpm at 30,000 rpm	3 mins-10 secs run time
26 February	1310 gpm at 20,000 rpm	18 mins-45 secs run time

The first run (5 February) was made with the panel flowmeter read-out improperly calibrated. However, the flow trace on the oscillograph was accurate and provided data for a low flow/high head performance point.

On 25 February, a trial run was conducted without tank pressurization. With the tank vented and a 3 foot head of liquid, the test vehicle was run up to 20,000 rpm and 600 gpm. After it was determined that the pump was operating stably, the flow was slowly increased to 1120 gpm.

Two runs were made on 26 February. The first was a complete inlet depression run, with probe survey data being obtained before the discharge probe actuator yaw motor failed. The following 30,000 rpm run was conducted with the discharge probe being manually traversed and the inlet probe "parked" at the RMS position (0.48 inch).

4.6.6 Test Program Conclusions and Recommendations

In general, the test equipment and vehicle performed satisfactorily. However, some difficulties were encountered that delayed or limited the overall test program. Discussion of these trouble areas was avoided during presentation of the test program material, but it is reported now for future reference:

- a. The output shaft of the cradled dynamometer gear box shifted off center due to high bearing clearance. This caused excessive wear on the coupling shaft and test vehicle drive spline. Another modified gear box is being obtained and all future couplings will incorporate O.D. fit spherical splines.
- b. The actuator driving the discharge probe required over 10 minutes to make an automatic survey and it was necessary to manually traverse the discharge and obtain angle data at four fixed radial positions. The slow speed was due to the low sensitivity of the control transducer and was caused by the small (.020) yaw taps in the "hammer head" probe. In the future, we propose to design a larger probe that incorporates yaw taps the size of the "cobra probe," since this traversed very well.



- c. The dual back to back face seals on the vehicle drive shaft were for the purpose of providing a helium gas barrier that would prevent hydrogen leakage into the dynamometer room. With one exception, it was impossible to maintain the helium pressure above the tank pressure since the seals blew open. Prior to any future use of this test vehicle, we will redesign the mounting flange and incorporate labyrinth type seals.



WATER DEPRESSION TEST

18 October 1962

Barometer @ 29.33" Hg

TABLE

	Radial Probe Position $R_1 =$							INLET PROBE						
								0.10			0.48			
	Tank Pressure TP psig	Water Temperature T_1 °F	Torque ft-lb	Power HP	Wall Static @ Discharge WS_2 psig	Static Rise (CP-TP) psi	Flow Coefficient ϕ	Angle θ_1 deg.	Total Pressure TD_1 psig	Velocity Pressure PV_1 psi	Angle θ_1 deg.	Total Pressure TD_1 psig	Velocity Pressure PV_1 psi	Angle θ_1 deg.
1050 gpm @ 16,000 rpm	90	55	34.4	105	169	80	0.1139	35.4	83.2	5.51	10.0	87.2	8.01	9.8
16,030	70	67	34.0	104	158	88		35.0	64.8	4.72	12.7	67.2	8.16	12.7
16,040	50	70	34.7	106	134	84		16.5	45.4	6.49	7.5	49.8	8.26	0.9
16,040	25	74	34.7	106	110	85		3.8	22.9	3.73	16.0	23.2	5.31	9.1
16,060	15	78	34.0	105	96	81		19.6	13.0	4.32	13.1	14.7	6.54	0.9
16,070	10	82	30.0	92	74	64		3.1	5.5	5.70	13.3	7.0	7.47	7.6
785 gpm @ 12,050 rpm	85	85	21.7	50.0	132	53		25.2	83.5	3.0	14.3	82.7	4.3	10.0
12,040	50	87	19.3	45.6	100	54		0.2	48.1	3.1	14.9	48.6	4.3	0.7*
12,050	20	89	19.3	45.6	69	52		21.9	16.9	2.9	15.2	17.9	4.3	9.8
12,060	5	90	19.3	45.6	53	51		17.4	4.4	1.6	10.5	4.5	3.1	12.0
12,060	2.2	90	19.0	43.7	47	48		35.7	-1.3	1.9	0.9	1.3	3.6	1.6
525 gpm @ 8,030 rpm	30	91	8.0	12.2	51	24		29.4	28.7	1.3	2.9*	30.4	1.9	5.8
8,010	10	90	8.0	12.2	30	22		17.8	8.0	1.7	2.2	8.0	2.4	9.8
8,010	2.2	90	7.3	11.1	20	20		35.7	-0.8	0.8	0.7*	0.5	1.9	12.5
720 gpm @ 16,100 rpm	70	89	51.2	157	248	174	0.0785	33.5	21.9	<-25.2	>43.0*	72.3	-0.6	2.9*
16,120	30	92	48.6	149	200	162		36.0	-5.0	<-25.2	>43.0*	26.2	-2.8	6.2*
16,110	10	94	46.5	143	152	138		>43.0*	16.2	6.0	43.0*	-3.7	-4.4	3.3*
16,140	2.2	94	36.3	112	105	100		24.1	0	3.4	24.1	0.5	4.6	14.3
540 gpm @ 12,080 rpm	40	90	28.4	65.5	140	108		38.0	13.7	<-25.2	>43.0*	43.6	1.9	>43.0*
12,060	10	90	28.0	64.3	102	90		38.0	-0.4	<-25.2	>43.0*	0.5	-1.7	>43.0*
12,060	2.2	90	25.7	59.1	85	80		>43.0*	3.7	2.2	>43.0*	-2.0	-2.1	10.7
360 gpm @ 8,000 rpm	20	89	12.0	18.3	62	42		36.1	6.2	-13.1	>43.0*	20.0	1.2	4.5
8,000	2.2	87	12.0	18.3	43	41		26.3	-5.2	-6.6	>43.0*	1.3	4.9	4.5

*Indicates CCW angular displacement of all others are CW from axial Q_L of shaft

< & > indicates galvanometer is off scale above or below value shown

4.6.5-1

					DISCHARGE PROBE													
0.80		1.17			R ₂ =	0.10			0.21			0.33			0.48			
Total Pressure TD ₁ psig	Velocity Pressure PV ₁ psi	Angle θ ₁ deg.	Total Pressure TD ₁ psig	Velocity Pressure PV ₁ psi		Angle θ ₂ deg.	Total Pressure TD ₂ psig	Velocity Pressure PV ₂ psi	Angle θ ₂ deg.	Total Pressure TD ₂ psig	Velocity Pressure PV ₂ psi	Angle θ ₂ deg.	Total Pressure TD ₂ psig	Velocity Pressure PV ₂ psi	Angle θ ₂ deg.	Total Pressure TD ₂ psig	Velocity Pressure PV ₂ psi	Un-Metered Flow gpm
87.7	8.41	6.7	87.2	8.51		44.4	223	44.7	48.6	214	40.3	57.2	205	36.0	55.3	200	38.0	10.0
68.0	8.51	6.9	68.5	7.67		42.3	202	44.2	50.8	185	41.9	56.6	176	36.2	54.6	169	38.9	
49.0	8.16	7.4	47.8	8.11		41.6	182	42.5	52.0	171	40.3	56.8	163	36.6	55.5	158	38.4	
23.9	6.24	9.3	23.7	6.05		41.9	156	44.4	52.7	147	39.6	55.9	137	36.1	53.7	134	38.5	
14.7	6.54	8.2	13.7	6.54		55.9	142	42.4	56.1	134	35.0	51.6	124	33.9	43.2	116	35.7	
7.2	7.38	9.6	7.2	7.38		48.2	126	32.8	55.2	110	36.9	59.0	100	31.2	57.3	95	33.8	7.7
83.0	4.4	10.9	83.2	4.7		37.6	167	25.2	39.2	160	21.3	53.1	155	20.6	51.6	155	22.0	9.2
48.6	4.3	4.2	49.8	4.3		41.3	127	21.5	50.5	126	23.6	49.5	120	20.6	51.6	118	22.0	
18.7	4.3	7.6	18.7	4.3		39.5	102	25.2	40.2	93.4	22.0	40.2	86.9	19.7	40.2	85.7	19.2	
4.5	3.1	0.2	4.5	3.1		40.8	81.1	24.0	50.1	76	22.4	52.9	70.8	20.1	40.2	82.4	20.1	
1.3	3.4	8.2	1.3	3.3		41.3	78.6	23.6	49.7	71.5	21.7	54.2	63.1	20.1	52.9	64.4	21.6	7.7
28.7	2.0	6.9	29.4	2.0		41.3	66.3	11.9	50.5	64.4	10.5	53.3	61.2	9.8	50.7	61.2	10.5	5.8
8.0	2.4	9.4	8.0	2.5		38.2	46.4	11.9	51.6	41.2	10.3	55.7	38.6	9.1	54.4	36.7	9.6	
0.5	2.2	2.5*	0.5	2.2		42.1	34.7	10.9	52.5	32.2	9.8	65.4	29.6	9.3	54.4	28.9	9.6	4.7
66.0	-8.7	6.0	68.5	-7.0		23.9	326	76.9	23.9	301	63.6	23.9	276	52.8	23.9	264	49.0	18.8
26.9	-5.5	2.7	29.9	-3.1		22.6	285	82.6	28.1	247	62.5	30.0	227	52.2	28.9	198	47.1	
6.2	1.6	3.3*	7.5	1.4		22.8	246	81.5	22.8	210	53.6	22.8	182	42.1	22.8	169	35.0	
0.8	4.6	12.0	0.5	4.6		28.5	-	48.7	30.6	-	30.7	42.3	-	21.3	42.3	-	21.3	12.1
38.6	-7.3	1.3	41.1	-1.6		23.3	191	44.6	28.5	174	36.6	29.4	160	31.6	25.7	152	28.1	12.1
0.3	-5.9	10.3	0.4	-2.1		23.1	156	46.0	28.3	135	34.3	30.8	120	29.3	28.7	113	26.5	
1.3	1.9	8.9*	1.5	2.1		23.3	138	46.9	27.4	116	32.9	31.7	102	28.1	32.8	92	19.9	12.1
18.7	-1.2	5.4	19.9	0.8		23.3	88.9	23.1	28.5	80.5	16.2	29.6	74.0	13.5	28.5	71.5	12.6	9.1
0	-1.6	7.8	0	-0.8		24.1	69.5	20.1	29.6	61.2	15.1	29.6	54.7	13.9	27.2	52.2	12.8	8.9

probe;

Leakage flow through bearings
 & balance chamber that by-
 passed flowmeter

or on stop



TABLE

LIQUID HYDROGEN DEPRESSION TEST

	Data Point	Running Time " : "	Vapor Pressure VP psia	Head Suction NPSH psi	Tank Level ft	Flow gpm	Speed rpm	Torque ft-lb	Power HP	Wall Static WS ₁ @ Inlet psig	Wall Static WS ₂ psi
5 February 1963 Barometer @ 29.58" Hg 680 gpm @ 20,000 rpm $\phi = 0.0519$ nominal	1	0-00	19.4	20.3	9.4	0	idle		tare	27.4	29.5
	2	0-58	20.0	7.4		470	20,390	9.00	35.6	15.4	40.0
	3	1-18	21.3	6.6		715				12.3	36.0
	4	1-39	21.2	4.4		635				11.1	36.0
	5	2-07	21.5	3.4		635				10.3	36.0
	6	2-26	22.2	1.1		578				11.3	36.0
	7	3-08	28.7	1.5		683				14.3	39.0
	8	3-25	29.2	1.6		675				14.6	39.0
	9	3-52	29.8	1.6		680	20,800	8.33	32.3	15.1	39.0
	10	4-17	30.3	1.8	9.2	0	idle		tare	14.4	17.0
25 February 1963 Barometer @ 29.21" Hg 1120 gpm @ 20,000 rpm $\phi = 0.1139$ nominal Tank vented Zero helium pressure	11	0-43	16.6	1.24	3.1	600	20,390	6.67	25.9	3.04	27.0
	12	1-15	17.0	0.27		600	20,390	6.67	25.9	2.64	25.0
	13	1-32	17.0	0.18						2.11	24.0
	14	1-59	17.0	0.09						1.91	23.0
	15	2-14	17.0	0.00		600	19,936	5.33	20.2	1.91	23.0
	16	2-32	16.5	0.00		680		4.67		1.32	21.0
	17	3-12	16.3	0.09		980	20,050	4.67	15.0	0.19	15.0
	18	3-36	16.1	0.18		1040	20,050	3.33	10.7	0.0	9.0
	19	4-07	15.9	0.27	2.4	1120	20,050	2.67	8.7	0.0	6.0
26 February 1963 Barometer @ 29.42" Hg 1950 gpm @ 30,000 rpm $\phi = 0.1139$ nominal	20	1-00	24.2	6.11	4.9	1874	30,550	13.7	79.7	12.1	35.0
	21	1-30	28.3	4.58		1917	30,550	12.0	69.7	14.6	38.0
	22	1-50	29.4	3.62		1895				14.8	39.0
	23	2-04	29.3	2.48		1874				13.9	37.0
	24	2-30	28.0	2.10		1917		12.7		13.0	34.0
	25	2-50	27.6	1.91		1921	30,770	11.0	64.4	13.0	32.0
	26	3-10	27.6	2.00	4.9	1908		11.0		12.9	31.0

E 4.6.5-2

	INLET PROBE				DISCHARGE PROBE				DIMENSIONLESS DATA						
g	Radial Position R_1 in.	Flow Angle θ_1 deg.	Total Pressure TD_1 psig	Velocity Pressure PV_1 psi	Radial Position R_2 in.	Flow Angle θ_2 deg.	Total Pressure TD_2 psig	Velocity Pressure PV_2 psi	Flow Coefficient ϕ	Cavitation Parameter \uparrow	Total Head Coefficient \downarrow	REMARKS			
2	0.47	\wedge 43° - Full CCW	31.9	All Negative	0.28	42.4	37.0	1.9	.0401	.1285	.3229	Dynamometer idling			
3	0.47		13.3		0.28	42.2	50.5	12.8				Note: Pannel flowmeter calibrated @ 60 ~ rather than 120 ~			
8	0.47		13.8		0.28		49.9	13.1							
0	0.47		13.3		0.28	28.8	47.5	13.8							
0	0.47		11.8		0.28	27.5	47.2	14.0							
7	0.47		10.7		0.28	25.4	47.9	14.2							
0	0.47		13.2		0.28	28.8	50.2	13.9	.0569	.0267	.3085	Probes @ rms (approx.)			
4	0.47		13.9		0.28	28.8	50.5	13.9				Dynamometer idling			
4	0.47		14.5		0.28	28.8	51.5	14.0							
3	0.47		18.0		0.28		22.7	1.4							
2	0.48	26.5	0.99	-0.13	0.27	33.7	31.7	9.6	.0512	.0215	.2665	Probes @ rms (approx.)			
8	0.48	42.0	1.11	-0.91	0.27	24.3	31.4	10.2							
3	0.48	42.0	0.62	-0.77	0.27	26.6	30.3	9.0							
9	0.48	42.0	0.62	-0.54	0.27	28.8	29.7	9.1							
8	0.48	42.0	0.49	-0.50	0.27	25.5	30.0	9.2					.0524	0	.2679
7	0.48	42.0	0.37	-0.13	0.27	28.8	26.9	9.2							
0	0.48	17.7	0.0	0.0	0.27	36.2	19.7	6.9					.0851	.0016	.1768
3	0.48	11.1	-0.12	-0.12	0.27	41.5	13.8	4.6					.0903	.0032	.1249
5	0.48	13.3	-0.13	-0.37	0.27	53.3	11.4	3.8	.0972	.0048	.1035				
	\uparrow All CCW														
5	0.48	9.9*	15.1	0.68	0.07	54.4	49.6	15.1	.1068	.0472	.1334				
8	0.48	6.2	17.7	0.68	0.27		51.6	15.3					.1092	.0354	.1311
4	0.48	4.4	18.5	0.91	0.47		48.6	14.4							
0	0.48	3.3	16.7	1.14	0.01		46.1	12.5							
5	0.48	2.2	15.7	0.95	0.27		41.7	12.1							
4	0.48	2.2	16.1	1.00	0.47		40.3	10.6	.1087	.0146	.0922				
5	0.48	2.2	16.2	1.14	0.0		43.7	12.4							
	\uparrow All CCW but (*) is CW				\uparrow Actuator angle drive failed Yaw angle constant										



TABL

LIQUID HYDROGEN DEPRESSION TEST

	Data Point	Running Time	Vapor Pressure VP psia	Suction Head NPSH psi	Tank Level ft	Flow gpm	Speed rpm	Torque ft-lb	Power HP	Wall Static @ Inlet WS ₁ psig	Wall Static @ Nicholas WS ₂ psig
26 February 1963 Barometer @ 29.42" Hg 1310 gpm @ 20,000 rpm $\phi = 0.1139$ nominal	27	1-15	29.9	6.87	6.85	1303	21,330	7.00	28.4	12.8	26.5
	28	2-30	26.1	5.25		1295	21,450	6.67	27.3	13.6	27.2
	29	3-30	26.7	4.67		1265	20,630	5.67	22.4	13.6	25.7
	30									13.5	25.9
	31									13.5	25.9
	32									13.6	25.0
	33									13.5	24.6
	34	5-00	27.6	3.15		1304	20,680	5.67	22.4	13.9	24.4
	35									13.9	24.4
	36									13.9	24.2
	37									13.9	24.2
	38									13.9	24.2
	39	8-00	28.8	2.38	6.60	1304	20,740	5.67	22.4	13.5	24.4
	40									13.6	24.4
	41									13.6	24.4
	42									13.6	24.4
	43									13.6	24.4
	44									13.5	24.3
	45	11-00	30.0	1.24	6.55	1310	20,800	5.00	18.8	13.7	24.4
	46	12-00	30.0	1.15			20,810	5.00	18.8	13.6	24.2
	47	13-00	30.2	0.95	6.30		20,830	5.00	18.8	13.5	24.4
	48	14-00	30.2	0.76			20,810	5.00	18.8	13.5	24.0
	49	15-00	30.3	0.57		1310	20,810	5.00	18.8	13.5	24.1
	50	16-00	30.4	0.48			20,830	5.00	18.8	13.5	24.1
	51	17-00	30.4	0.29	6.30	1340	20,830	5.00	18.8	13.5	23.9
	52	18-00	30.4	0.48		1400	20,860	5.00	18.8	13.4	21.1
	53	18-33	30.4	0.48		1430	20,850	4.33	17.5	13.4	21.1
	54	18-45	30.6	0.38	5.75	1420	20,850	4.33	17.5	13.4	20.9

E 4.6.5-3

INLET PROBE				DISCHARGE PROBE				DIMENSIONLESS DATA			REMARKS
Radial Position	Flow Angle	Total Pressure	Velocity Pressure	Radial Position	Flow Angle	Total Pressure	Velocity Pressure	Flow Coefficient	Cavitation Parameter	Total Head Coefficient	
R ₁ in.	θ ₁ deg.	TD ₁ psig	PV ₁ psi	R ₂ in.	θ ₂ deg.	TD ₂ psig	PV ₂ psi	φ	r	↓	
0.48	2.2	15.4	0.50	0.28	44.7	41.7	7.24	.1064	.1090	.2086	
0.48	4.4	16.1	0.50	0.28	43.7	41.7	7.13	.1051	.0824	.2008	
0.48	4.9	16.1	0.45	0.27	43.7	40.3	6.67	.1068	.0792	.2052	
0.59	4.4	16.1	0.45	0.27	44.1	41.0	6.67				
0.62	3.3	16.1	0.45	0.26	44.7	41.7	6.67				
0.62	2.2	16.1	0.45	0.26	44.7	40.4	6.78				
0.85	1.5	16.1	0.45	0.21	45.8	41.0	7.36				
0.48	8.2	16.1	0.50	0.21	49.4	40.4	7.10	.1098	.0531	.2050	
0.48	4.4	16.1	0.50	0.22	49.0	40.4	7.00				
0.48	4.4	16.2	0.50	0.23	48.8	40.4	7.00				
0.48	4.4	16.2	0.50	0.25	49.0	40.4	6.90				
0.48	3.3	16.1	0.50	0.27	49.6	39.0	6.60				
0.12	6.6	16.1	0.46	0.21	52.0	38.3	6.90	.1095	.0399	.1862	
0.39	6.0	16.1	0.46	0.27	51.6	38.3	6.67				
0.48	4.2	16.1	0.46	0.27	51.1	38.0	6.55				
0.72	2.4	16.2	0.46	0.30	51.3	38.0	6.30				
0.89	2.7	16.2	0.46	0.35	54.3	37.6	6.21				
1.17	0.1	16.2	0.54	0.48	55.4	38.3	6.30				
0.12	7.3	16.4	0.59	0.25	53.9	35.2	6.70	.1096	.0207	.1568	
0.48	7.3	16.3	0.45	0.27		35.2	5.30				
0.48	6.4	16.6	0.50	0.27		35.9	6.20				
0.48	6.4	16.4	0.50	0.27		36.6	6.20				
0.48	3.3	16.6	0.50	0.27		36.9	6.10	.1096	.0095	.1692	
0.48	6.4	16.4	0.55	0.27		37.3	6.20				
0.48	4.4	16.2	0.55	0.27		36.9	6.10	.1120	.0048	.1721	
0.48	4.4	16.3	0.69	0.27		34.5	6.10	.1168	.0080	.1509	
0.48	1.1	16.1	0.64	0.27		34.2	6.10	.1194	.0080	.1503	
0.48	3.1	16.3	0.69	0.27		34.2	6.00	.1186	.0063	.1486	

— All CCW

— Actuator angle drive
failed at this point

4.7 PRESENTATION AND DISCUSSION OF RESULTS

4.7.1 Introduction

The results of both experimental and analytical work on the referee inducer are summarized in Tables 4.7.1-1 and 4.7.1-2 respectively. Tests were run in water and hydrogen, and the actual test data are presented in Section 4.6. The analytical results are given for the calculated set of blade coordinates presented in Appendix C, using the quasi three-dimensional method of solution presented in Section 4.2. These results were calculated for incompressible flow of water, hydrogen, RP-1, and oxygen. Compressible flow results were obtained on only the leading portion of the inducer blading because the discontinuity of the blade curvature at the juncture of the helical and circular arc portions of the rotor (see Figure C-3) created difficulties in the two-phase iteration loop. Also, these compressible results of the analysis program do not include the lowest net positive suction heads obtained on test, due to imperfections in this same iteration loop. One-dimensional calculations of the state of the two-phase fluid at the inducer inlet, under the lowest NPSH (negative values) test conditions in hydrogen, are presented in Table 4.5.4-1 because of their importance and use in evolving design criteria. Correlations of the analytical and test results are possible, at least on a qualitative basis. However, such problems as probe calibrations for this application and questions about blade coordinates (Appendix C) preclude a completely quantitative evaluation of the quasi three-dimensional analysis program. Correlation of the theoretical one-dimensional methods of Section 4.5 with a "quality-at-inlet" hydrogen test run of Section 4.6 appears to be good.

4.7.2 Test Results

The first set of results in Table 4.7.1-1 are the ones for water, and they are presented in Figures 4.7.2-1 to 4.7.2-4. Figure 4.7.2-1 presents the wall static pressure rise across the inducer at various flow coefficients. No total pressure measurements were obtained as the probes were not yet operational at the time of these calibrations. These wall static pressure data are close to the mass-averaged static pressure only at high values of flow coefficient ϕ . Heavy loading of the blades near inlet causes high-pressure (rotating) back flows along the shroud upstream at low ϕ . This results in a lower reading of static pressure rise than is the average under such conditions.

Figure 4.7.2-2 summarizes the suction head depression runs in water. (Efficiency based on total pressure rise and shaft power input varied between 70 to 85% for water and hydrogen runs. Tables 4.6.5-1, 4.6.5-2, and 4.6.5-3 contain the necessary data for calculating these values, which were not plotted.) Two values of flow coefficient ϕ , 0.1139 and 0.0785, were held in these water tests, each at 8,000, 12,000, and 16,000 rpm. Values of the cavitation parameter $\mathcal{C} = \frac{p_1 - p_{sat}}{\frac{1}{2} \rho_f U_{1,t}^2}$ as low as 0.04 at $\phi = 0.1139$ and 0.34 at $\phi = 0.0785$

were obtained. (Note from equation (4.5.2-4) that $\mathcal{C} \approx K + \phi^2$, where the cavitation number R_e is defined by equation (4.5.2-3). Thus \mathcal{C} is here about 0.01 larger than K .) The Reynolds number, $Re = \frac{U_{1,t} r_{1,t}}{\nu}$, varied only from 2.6 to 5.1×10^6 ; so,



TABLE 4.7.1-1
TEST RESULTS

a. WATER RESULTS

Figure No.	Description	Speed - RPM	Flow Coefficient ϕ	Cavitation Parameter $\left[\frac{P_1 - P_{sat}}{\frac{1}{2} \rho_f U_{1,t}^2} \right]$	Reynolds Number $R_e = \left(\frac{U_{1,t} r_{1,t}}{\nu} \right)$
4.7.2-1	$\Delta \hat{p}_t$ vs ϕ	$\left\{ \begin{array}{c} 8,000 \\ \text{To} \\ 16,000 \end{array} \right\}$	0 to 0.14	(Non-Cavitating)	$\left\{ \begin{array}{c} 2.6 \times 10^6 \\ \text{To} \\ 5.1 \times 10^6 \end{array} \right\}$
4.7.2-2	ψ vs τ		0.1139, 0.0785	0.03 to 0.33	
4.7.2-3	$\hat{V}_z, \hat{V}_\theta, \hat{p}, \hat{p}$ vs \hat{r}_2 ↓	16,000	0.1139	0.1940	5.1×10^6
4.7.2-4		16,000	0.0403	↓	5.1×10^6
4.7.2-5		12,000	0.3295		3.8×10^6
4.7.2-6		12,000	0.0521		3.8×10^6
4.7.2-7		8,000	0.3404		2.6×10^6
4.7.2-8		8,000	0.1112	↓	2.6×10^6
4.7.2-9		16,000	0.0785	0.0785	5.1×10^6
4.7.2-10		16,000	0.0197	↓	5.1×10^6
4.7.2-11		12,000	0.1963		3.8×10^6
4.7.2-12		12,000	0.0409		3.8×10^6
4.7.2-13		8,000	0.2607		2.6×10^6
4.7.2-14		8,000	0.1173	↓	2.6×10^6

b. HYDROGEN TESTS

4.7.2-15	χ vs τ	$\left\{ \begin{array}{c} 20,000 \\ 30,000 \end{array} \right\}$	0.11	0 to 0.11	2.9 to 4.3×10^7
4.7.2-16	$\hat{V}_z, \hat{V}_\theta, \hat{p}, \hat{p}$ vs \hat{r}_2		0.110	0.0531	2.9×10^7
4.7.2-17	↓	20,000	0.109	0.0399	2.9×10^7

WALL STATIC PRESSURE COEFFICIENT
VS. FLOW COEFFICIENT (NON-CAVITATING)

WATER

REYNOLDS NO. - R_e

- — ○ 5.1×10^6 (16,000 rpm)
- — □ 3.8×10^6 (12,000 rpm)
- △ — △ 2.6×10^6 (8,000 rpm)

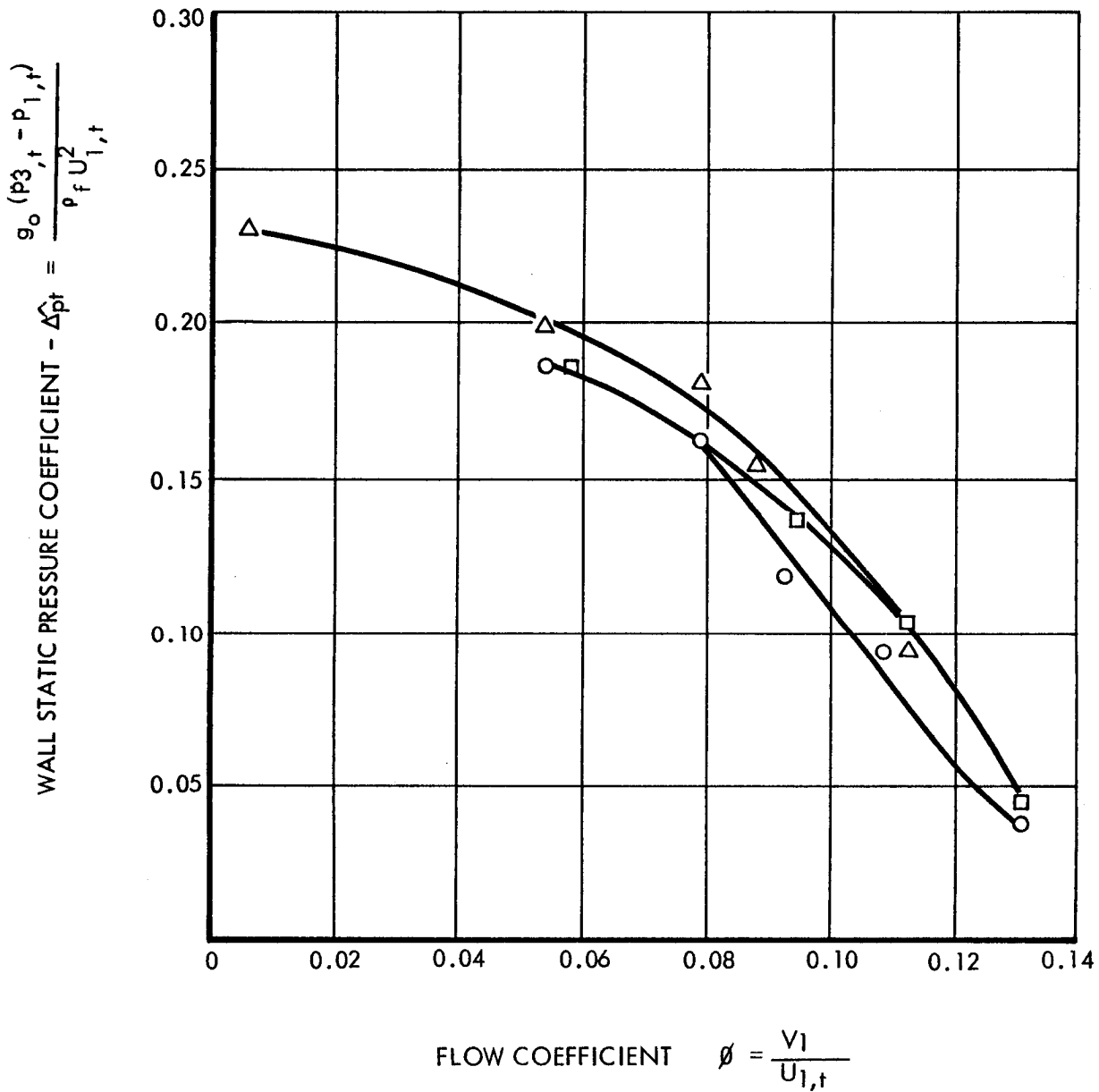


FIGURE 4.7.2-1

TOTAL HEAD COEFFICIENT VS. CAVITATION PARAMETER IN WATER

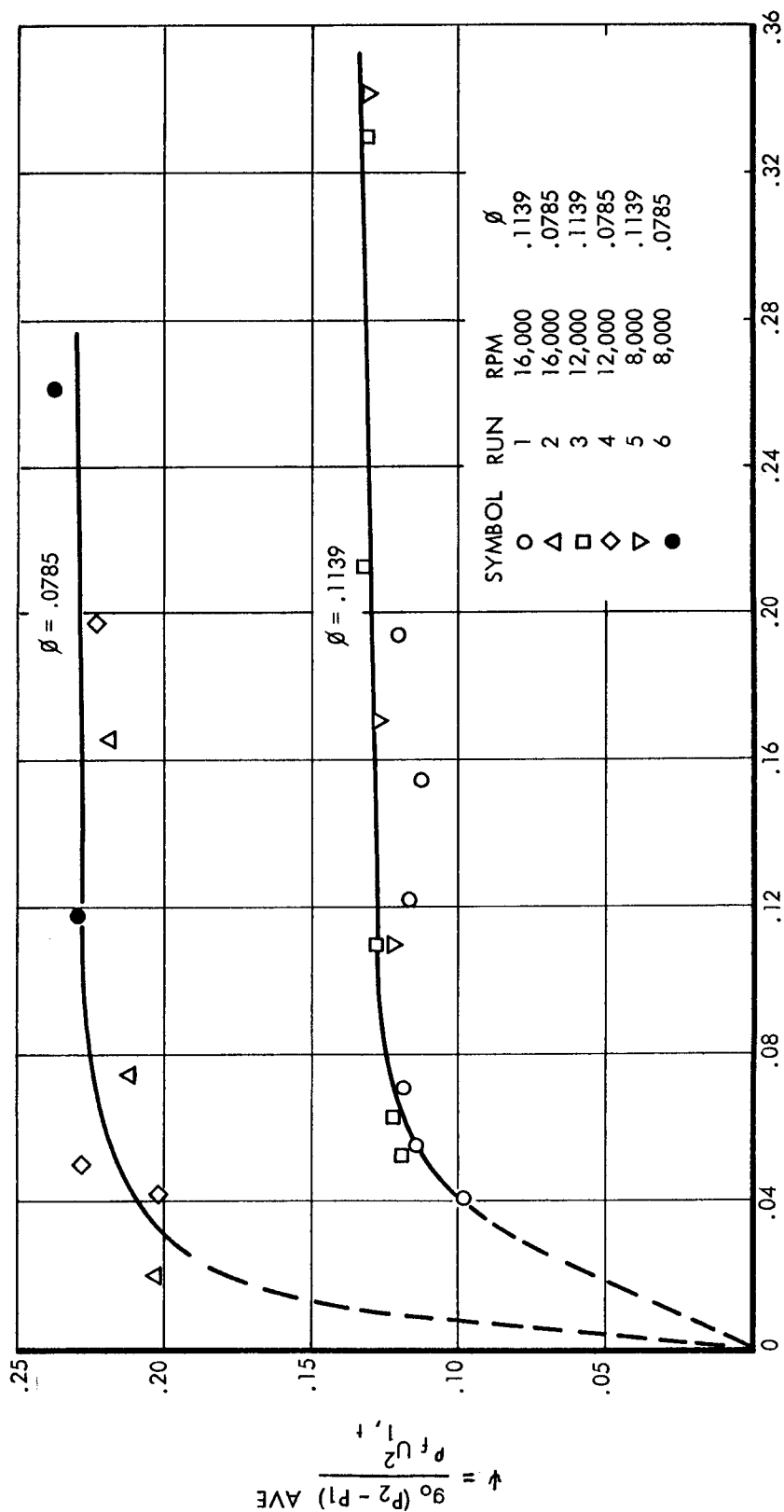


FIGURE 4.7.2-2

differences at $\phi = 0.1139$ in total head coefficient ψ (cf. Figure 4.7.2-2), can be explained by normal scatter of the data for the incompressible case ($\tau > 0.25$). Effects of the thermodynamic parameter Θ (cf. Section 4.7), which applies in the case of two-phase fluid motion, may account for differences in ψ at low τ . Table 4.4.4-1 shows that hydrogen, for example, has a very low value of \mathcal{T} (and therefore of Θ). It is known that hydrogen gives high ψ at very low τ . Now the increase only of speed in the same fluid (not of ϕ) gives higher Θ , which would thereby result in a slightly smaller ψ . Thus we might expect that the R_e and Θ effects on ψ should cancel each other, since ψ would be expected to increase with R_e .

Although surveys of velocity, total pressure, and static pressure were made at both inlet and outlet, at inlet only the total pressures were used in the presentation of Figures 4.7.2-2 to 4.7.2-14. For Figure 4.7.2-2, P_2 and P_1 are the probe readings at $r_2 = 0.7945$. Figures 4.7.2-3 to 4.7.2-14 show the distributions of the axial and tangential absolute velocity ratio components, $V_{z,2}/U_{1,t}$ and $V_{\theta,2}/U_{1,t}$, and static and total pressure coefficients, $\frac{P_2 - P_1}{\rho_f U_{1,t}^2}$ and $\frac{P_2 - P_1}{\rho_f U_{1,t}^2}$, versus radius ratio $r_2 = \frac{r_2}{r_{1,t}}$ for these

suction runs. These values have been corrected to the trailing edge by the assumption of constant angular momentum, $r_2 V_{\theta,2} = r_3 V_{\theta,3}$, constant ratio of $V_{z,3}/V_{z,2}$ from hub to shroud, and constant pressure, $P_2 = P_3$. Two figures are shown for each speed; one for essentially non-cavitating conditions (high τ), and the other for cavitating conditions (low τ).

No need for a calibration correction for these water tests was found in the velocities obtained by the probes at outlet. This was verified by numerical integration of the elemental volume flows at outlet to obtain the total volume flow. This agreed, within the accuracy of the calculations, with the value measured by the flow meter in the loop. The reason for this may be due to the probes being located in a rather restricted internal flow passage, as compared to the configuration used in the NASA-LeRC calibration which called for the correction of readings (see Figure 4.6.4-1).

Data similar to the types presented above are shown for hydrogen in Figures 4.7.2-15, 4.7.2-16, and 4.7.2-17. Figure 4.7.2-15 summarizes the suction depression results that were obtainable in the vicinity of $\phi = 0.11$. (Other data were obtained for widely scattered values of ϕ and may be seen in the data of Tables 4.6.5-2 and 4.6.5-3.) The 30,000 rpm data are shown to have considerably lower ψ than that of all the rest, which was obtained at 20,000 rpm. This could be ascribed to the effect of the thermodynamic parameter Θ discussed above, especially since the τ values indicate a rather predominant two-phase activity. The very high values of ψ for this ϕ (see Figures 4.7.2-2 and 4.7.2-15) - as compared to the water results - need further explanation. Figures 4.7.2-16 and 4.7.2-17 show the results of the surveys at outlet that were obtainable. The trends are somewhat similar to those of water at the same τ (cf. Figure 4.7.2-4, especially in the tangential velocity V_{θ}). Here the velocities obtained from the probe data had to be multiplied by 0.75 in order for the integrated volume flow across the exit to be equal to that measured on the downstream flow meter. This is equivalent to using a value of 1.8 for the correction factor $\frac{H' - P'}{H' - P}$ in Figure 4.6.4-1.



MEASURED VELOCITY AND PR

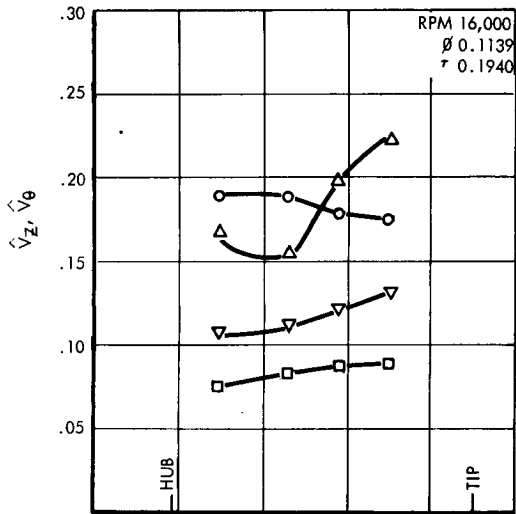


FIGURE 4.7.2-3

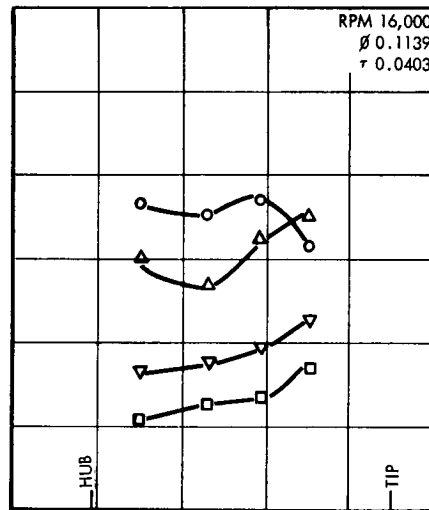


FIGURE 4.7.2-4

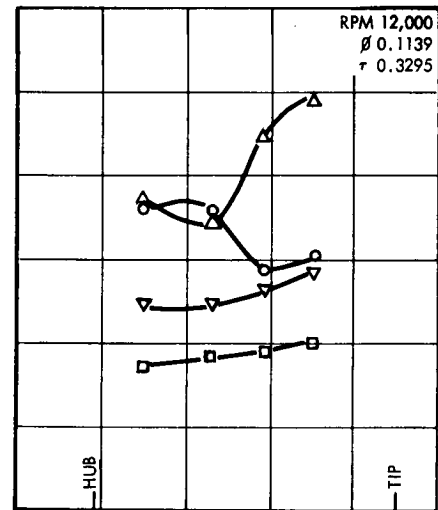


FIGURE 4.7.2-5

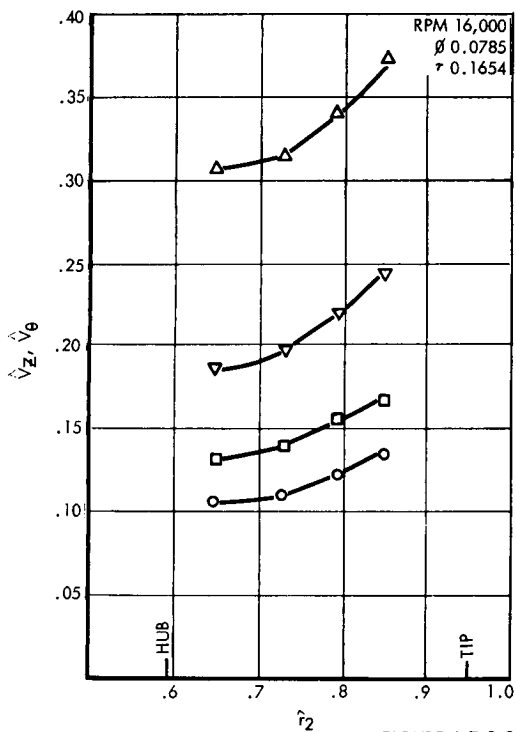


FIGURE 4.7.2-9

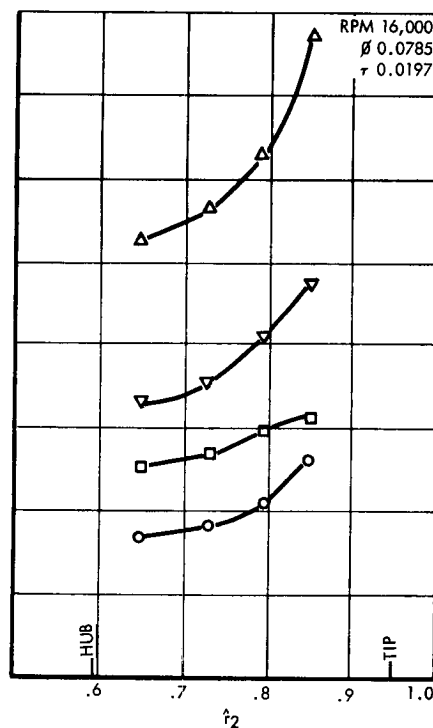


FIGURE 4.7.2-10

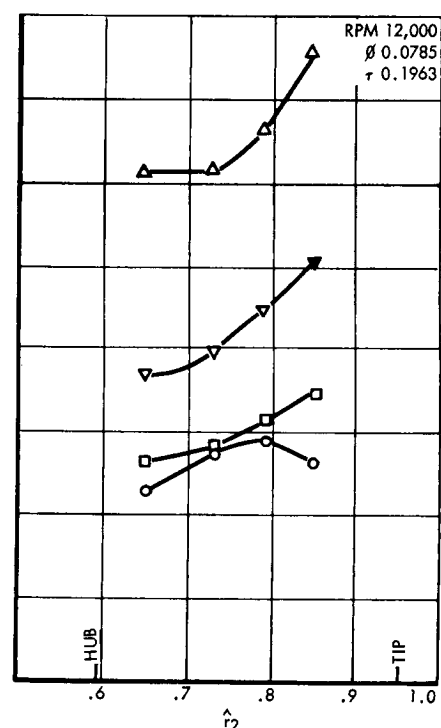


FIGURE 4.7.2-11

$$\hat{V}_Z = \frac{V_Z}{U_{1,t}} : \circ$$

$$\hat{V}_\theta = \frac{V_\theta}{U_{1,t}} : \Delta$$

$$\hat{p} = \frac{g_o (p - p_1)}{\rho_f U_{1,t}^2} : \square$$

$$\hat{p} = \frac{g_o (P - P_1)}{\rho_f U_{1,t}^2} : \nabla$$

PRESSURE DISTRIBUTIONS VS RADIUS

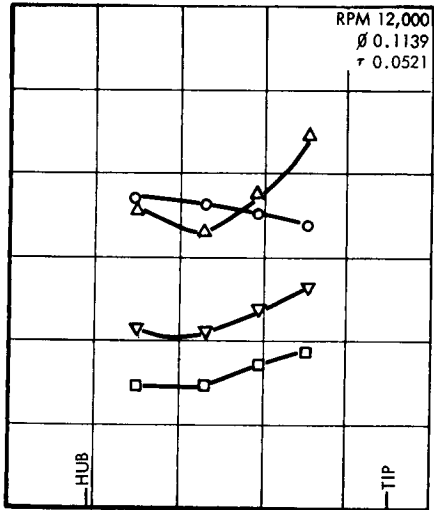


FIGURE 4.7.2-6

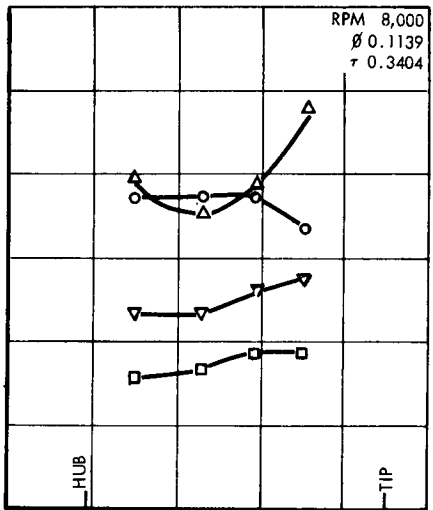


FIGURE 4.7.2-7

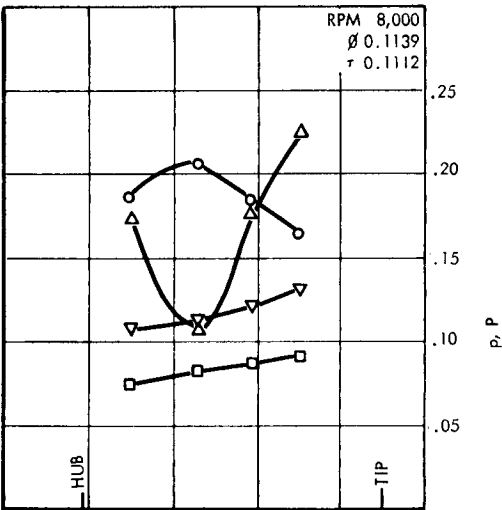


FIGURE 4.7.2-8

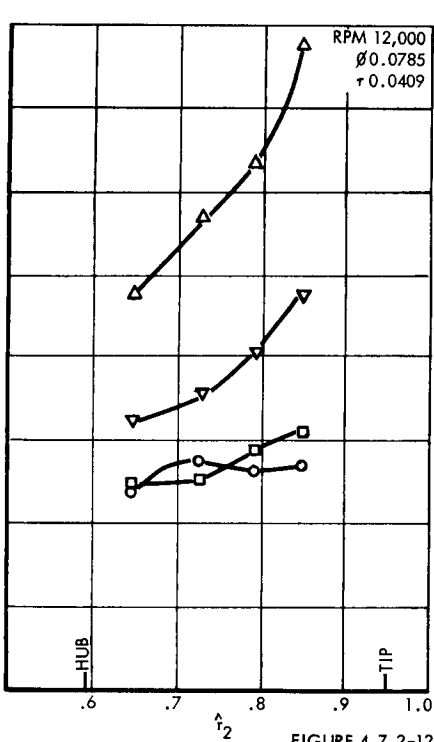


FIGURE 4.7.2-12

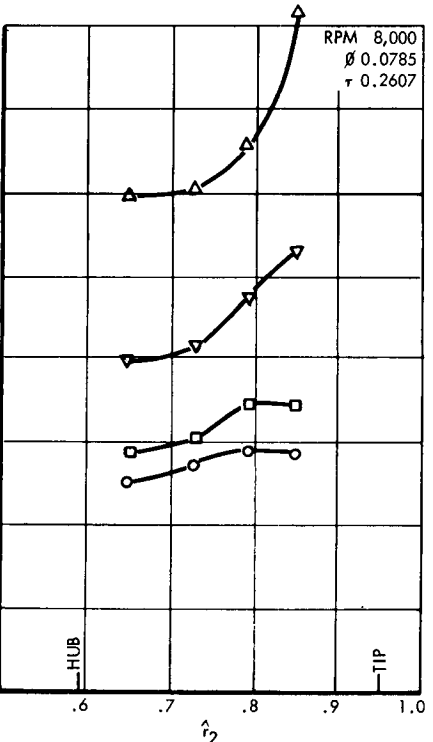


FIGURE 4.7.2-13

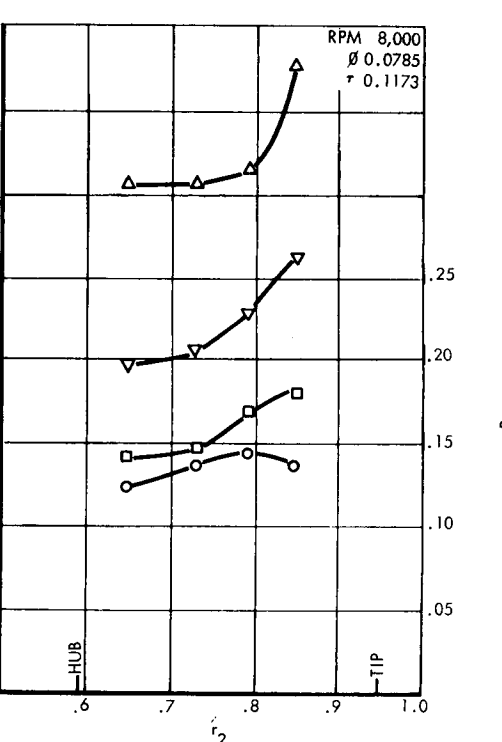


FIGURE 4.7.2-14

TOTAL HEAD COEFFICIENT VS. CAVITATION PARAMETER,
IN HYDROGEN

Flow Coefficient ≈ 0.11

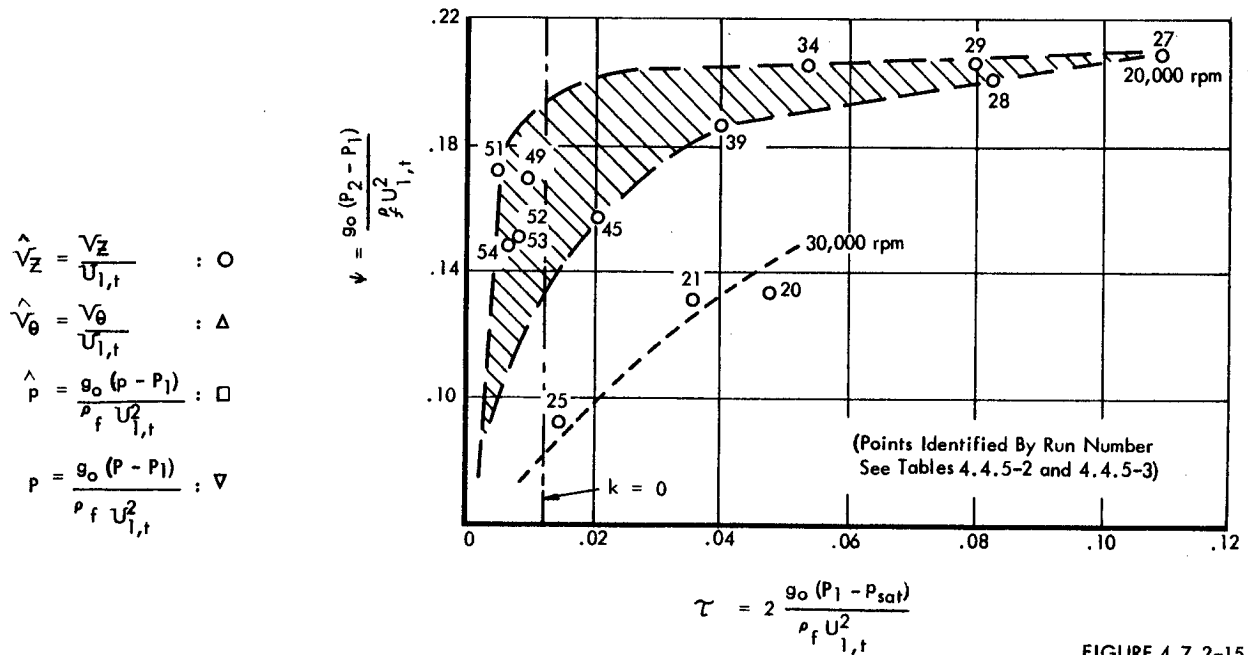


FIGURE 4.7.2-15

MEASURED VELOCITY AND PRESSURE DISTRIBUTION VS RADIUS

MEASURED VELOCITY AND PRESSURE DISTRIBUTIONS VS RADIUS

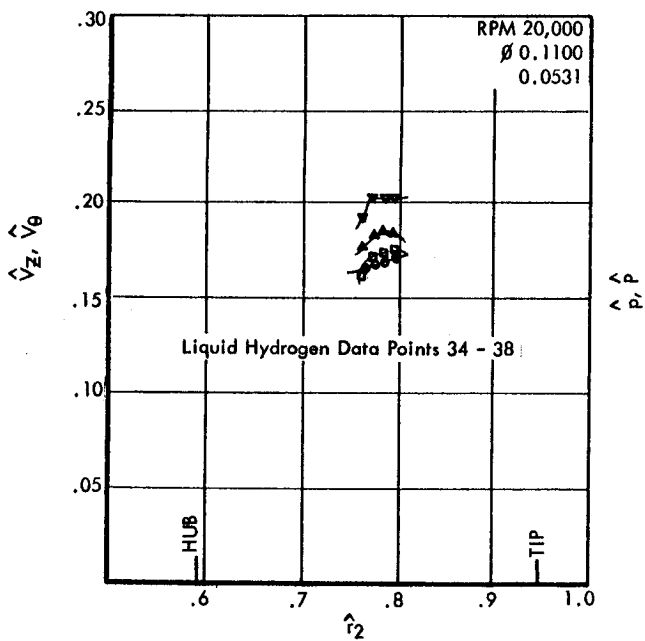


FIGURE 4.7.2-16

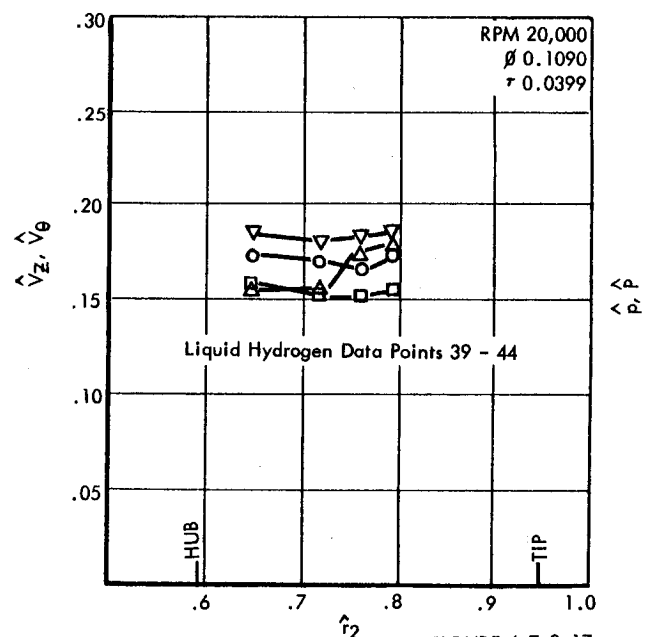


FIGURE 4.7.2-17



Also, the Reynolds number of Figure 4.6.4-1 in the hydrogen tests was about 5×10^5 , which is beyond the range of the calibration. Even so, the need for such a large correction, compared to none for water, needs further explanation.

The most revealing hydrogen test was run with boiling liquid in the tank, which was vented to the atmosphere (cf. Data points 11 to 19 in Table 4.6.5-2). Here the flow coefficients, based on the outlet liquid volume flow, were lower than the chosen value of 0.1139 which is estimated to be near the optimum for the inducer tested. However, the inlet volume flow coefficient to the inducer for Data point #19 has been calculated, in Table 4.5.4-1, to be up to this value (cf. Table 4.6.5-2 also), and τ was -0.0014. Here it is important to note that p_{sat} in the τ definition is the value of pressure at the start of vaporization (cf. Sections 4.1 and 4.4). Thus we may state that K was -0.013 for this point (see equation 4.5.2-4). Although γ was low (0.10), it is comparable to that of Data point #25 at 30,000 rpm, shown on Figure 4.7.2-15 for $\phi = 0.11$ and for a considerably higher τ of +0.015.

4.7.3 Results of Theoretical Calculations

The results of the analytical work are conveniently divided into incompressible and compressible studies, as seen in Table 4.7.3-1. All calculations were made for a flow co-efficient, $\phi = 0.1139$. The quasi three-dimensional analysis of Section 4.2 was applied successfully to the complete inducer for incompressible operation in water, hydrogen, RP-1, and oxygen. As can be seen from equations (4.4.2-2) and (4.4.2-4), at constant ϕ only R_e has any influence on the results if τ is high enough to prevent vaporization (compressibility) and the attendant Θ effects. The range of R_e was from 1.2×10^6 (RP-1 at 60°F and 16,000 rpm) to 4.3×10^7 (hydrogen at 20°K and 30,000 rpm). Figure 4.7.3-1 shows the Reynolds number effect on efficiency as calculated by the analysis program. (The losses were obtained according to the methods of Sections 4.1 and 4.2. The values of the equivalent diffuser angle that were used in these calculations were only 79% of the correct value given in equation (4.1.3-9). The effect of this error was checked and found to change the answers by less than 1/2%, which is within the accuracy of the calculations.) Other effects are seen on the total pressures, etc., if one examines the outlet velocity and pressure distributions of Figures 4.7.3-6 to 4.7.3-14. Figure 4.7.3-6 shows the results for zero loss, and Figures 4.7.3-10, 4.7.3-11, 4.7.3-12, and 4.7.3-14 for the high R_e cases of hydrogen and oxygen show similar results. The most dramatic effect is seen in the change of the V_e distribution from Figure 4.7.3-6 (no loss) to Figure 4.7.3-13 (RP-1 and the lowest R_e). These outlet distributions show the same trends and approximate relation to each other as do those of the comparable test results. Quantitative differences could be explained by the limitations imposed on the analysis because of the assumption of a primarily axial flow; because of the inability of a quasi three-dimensional method to describe the blade unloading phenomenon; and because of differences in blade co-ordinates used in the calculations from those of the rotor itself (see Appendix C). (Six annuli were used for these calculations.)

TABLE 4.7.3-1
RESULTS OF THEORETICAL CALCULATIONS
($\phi = 0.1139$ THROUGHOUT)

a. INCOMPRESSIBLE STUDIES

Figure No.	Description	Speed - Rpm	Fluid	Cavitation Parameter τ	Reynolds Number $Re (= \frac{U_{it} r_{it}}{\nu})$
4.7.3-1	η vs Re			(Sufficient to Prevent All Vaporization)	$10^6 \times 10^8$
4.7.3-2	p vs z	16,000	Water		5.1×10^6
4.7.3-3	w vs z	16,000	Water		5.1×10^6
4.7.3-4	p vs z		(No Loss)		
4.7.3-5	w vs z		(No Loss)		
4.7.3-6	$\hat{v}_z, \hat{v}_\theta, \hat{p}, \hat{p}$ vs \hat{r}_2		(No Loss)		
4.7.3-7		16,000	Water		5.1×10^6
4.7.3-8		12,000	↓		3.8×10^6
4.7.3-9		8,000	↓		2.6×10^6
4.7.3-10		16,000	Hydrogen		2.3×10^7
4.7.3-11		20,000	↓		2.9×10^7
4.7.3-12		30,000	↓		4.3×10^7
4.7.3-13		16,000	RP-1		1.2×10^6
4.7.3-14		16,000	Oxygen		2.6×10^7

b. COMPRESSIBLE STUDIES (ON INITIAL 8.35% OF INDUCER AXIAL LENGTH z .)

4.7.3-15	ψ vs τ	16,000	Water	$z \geq 0.08$	5.1×10^6
4.7.3-16	η vs τ	↓	↓	↓	↓
4.7.3-17	p vs z				
4.6.3-18	w vs z			↓	
4.7.3-19	$\hat{v}_z, \hat{v}_\theta, \hat{p}, \hat{p}$ vs \hat{r}_2			$z \geq 0.266$	
4.7.3-20	↓	↓	↓	0.203	↓
4.7.3-21				0.160	
4.7.3-22				0.120	
4.6.3-23				0.080	

EFFICIENCY VS. REYNOLDS NUMBER,
FOR THEORETICAL, INCOMPRESSIBLE FLOW

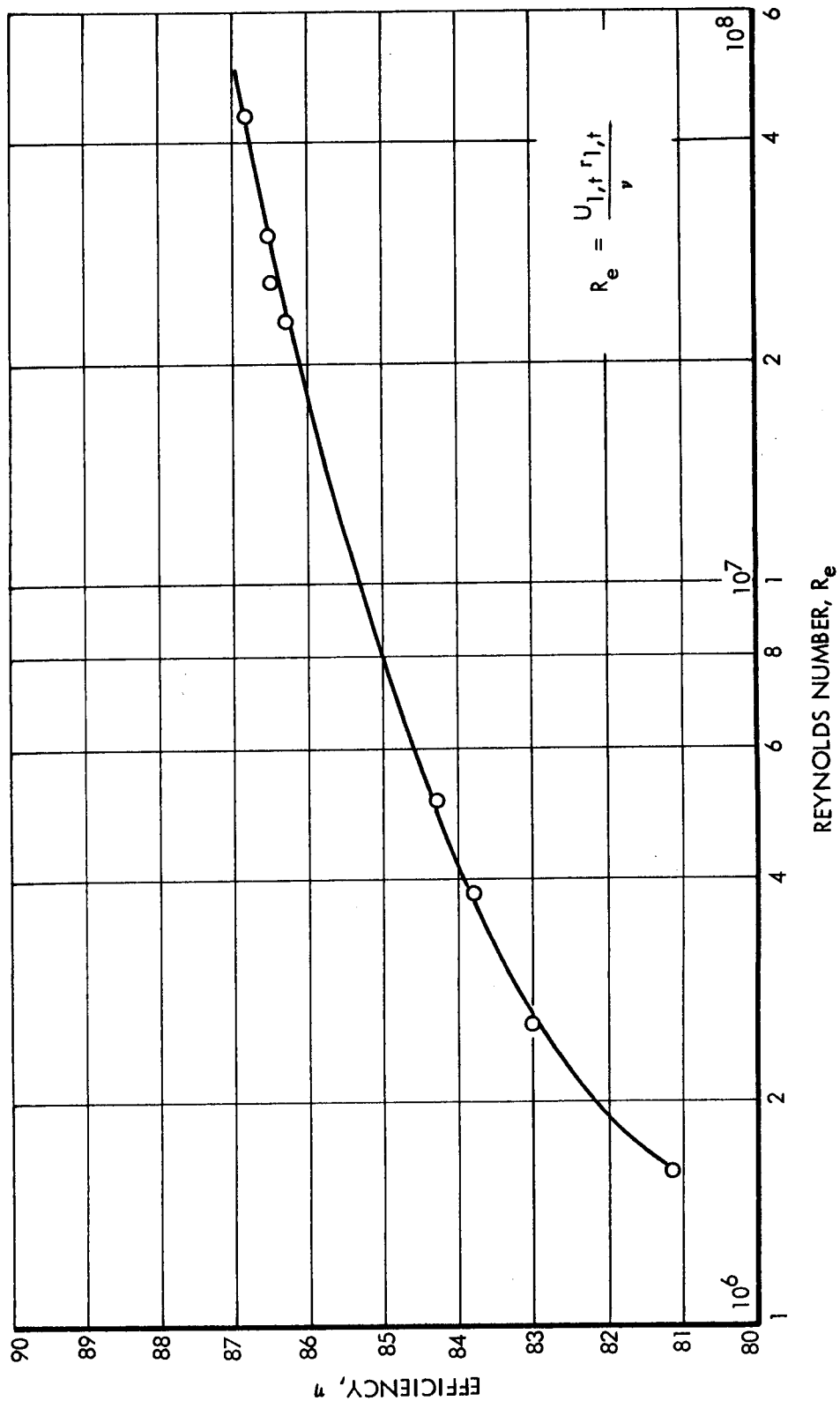
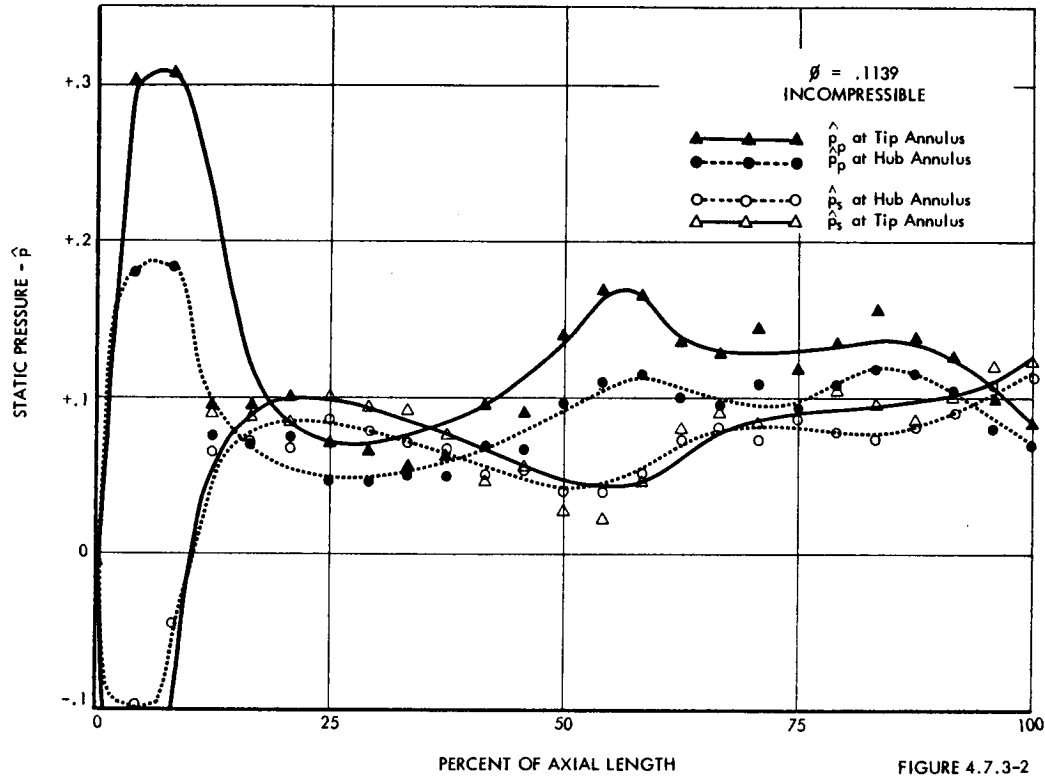
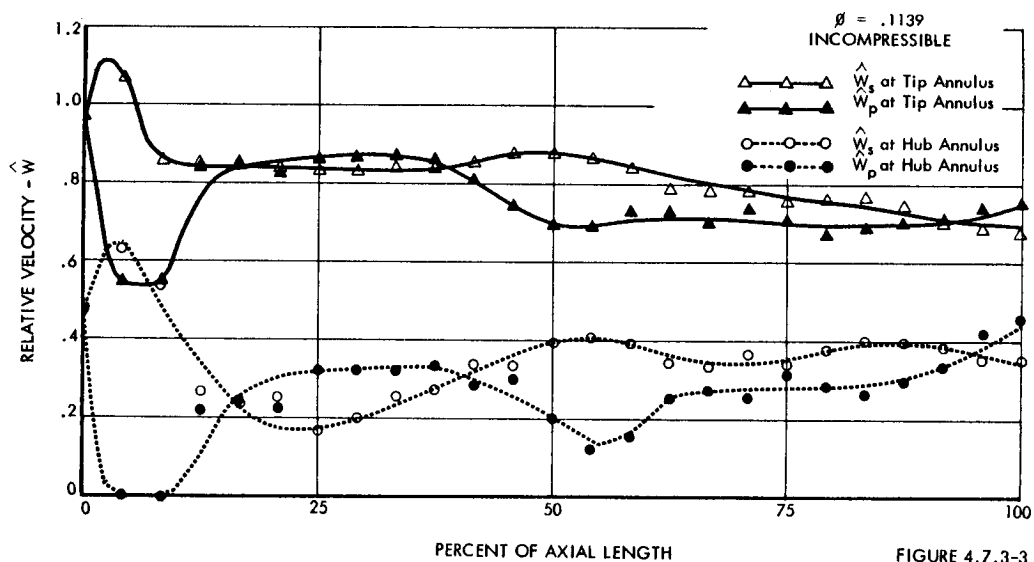


FIGURE 4.7.3-1

THEORETICAL PRESSURE DISTRIBUTION ON BLADES
WATER AT 82°F AND 16,000 RPM
(OR ANY FLUID FOR $R_e = 5.1 \times 10^6$)



THEORETICAL RELATIVE VELOCITY DISTRIBUTIONS ON BLADES
WATER AT 82°F AND 16,000 RPM
(OR ANY FLUID FOR $R_e = 5.1 \times 10^6$)





THEORETICAL PRESSURE DISTRIBUTION ON BLADES
NO LOSS

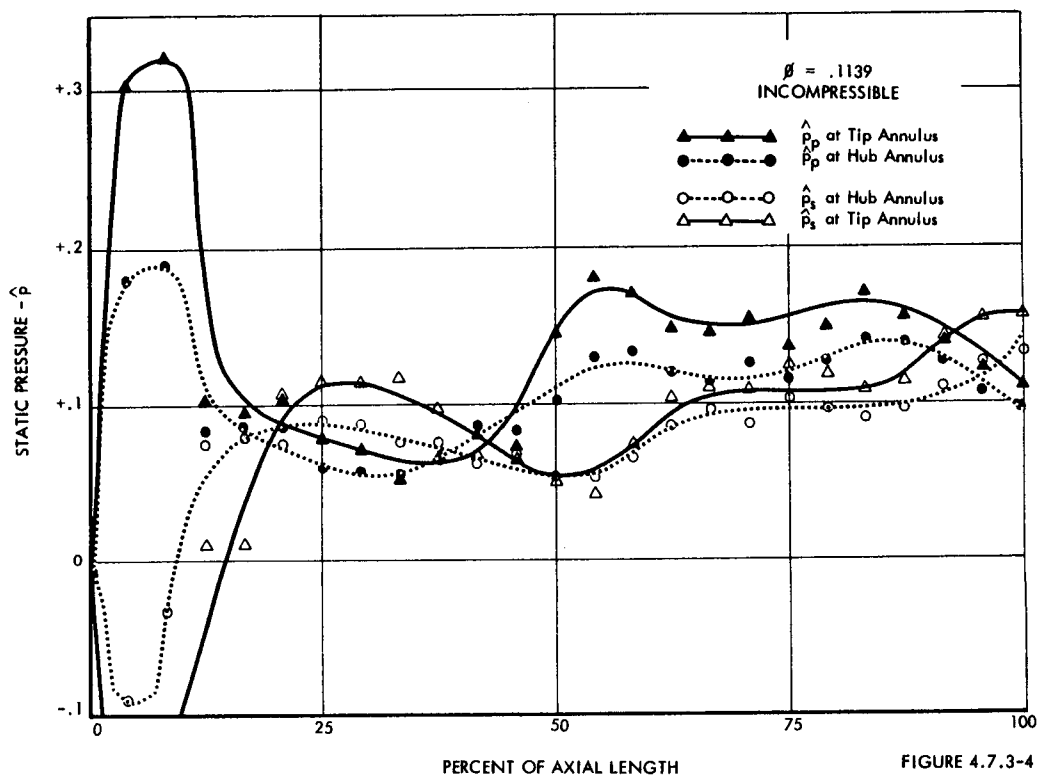


FIGURE 4.7.3-4

THEORETICAL RELATIVE VELOCITY DISTRIBUTIONS ON BLADES
NO LOSS

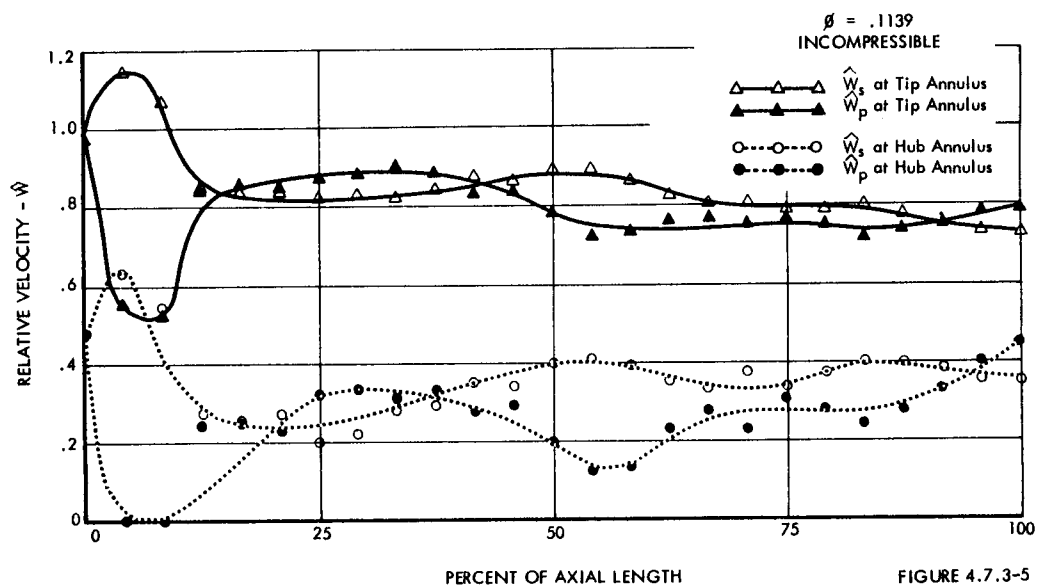
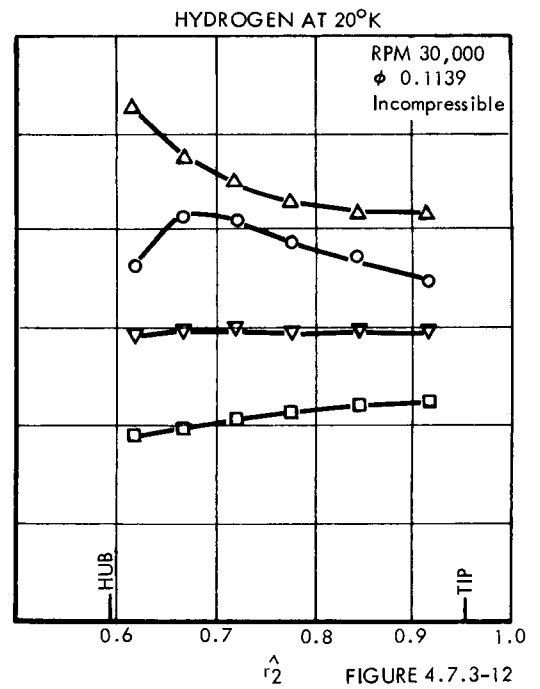
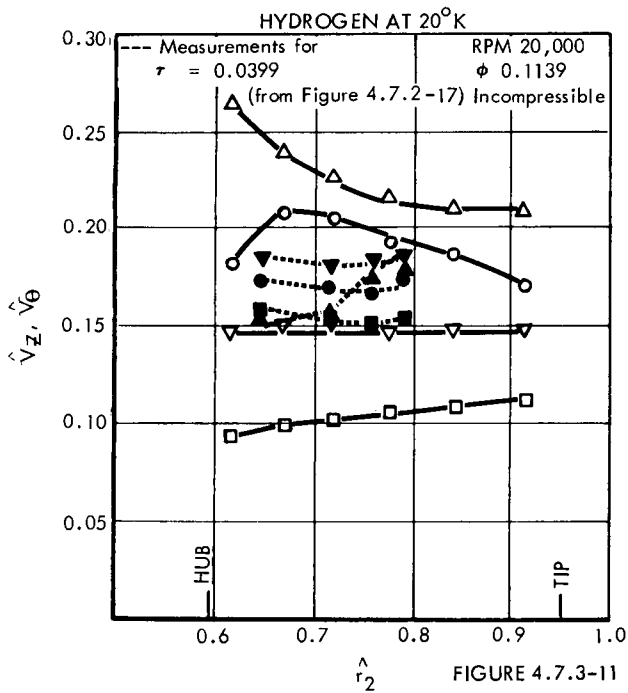
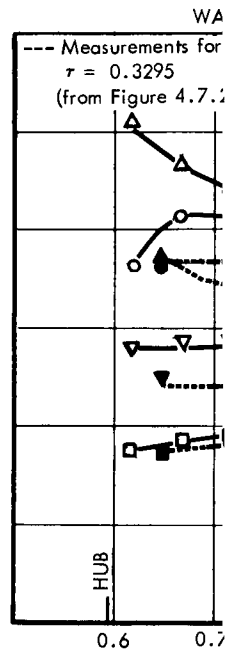
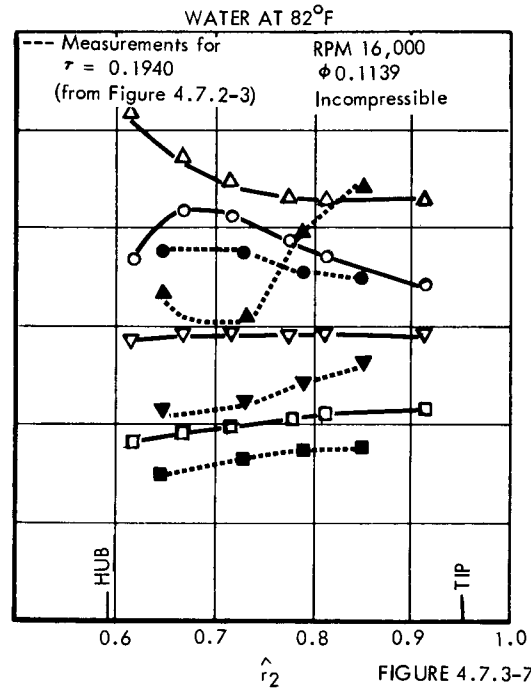
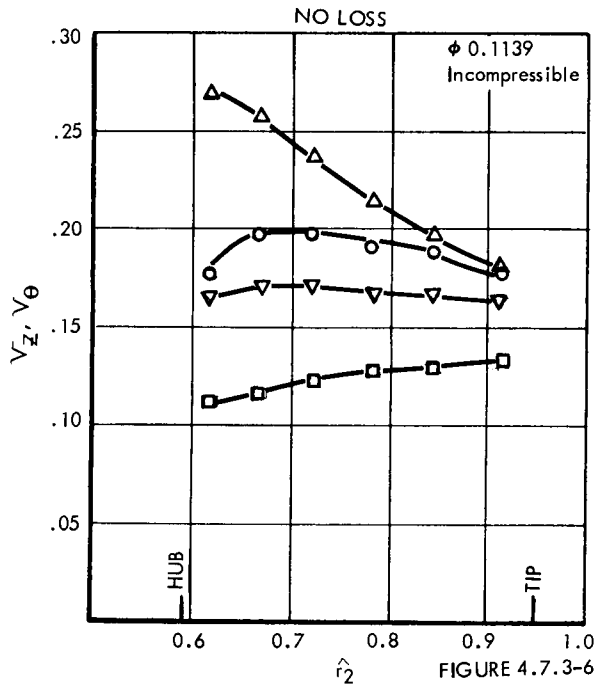


FIGURE 4.7.3-5



THEORETICAL VELOCITY AND



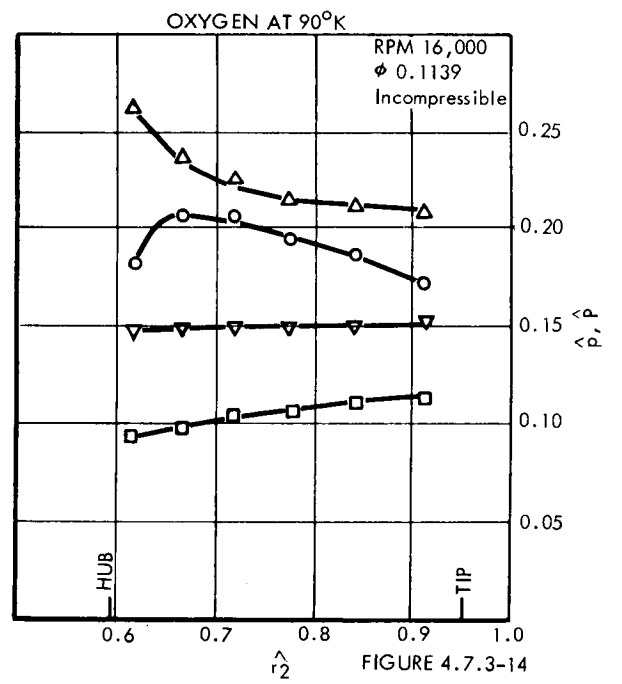
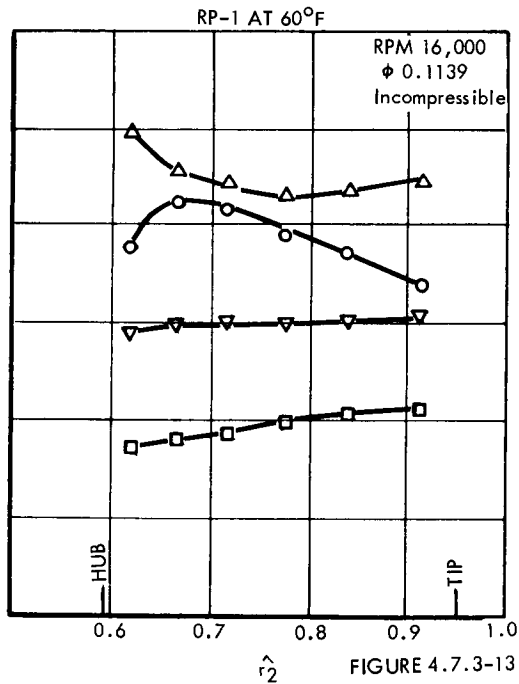
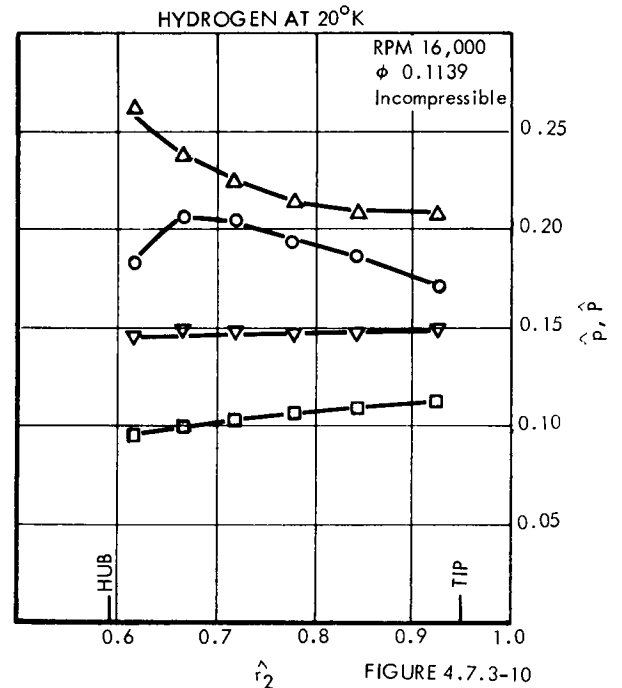
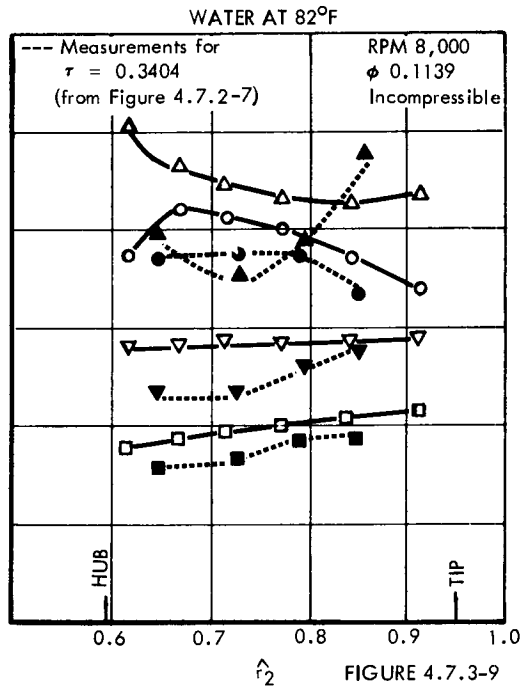
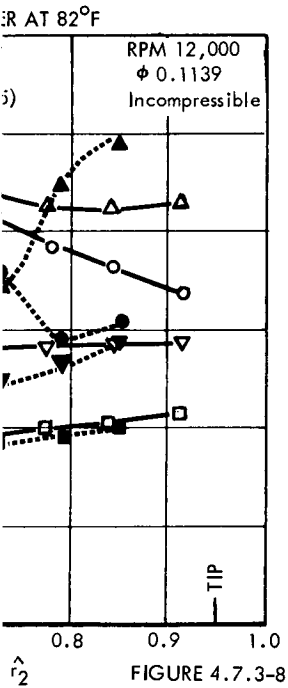
$$V_z = \frac{V_z}{U_{1,t}} : \circ$$

$$\hat{p} = \frac{g_o (p - p_1)}{\rho_f U_{1,t}^2} : \square$$

$$\hat{p} = \frac{g_o (P - P_1)}{\rho_f U_{1,t}^2} : \nabla$$

$$V_\theta = \frac{V_\theta}{U_{1,t}} : \Delta$$

PRESSURE DISTRIBUTION VS RADIUS



Although zero flow deviation angles δ were used, the static pressure and relative velocity distributions on the blades (cf. Figures 4.7.3-2, 4.7.3-3, 4.6.3-4, 4.7.3-5) show negative loading at outlet. If such loading reversal does in fact occur there, it may be primarily attributed to this characteristic behavior of the average inducer in incompressible flow. The blade angles β and the cross-sectional flow areas, as evidenced by hub-shroud contours, are such that most of the loading occurs in the "front" or leading portion of the rotor. However, under vaporizing fluid conditions, this loading pattern is shifted and the latter portions then load positively. In this way, an inducer continues to pump successfully at low NPSH. However, these plots of p and W distributions versus axial distance show the following:

- a. The blades are heavily loaded at inlet at the chosen, approximately optimum ϕ of 0.1139. A higher value of ϕ would eliminate this but would create other internal loading reversal problems.
- b. The blades unload at the juncture of the helical and circular arc portions of the inducer (see Figures C-1 and C-2.) There is a definite reversal of loading at this point.
- c. The circular arc portion loads fairly well, except for some variations that are probably due to numerical inaccuracies of the calculations (see Section 4.2.4).
- d. For the blade co-ordinates used, a rather "natural" unloading with some small reversal occurs at the exit with no allowance for deviation of the flow from the blade.
- e. The distributions for the zero loss case (Figures 4.7.3-4 and 4.7.3-5) show a greater loading reversal (see (b) above) than does the other case with loss (Figures 4.7.3-2 and 4.7.3-3).

Note (b) is illustrated rather dramatically in Figure 4.6.5-1 by the pitting that occurred on the suction sides of the rotor blades. Local collapsing of bubbles, which ordinarily exist on this side of the blades, and which collect there due to tip vortex activity, resulted from the sudden application of pressure loading at the suction sides and caused the pitting.

Compressible analyses were conducted on the leading 8%, or inlet portion, of the inducer with the same quasi three-dimensional program. These results show the ability of this analysis method to describe the blade unloading that occurs at inlet under cavitating conditions. The loop in which compressible radial equilibrium is iterated needs some improvements to make it capable of handling values of τ lower than 0.08. Also it was not possible to make the program calculate flow beyond the point of reversed loading discussed in note (b) above. However, in its present form, the program might calculate the complete flow field (at this τ) of a rotor that does not have reversed loading.



Part of the calculation problem is one of avoiding, during the iteration, the two-phase, negative-loading combination that is discussed in Section 4.5.3 as a limiting condition on the flow rate. Another problem concerns the change in mathematical behavior of the radial equilibrium residual (cf. Figure 4.2.4-3), because of the discontinuous density variation due to a change from single to two-phase flow somewhere between the blades, (cf. Section 4.2.3 and Figure 4.2.3-1). (Three annuli were used for these calculations.)

Figure 4.7.3-15 shows the head coefficient obtained by this "front" portion of the inducer due to the reduction of τ . Since $\frac{\tau}{2} \geq -\hat{p}_{min}$ to prevent vaporization, the limiting value of τ above which the flow is incompressible was found from the minimum pressure coefficient $\hat{p}_s = -0.133$ for the incompressible case in the pressure distributions of Figure 4.7.3-17 (see Section 4.4.5 and Figure 4.4.5-1). This reduction in pressure rise for the leading portion of the inducer shifts the loading farther back into the rotor as τ is reduced. This is shown graphically in the unloading phenomenon presented in Figure 4.7.3-17. Since the average relative velocities are thereby higher and, therefore, the friction losses also higher, the efficiency versus τ curve of Figure 4.7.3-16 is obtained. The relative velocities are shown in Figure 4.7.3-18. The high values of W_S calculated where the fluid is two-phase illustrate the limitations of the linear pressure method used for the blade-to-blade analysis, as discussed in Section 4.2.3 (cf. Figures 4.2.3-1 and 4.2.3-2).

Distributions of \hat{V}_x , \hat{V}_θ , \hat{p} , and \hat{P} at the "exit" of this front portion of the inducer are shown for the five cases of τ that were investigated in the compressible work in Figures 4.7.3-19 to 4.7.3-23. The incompressible case ($\tau \geq 0.266$) shown in Figure 4.5.3-19 reveals the initial tendencies of the blading to create the distributions observed at the outlet in Figures 4.5.3-7 to 4.5.3-14. As τ is decreased, these distributions "flatten out" due to the unloading phenomenon of Figure 4.7.3-17. These calculations were done with $\epsilon = 0.03$ (see equation 4.2.4-3). A value of $\epsilon = 0.01$ was used for the incompressible calculations. At the lowest τ , V_x is larger because the average density $\bar{\rho}$ is below that of the liquid (see Figure 4.2.3-1); V_θ is small because of the very low loading; and the static and total pressures are nearly constant because of the near absence of tangential absolute fluid motion.

As discussed in Section 4.7.2, some revealing information was obtained in the vented-tank hydrogen run of data points 11 - 19 in Table 4.6.5-2. As shown in Section 4.5.4, Figure 4.5.4-2, and Table 4.5.4-1, in one-dimensional duct flow calculations using the equation of state evolved in equation (4.1.2-8) for a vaporizing fluid, the state of the two-phase fluid was obtained at the inducer inlet. Table 4.7.4-1 shows that the static pressure was 3/4 psi below the vapor pressure (at the start of vaporization) of the fluid. Further calculations revealed the NPSH to be -2.6 ft-lbf/lbm at this condition. The inlet volume flow was equivalent to a ϕ of 0.114 and, had it not been for the pressure drop limitations of the test loop, which limited the flow at this test point, the inducer should probably have passed a higher mass flow rate before the limiting phenomenon of negative loading in two-phase flow would have occurred (see Section 4.5.3).

"HEAD COEFFICIENT" OF INITIAL 8-1/3% OF INDUCER
VS.
CAVITATION PARAMETER

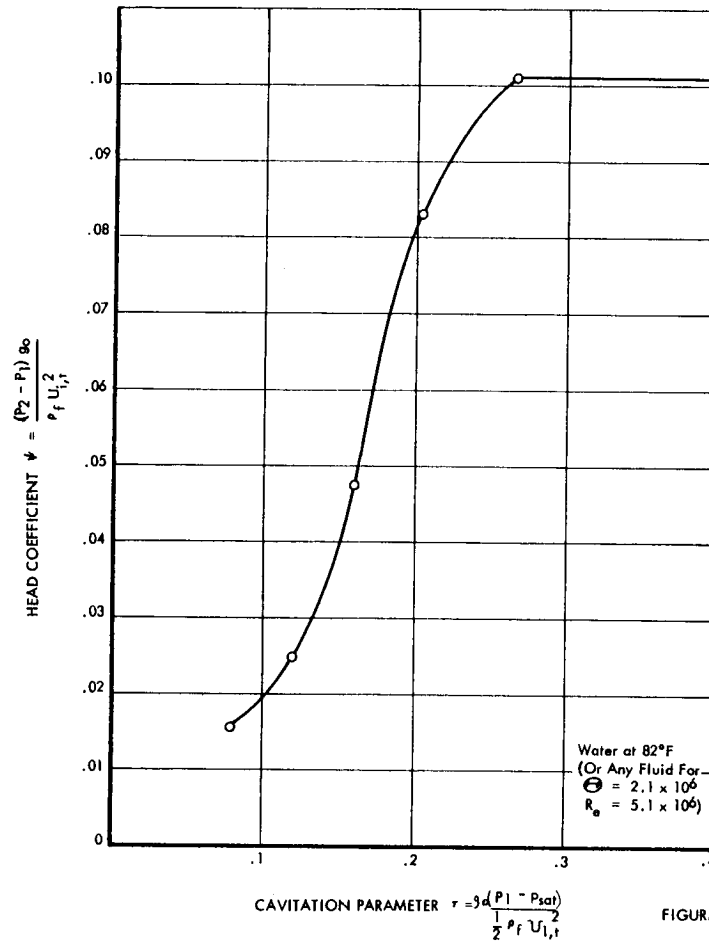


FIGURE 4.7.3-15

EFFICIENCY OF INITIAL 8-1/3%
OF INDUCER VS CAVITATION PARAMETER

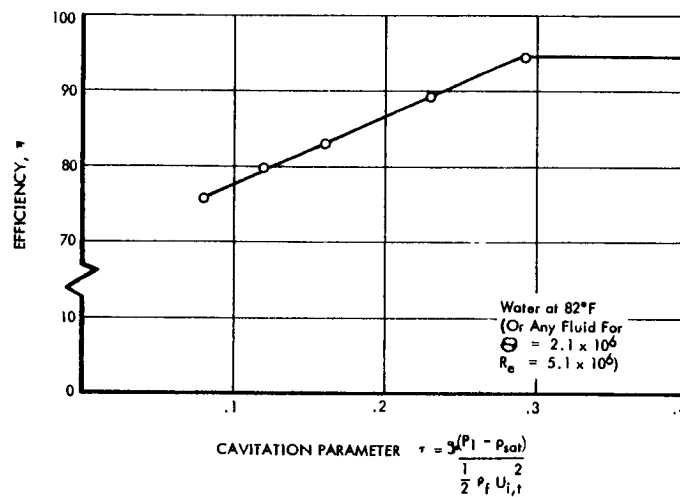


FIGURE 4.7.3-16



THEORETICAL PRESSURE DISTRIBUTION ON BLADES MEAN ANNULUS

Water at 80°F

(Or Any Fluid For $\rho = 2.1 \times 10^6$)

$R_e = 5.1 \times 10^6$)

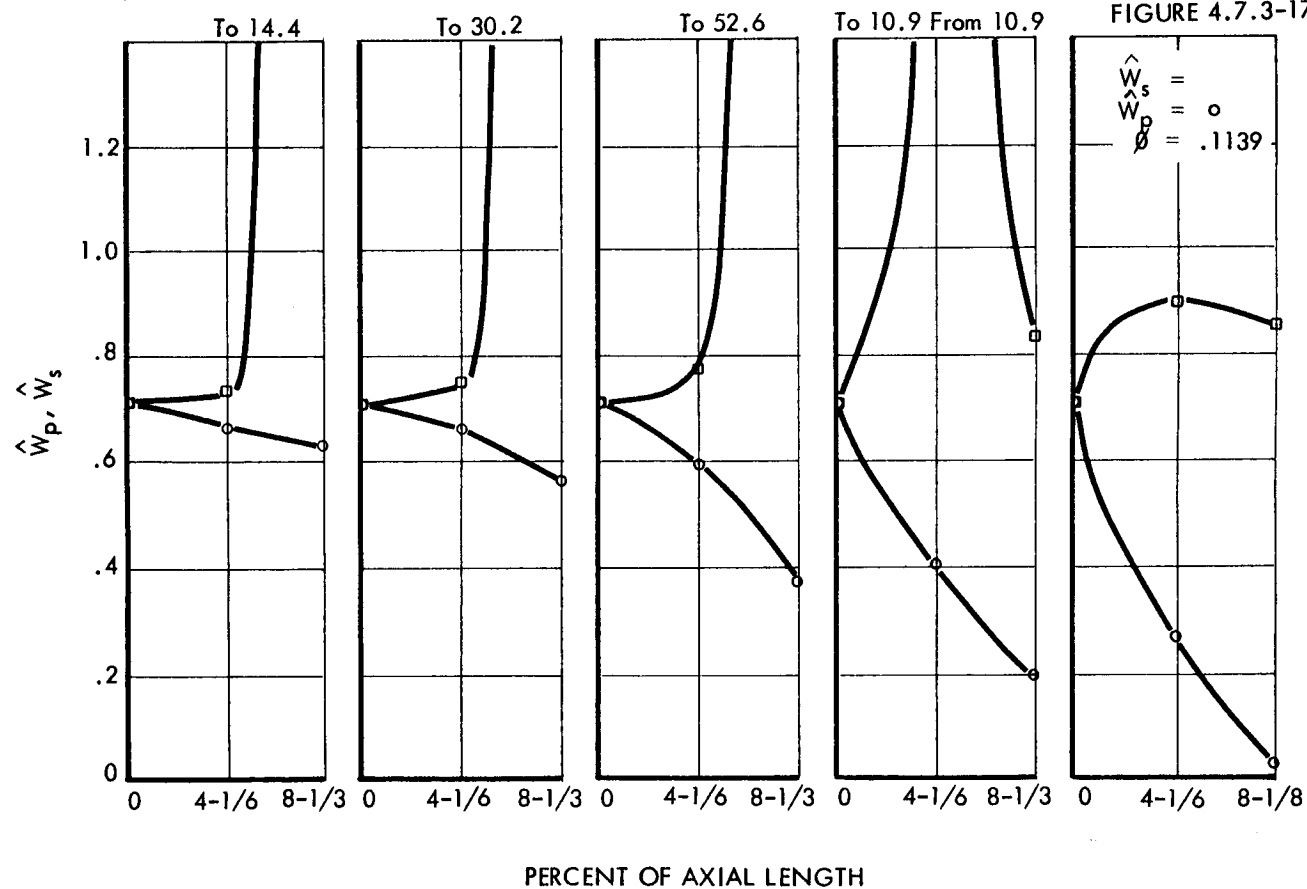
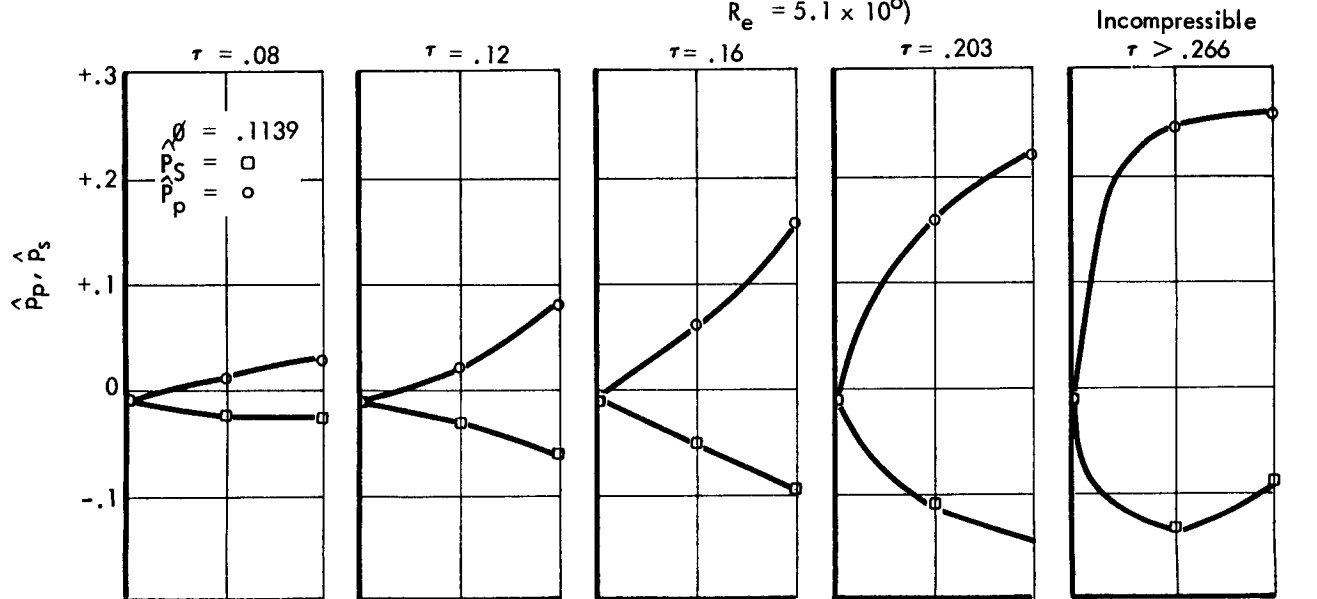


FIGURE 4.7.3-18

THEORETICAL VELOCITY AND PRESSURE DISTRIBUTIONS VS RADIUS

WATER AT 82°F

(Or Any Fluid For
At Axial Stations 8-1/3% of the
Way Through the Inducer)
 $\rho = 2.1 \times 10^6$
 $R_c = 5.1 \times 10^6$

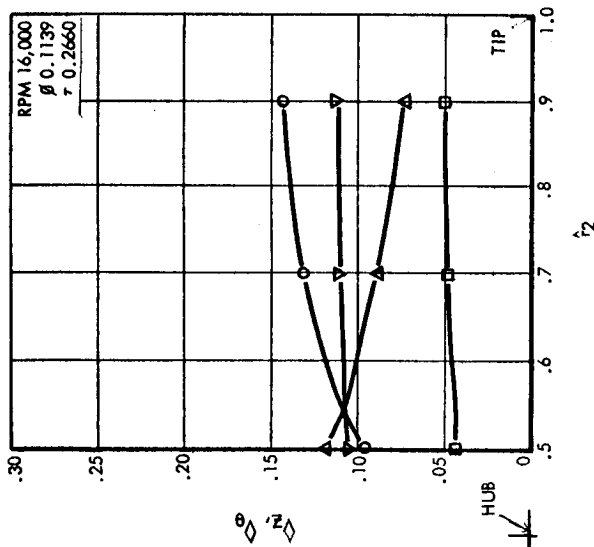


FIGURE 4.7.3-19

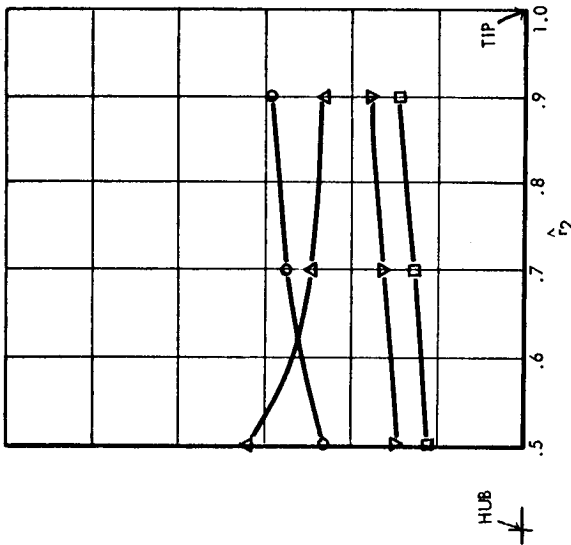


FIGURE 4.7.3-20

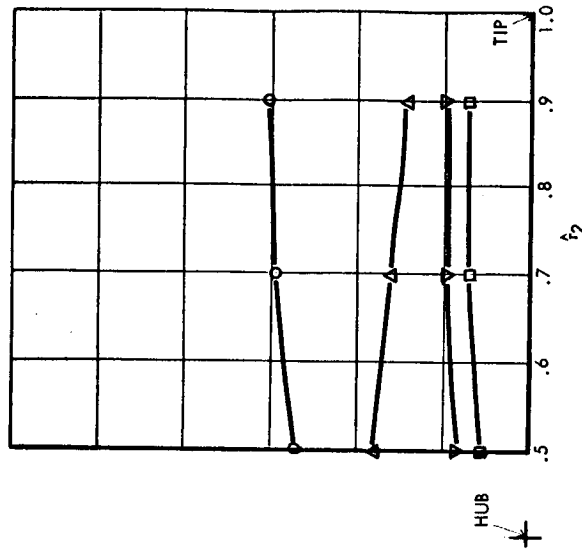


FIGURE 4.7.3-21

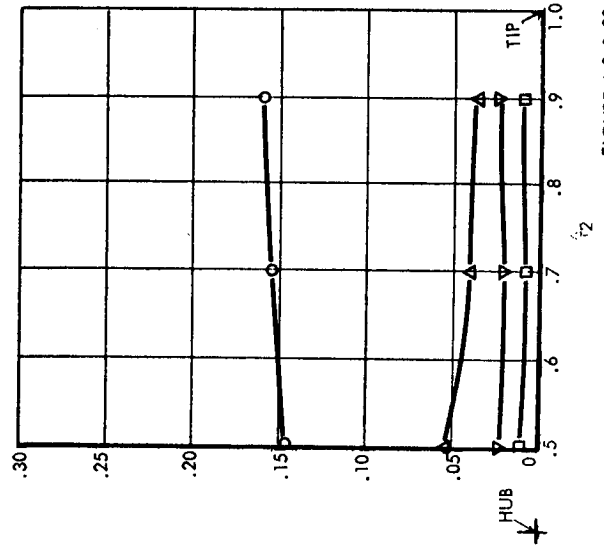


FIGURE 4.2.3-22

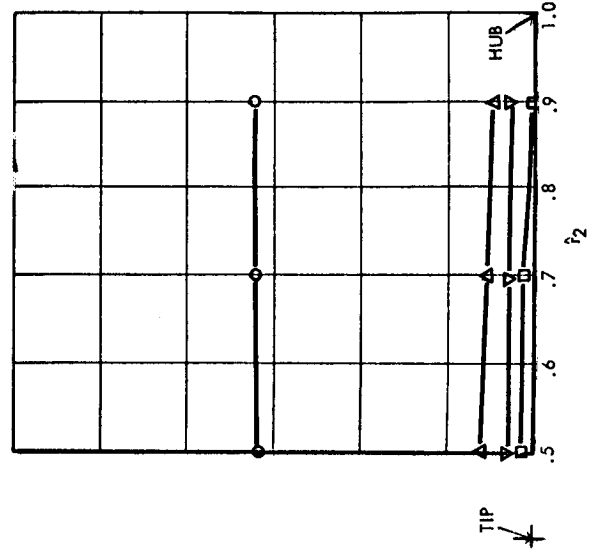


FIGURE 4.7.3-23

$$\begin{aligned} \hat{V}_z &= \frac{V_z}{U_{1,t}} & \text{O} \\ \hat{V}_\theta &= \frac{V_\theta}{U_{1,t}} & \Delta \\ \hat{P} &= \frac{P - P_1}{\rho_f U_{1,t}^2} & \square \\ \hat{P} &= \frac{P - P_1}{\rho_f U_{1,t}^2} & \nabla \end{aligned}$$



4.7.4 Conclusions

The ability of a homogeneous, two-phase flow model to describe the occurrence in an inducer has been demonstrated with a quasi three-dimensional solution. Furthermore, incompressible calculations of inducer performance have shown the method of loss description in this model to be reasonable. At least qualitative agreement with test results has been achieved, and with proper modification in the compressible calculation method, this capability could be extended into the negative τ regime from presently calculable results at $\tau \geq 0.08$. The ability to describe the fluid state at the inlet of the inducer in a vaporizing fluid has been demonstrated for the case of liquid hydrogen, (Section 4.5.4).

Further study and correlation of the results should be conducted to determine what modifications are required for the presently successful analysis methods. Modifications must be made to the quasi three-dimensional program to allow analysis of the lower τ conditions. Also, the compressible program has not yet analyzed a complete inducer, although the proper combination of circumstances could show this to be possible. Computer running time for an inducer with 25 axial stations and 6 annuli is approximately one hour (IBM 7070 digital computer) for an incompressible calculation. Relaxation of the $.01 \epsilon$ requirement speeds up the calculation, and this is imperative for the compressible calculations as they now stand. The improvements in the iteration loop would make it possible to demand more accuracy for reasonable lengths of running time.

APPENDIX A

NOMENCLATURE

Nomenclature not explained in this Appendix is described concurrently as it appears in the text. Unless otherwise described in the text, the meanings given below apply.

1. Symbols

A	Cross-sectional area of passage
a	Constant in diffusion loss equation (4.1.3-8)
B	Vapor-to-liquid volume ratio
D	Diameter
D_h	Hydraulic diameter
d	Pipe diameter
F	Friction force
f	Friction loss factor
g_0	Constant in Newton's second law $(F = \frac{1}{g_0} ma) [g_0] = \left[\frac{\text{Mass} \cdot \text{Length}}{\text{Force} \cdot \text{Time}^2} \right]$
h	Enthalpy
h	Height of liquid level
K_1	Constant in blade-to-blade pressure distribution
K_2	Constant in blade-to-blade velocity distribution
k	Cavitation number
k	Axial station within inducer $(1 \leq k \leq n)$
k	Diffusion loss factor
L	Loss
L_a	Friction loss



L_b	Diffusion loss
l	Length in direction of flow
m	Meridional distance
N	Rotative speed
$NPSH$	Net positive suction head
n	Number of axial stations within inducer
n_b	Number of blades
P	Total (stagnation) pressure
ρ	Power
p	Pressure (static)
ρ	perimeter
Q	Volume flow rate
R	Gas constant - (equation (4.4.3-3) only)
R	Reynolds number
Re	Reynolds number
R	Residual
r	Radius
S	Suction specific speed (dimensionless)
s	Entropy
T	Temperature
\mathcal{T}	Thermodynamic constant
t	Blade thickness

U	Blade velocity ($= \Omega r = \pi DN$)
U_{∞}	Free stream velocity ¹⁰
u	Internal energy
V	Absolute velocity
$\frac{V}{L}$	Vapor-to-liquid volume ratio
v	Specific volume
W	Velocity of fluid relative to blade system
\dot{W}	Mass flow rate
X	Quality parameter
x	Quality
z	Distance along inducer axis of rotation
β	Angle between blade and axial direction
β'	Angle between blade and tangential direction
δ	Deviation angle
δ^*	Boundary layer displacement thickness
ϵ	Accuracy criterion in numerical solution
η	Efficiency
Θ	Thermodynamic parameter
θ	Angle measured in plane normal to inducer axis
λ	Distance in the streamline direction
μ	Absolute viscosity
ν	Kinematic viscosity ($= \frac{g_o \mu}{\rho}$)
ξ	Hub-to-tip radius ratio



ρ	Density (using a system having independent units of force and mass; e.g. $[\rho] = \left[\frac{lb\ m}{ft^3} \right]$)
σ	Surface tension
σ	Solidity
τ	Cavitation parameter
ϕ	Flow co-efficient
χ	Bubble radius parameter
ψ	Total pressure (head) co-efficient
Ω	Angular velocity of blade system

2. Subscripts

a	Inlet to line (cf. Figure 4.5.4-2)
ave	Average
b	Blade direction (used only with β and β')
b	Bubble (equilibrium radius)
b	Station at end of inlet line (in Figure 4.5.4-2)
(f)	Value if same amount of mass flowing were in liquid form
f	Flow direction (used only with β and β')
f	Liquid
fg	Saturated vapor value minus saturated liquid value
g	Saturated vapor
H	Hydraulic (power)
h	Hub
i	Streamline
i	Annulus

<i>i</i>	Inside bubble
<i>j</i>	Juncture of inducer sections (cf. Figure C-3)
<i>k</i>	Axial station within inducer
<i>m</i>	Meridional component
<i>m</i>	Number of annuli
<i>n</i>	Number of axial stations from inducer inlet to outlet
<i>o</i>	Outside bubble
<i>o</i>	Tank
<i>p</i>	Pressure side of channel or blade
<i>r</i>	Radial component
<i>S</i>	Shaft (power)
<i>s</i>	Suction side of channel or blade
<i>sat</i>	Saturated liquid (the conditions at which the vaporization process starts)
<i>st</i>	Stagnation
<i>t</i>	Tip (shroud)
<i>T</i>	Throat
<i>z</i>	Axial component
<i>θ</i>	Tangential component
<i>1</i>	Inducer inlet (blade leading edge)
<i>2</i>	Inducer outlet (blade trailing edge)
<i>3</i>	Inducer outlet probe station



3. Superscripts

- \wedge Dimensionless notation
- \circ Unit vector notation
- $-$ Average value
- \rightarrow Vector notation

APPENDIX B

REFERENCES

1. Cooper, P. "Application of Pressure & Velocity Criteria to the Design of a Centrifugal Pump Impeller & Inlet." A.S.M.E. Paper No. 63-AHGT-58, 1963.
2. Stripling, L.B. & A.J. Acosta, "Cavitation in Turbopumps, Part 1." A.S.M.E. Paper No. 61-WA-112, 1961.
3. Stripling, L.B. "Cavitation Turbopumps, Part 2." A.S.M.E. Paper No. 61-WA-98, 1961.
4. Vavra, M.H. Aero-Thermodynamics & Flow in Turbomachines. John Wiley & Sons, New York, 1960, pp. 121, 122.
5. Keenan, J.H. Thermodynamics. John Wiley & Sons, New York, 1946, p. 329.
6. Roder, H.M. & R.D. Goodwin, Provisional Thermodynamic Functions for Para-Hydrogen. National Bureau of Standards TN 130, 1961.
7. Prandtl, L., & O.G. Tietjens, Applied Hydro- & Aeromechanics. Dover Publications, Inc., New York, 1934, p. 42.
8. Marks, L.S. Mechanical Engineers' Handbook, Fifth Edition. McGraw-Hill Book Co., Inc., New York, 1951, p. 250.
9. "Airplane Heating & Ventilating Equipment, Engineering Data, Fluid Dynamics." S.A.E. Aeronautical Information Report No. 23, New York, 1951.
10. Schlichting, H. Boundary Layer Theory. McGraw-Hill Book Co., Inc. New York, 1955.
11. Eichenberger, H.P. "A Contribution to the Aerodynamic Design of Mixed-Flow Compressors." A.S.M.E. Paper No. 57-A-61, 1957, Appendix.
12. Hamrick, J.T., A. Ginsburg, and W.M. Osborn. "Method of Analysis for Compressible Flow Through Mixed-Flow Centrifugal Impellers of Arbitrary Design." NACA Report 1082, Washington, 1952, Appendix D.
13. Stanitz, J.D., and V.D. Prian, "A Rapid Approximate Method for Determining Velocity Distribution on Impeller Blades of Centrifugal Compressors." NACA TN 2421, Washington, 1951.
14. Spang, H.A. "A Review of Minimization Techniques for Nonlinear Functions." SIAM Review, Vol. 4, No. 4, October, 1962, pp. 343-365.



REFERENCES (CONTINUED)

15. Keenan, J.H. Op. Cit., Chapter 25.
16. Keenan, J.H., & F.G. Keyes, Thermodynamic Properties of Steam. John Wiley & Sons, Inc., New York, 1946.
17. Mullins, J.C., W.T. Ziegler, & B.S. Kirk, "The Thermodynamic Properties of Oxygen from 20° to 100°K." Paper C-2 of the 1962 Cryogenic Engineering Conference, Los Angeles, August, 1962.
18. Jacobs, R.B. "Predictions of Symptoms of Cavitation." Journal of Research of the National Bureau of Standards, Engineering & Instrumentation, Vol. 65C, No. 3, July-September, 1961.
19. Stepanoff, A.J. "Cavitation Properties of Liquids." A.S.M.E. Paper No. 63-AHGT-22, 1963.
20. Ross, C.C., & G. Banerian, "Some Aspects of High Suction Specific Speed Pump Inducers". A.S.M.E. Paper No. 55-A-124, 1955.
21. Smith, R.V. "Some Idealized Solutions for Critical (Mass Limiting) Flow for Two-Phase Flow of Hydrogen, Nitrogen & Oxygen." Paper C-5 of the 1962 Cryogenic Engineering Conference, Los Angeles, August, 1962.
22. Keenan, J.H., Op. Cit., Chapter 18.
23. Hord, J., C.C. Robinson, & L.L. Sparks, "Effects of Liquid-Solid Interfaces on the Nucleation Characteristics of Cryogenic Liquids." A.S.M.E. Paper No. 63-AHGT-45, 1963.

APPENDIX C

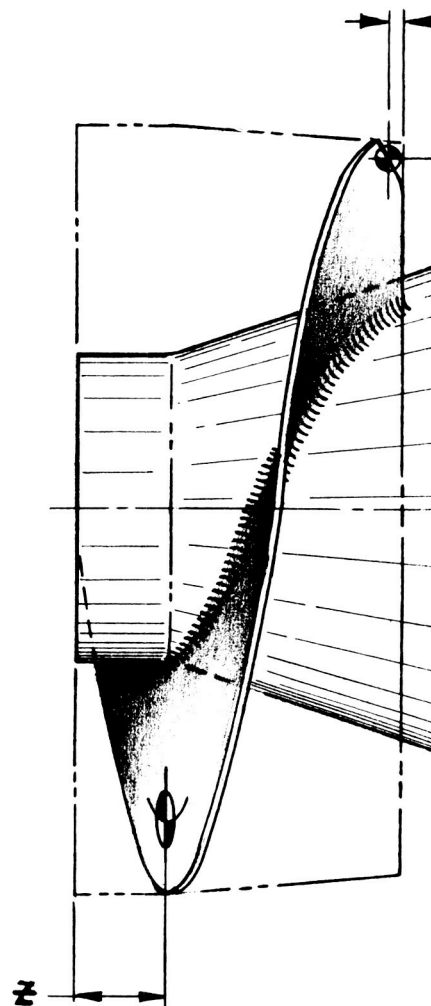
BLADE CONTOUR OF REFEREE INDUCER

An existing inducer was used as a basis for comparison between the results of tests and of analysis. Section 4.6 gives illustrations and a general description of this rotor. Since it was made from a master blade and at a scale of 4:6.5 of this blade, no list of co-ordinates of the blades was required for its manufacture. Upon receipt of the rotor, however, it was inspected so that a gaged record of the co-ordinates would be available if needed for any future checking and reference. This gaging was accomplished by setting a ball-end indicator against the suction surface of each blade at a given axial location Z (See Figure C-1). Then the indicator was moved radially and the inducer was rotated as required to maintain the same indicator reading (axial location of the the center of the ball). This procedure was followed for each blade at the given Z station and at several other such stations. A summary of the data for one blade is presented in Figure C-1. Figure C-2 is a drawing of the inducer to illustrate the blade thickness and the way in which the leading and trailing edges were fared.

These gage data were utilized to obtain the channel boundary description for the early trial calculations on the three-dimensional analysis program (See Section 4.3). However, small discontinuities (besides the one at the point where the helix portion of the blade joins the circular arc portion) in the gage data created difficulties in these calculations. When it was found that the data for the three blades showed disagreement, it was decided that a mathematical development of the blade co-ordinates should be employed for analytical purposes. This development followed steps of the kind utilized by NASA in the original design of the rotor. In order that a match of the helical and circular arc could be obtained, the blade elements were stacked in exactly the same way at this juncture; viz., at $Z = 0.492$ in. (See Figure C-3). Typical data from the gage measurements in the helical section were used to determine this method of stacking on a plane of constant Z . The shape of line that this gives on the Z - plane was used at Z , and at all stations for $0 < Z \leq Z_j$, the angular spacing being determined by the 80.5 degree blade tip helix angle β_b, t . Figure C-3 shows the NASA - LeRC design data used for the circular arc portion of the blade. The shape of the blade suction surface on the developed cone for each meridional line was obtained by transforming numerically the co-ordinates of a circular arc drawn graphically in a rectangular system of co-ordinates x'' and y'' , where $(x_j'' - x_2'')$ was equal to the meridional line length, according to the formula

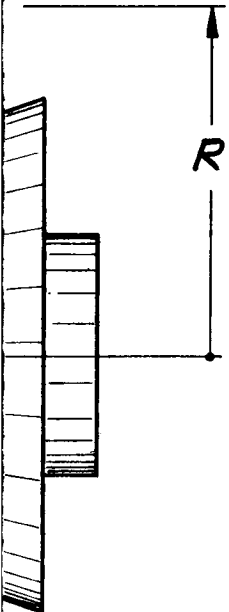
$$\tan \beta_b = \frac{r d\theta}{dm} = \frac{dy''}{dx''} \quad (C-1)$$

At several chosen axial (Z) stations from Z_j to Z_2 , the resulting shapes of the circular arc blade from hub to tip on the $r-\theta$ (constant Z) plane were plotted and checked. These



THREE BLADES EQUALLY SPACED
ONLY ONE BLADE SHOWN FOR CLARITY

-Z



$z = 0.000$

r	2.002	1.834	1.666	1.498	1.330	1.162	.994
$\theta -$	0°	$1^\circ 10'$	$3^\circ 10'$	$5^\circ 20'$	$7^\circ 55'$	$10^\circ 10'$	$15^\circ 10'$

$z = 0.050$

r	2.004	1.836	1.668	1.500	1.332	1.164	.996
$\theta +$	$16^\circ 42'$	$16^\circ 17'$	$15^\circ 34'$	$14^\circ 54'$	$13^\circ 29'$	$12^\circ 17'$	$10^\circ 42'$

$z = 0.188$

r	2.002	1.834	1.666	1.498	1.330	1.162	.994
$\theta +$	$42^\circ 5'$	$41^\circ 50'$	$41^\circ 10'$	$40^\circ 23'$	$39^\circ 24'$	$38^\circ 00'$	$36^\circ 52'$

$z = 0.446$

r	2.002	1.834	1.666	1.498	1.330	1.162	.994
$\theta +$	$95^\circ 47'$	$96^\circ 52'$	$96^\circ 52'$	$95^\circ 55'$	$94^\circ 33'$	$93^\circ 6'$	$92^\circ 36'$

$z = 0.744$

r	1.978	1.810	1.642	1.474	1.306	1.138	.996
$\theta +$	$142^\circ 40'$	$145^\circ 15'$	$147^\circ 5'$	$147^\circ 3'$	$146^\circ 17'$	$144^\circ 38'$	$143^\circ 45'$

$z = 1.015$

r	1.957	1.827	1.697	1.567	1.437	1.307	1.177
$\theta +$	$189^\circ 15'$	$190^\circ 8'$	$190^\circ 30'$	$190^\circ 30'$	190°	$188^\circ 40'$	$187^\circ 50'$

$z = 1.286$

r	1.933	1.803	1.673	1.543	1.413	1.283	1.153
$\theta +$	239°	234°	$230^\circ 30'$	$227^\circ 40'$	225°	$223^\circ 40'$	$223^\circ 40'$

$z = 1.557$

r	1.916	1.816	1.716	1.616	1.516	1.416	-
$\theta +$	$276^\circ 25'$	$272^\circ 40'$	268°	263°	260°	257°	-

$z = 1.692$

r	1.620	1.570	1.520	1.470	1.420	1.370	1.320	1.270
$\theta +$	277°	276°	$274^\circ 20'$	$272^\circ 50'$	$270^\circ 50'$	$269^\circ 30'$	$268^\circ 50'$	$268^\circ 20'$

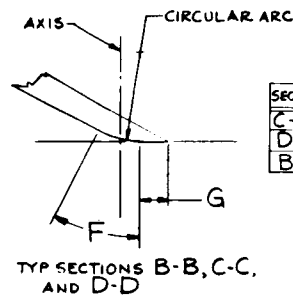
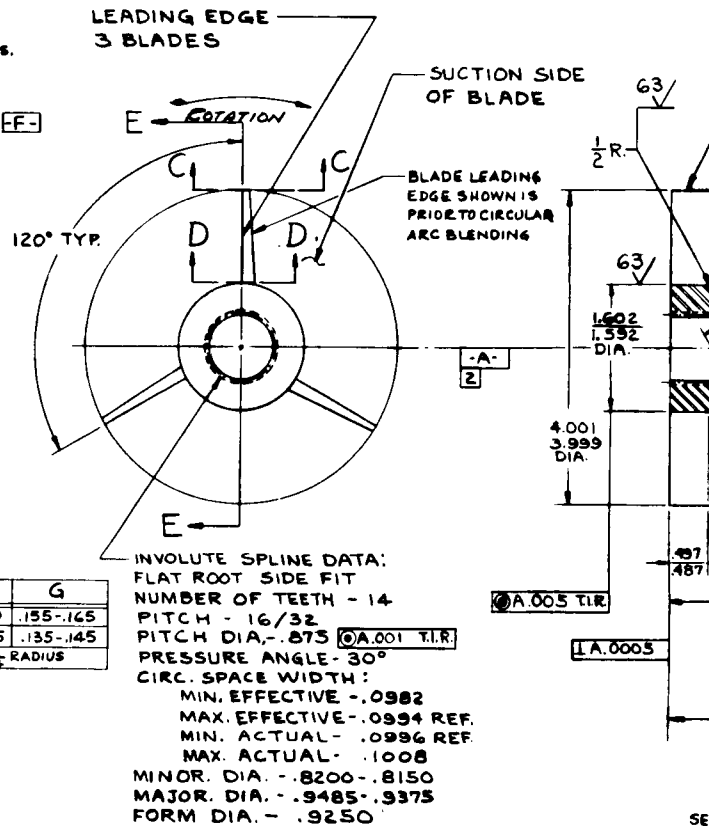
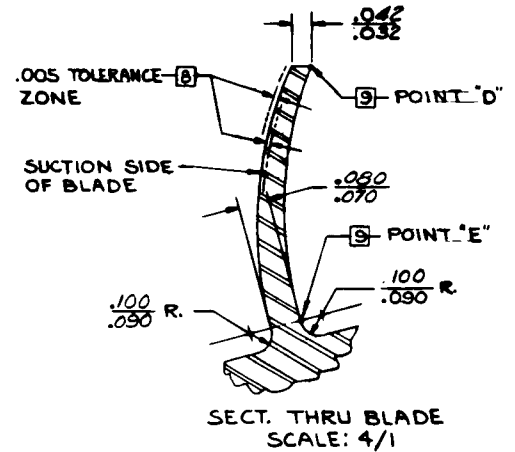
R	Z
1.620	0
1.670	0.005
1.720	0.035
1.770	0.060
1.820	0.095
1.870	0.140

TYPICAL BLADE CONTOUR
GAGE DATA
NO. 1 BLADE
SK 17761

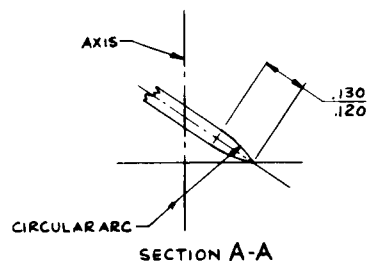


NOTES UNLESS OTHERWISE SPECIFIED

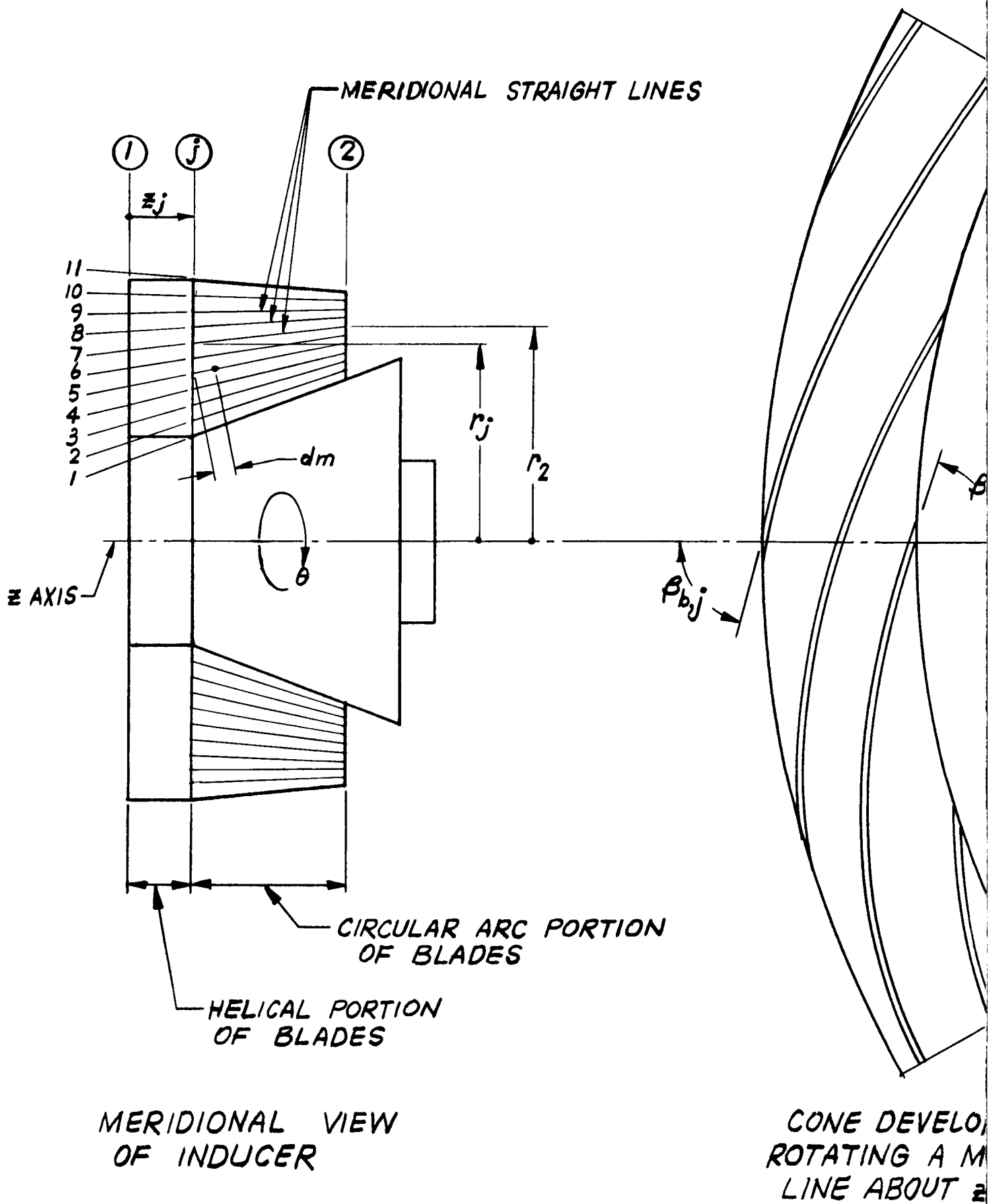
1. BLADE CONTOUR TO BE PER NASA INDUCER MASTER (DWG. NO. CDB40806) REDUCED IN SIZE BY THE RATIO OF 6.5 TO 4.0 INCHES.
2. AXIS -A- IS DETERMINED BY A LINE PASSING THRU THE CENTER OF -B- AND PERPENDICULAR TO PLANE -C- IN CONTACT WITH HIGH POINT OF SURFACE -D-.
3. $\sqrt[63]{}$ FINISH ALL OVER EXCEPT AS NOTED. (SEE NOTE 4)
4. BLADES TO HAVE $\sqrt[63]{}$ FINISH ALL OVER.
5. MATERIAL TO BE QQ-N-286, CLASS A, ANNEALED (K-MONEL)
6. AGE HARDEN TO Rc 31-34.
7. PENETRANT INSPECT IN FINISH PER MIL-I-6066, TYPE I. NO CRACKS, SEAMS, INCLUSIONS, OR OTHER DEFECTS ALLOWABLE.
8. SUCTION SIDE OF BLADE MUST BE WITHIN TOLERANCE ZONE SHOWN WITH RESPECT TO NASA MASTER CONSIDERED AS BASIC FORM.
9. BLADE THICKNESS TO INCREASE UNIFORMLY FROM POINT "D" TO POINT "E".
10. THE LEADING & TRAILING EDGE CIRCULAR ARCS ARE TO BE TANGENT TO THE REMAINING PORTIONS OF THE BLADE.
11. POLISH BOTH SIDES OF BLADE AT LEADING & TRAILING EDGES.
12. BLEND LENGTHS F & G UNIFORMLY FROM SECTION C-C TO SECTION D-D.
13. BLEND AS REQUIRED AT INTERSECTION OF SURFACES -E- & -F-.



SECTION	F	G
C-C	.150-.160	.155-.165
D-D	.225-.235	.135-.145
B-B	BLEND $\frac{1}{2}$ RADIUS	



[illegible]



MERIDIONAL STRAIGHT LINE NUMBER	INLET TO CIRCULAR ARC SECTION		OUTLET OF ROTOR	
	RADIUS, r_j (INCHES)	ANGLE $\beta_{b,j}$ (DEGREES)	RADIUS, r_2 (INCHES)	ANGLE $\beta_{b,2}$ (DEGREES)
1	0.798	71.92	1.203	59.18
2	0.986	74.71	1.276	62.23
3	1.143	76.36	1.348	64.87
4	1.283	77.49	1.415	67.15
5	1.409	78.32	1.482	69.11
6	1.522	78.97	1.550	70.82
7	1.630	79.49	1.618	72.46
8	1.730	79.92	1.681	74.08
9	1.826	80.28	1.751	75.83
10	1.914	80.59	1.820	77.77
11	2.000	80.87	1.900	79.92

NASA DESIGN DATA FOR CIRCULAR
ARC SECTION OF REFEREE INDUCER

PERIOD BY
MERIDIONAL
AXIS

were found to be satisfactory except near outlet where some slight adjustments were made to smooth the data and to bring them closer to the gage data. Data were taken from each of the plots, and allowance was made for boundary layer thickness as described in Section 4.2.2 and for blade thickness t . Thus, corresponding data for the effective channel boundaries were obtained by a short computer program as follows:

$$\theta_s = \theta + \frac{\delta^* \sec \beta_b}{r} \quad (C-2)$$

$$\theta_p = \theta + \frac{2\pi}{n_b} - \left(\frac{t + \delta^*}{r} \right) \sec \beta_b \quad (C-3)$$

where

$$t = t_h + (t_t - t_h) \left(\frac{r - r_h}{r_t - r_h} \right) \quad (C-4)$$

and t_h, t_t are constants given in Figure C-2. The results are presented in Table C-1. These were used for all runs of the analysis program, polynomials being fitted to the data at each Z - station to obtain analytic curves for the blade shape, as required by the programs described in Sections 4.2 and 4.3.

The blade shape thus evolved, while different in details such as the location of the tip of the trailing edge and the stacking point of the blade elements, was regarded as being reasonably close to that of the actual inducer. It was sufficient for use in the calculations which show, up to this point, how such an analysis should work. Questions of doubt about blade contour need to be eliminated if useful correlations are to be made with test data.



NASA ADVANCED INDUCER STUDY
ER 5288 APPENDIX C
TAPCO DIVISION
THOMPSON RAMO WOOLDRIDGE, INC.

5/15/63
TABLE C-1

BLADE COORDINATES & CHANNEL BOUNDARIES USED TO ANALYZE REFEREE INDUCER

STATION 1	Z IS 0.0000	RADIUS	THETA	BETA	THETA	
					SUCTION	PRESSURE
		0.8000	-17.2001	10.8275	-17.2001	102.8004
		1.0000	-11.3000	9.7940	-11.3000	108.7004
		1.2000	-7.4000	8.8983	-7.4000	112.6004
		1.4000	-4.9000	8.0114	-4.9000	115.1004
		1.6000	-2.9000	7.3397	-2.9000	117.1005
		1.8000	-1.3000	6.8431	-1.3000	118.7005
		2.0000	0.0000	6.3670	0.0000	120.0005

STATION 2	Z IS 0.0705	RADIUS	THETA	BETA	THETA	
					SUCTION	PRESSURE
		0.8000	9.2000	22.4832	9.2985	115.0556
		1.0000	12.1000	18.3195	12.1959	119.4887
		1.2000	14.1001	15.4249	14.1944	122.8187
		1.4000	15.6001	13.3058	15.6936	125.5524
		1.6000	16.7001	11.6915	16.7930	127.8354
		1.8000	17.4001	10.4226	17.4926	129.6892
		2.0000	18.1001	9.3999	18.1923	131.5253

STATION 3	Z IS 0.1410	RADIUS	THETA	BETA	THETA	
					SUCTION	PRESSURE
		0.8000	21.4001	22.4832	21.5970	127.1572
		1.0000	24.3001	18.3195	24.4918	131.5929
		1.2000	26.3001	15.4249	26.4889	134.9243
		1.4000	27.8001	13.3058	27.9871	137.6590
		1.6000	28.9001	11.6915	29.0860	139.9425
		1.8000	29.6001	10.4226	29.7852	141.7967
		2.0000	30.3001	9.3999	30.4846	143.6331

STATION 4 Z IS 0.2115

RADIUS	THETA	BETA	THETA	SUCTION	THETA	PRESSURE
0.8000	33.6001	22.4832	33.8956	139.2587		
1.0000	36.5001	18.3195	36.7877	143.6971		
1.2000	38.5001	15.4249	38.7833	147.0300		
1.4000	40.0002	13.3058	40.2807	149.7655		
1.6000	41.1002	11.6915	41.3789	152.0496		
1.8000	41.8002	10.4226	42.0777	153.9043		
2.0000	42.5002	9.3999	42.7769	155.7409		

STATION 5 Z IS 0.2820

RADIUS	THETA	BETA	THETA	SUCTION	THETA	PRESSURE
0.8000	45.8002	22.4832	46.1941	151.3603		
1.0000	48.7002	18.3195	49.0836	155.8013		
1.2000	50.7002	15.4249	51.0778	159.1356		
1.4000	52.2002	13.3058	52.5742	161.8721		
1.6000	53.3002	11.6915	53.6719	164.1568		
1.8000	54.0002	10.4226	54.3703	166.0118		
2.0000	54.7002	9.3999	55.0691	167.8488		

STATION 6 Z IS 0.3525

RADIUS	THETA	BETA	THETA	SUCTION	THETA	PRESSURE
0.8000	58.0002	22.4832	58.4926	163.4619		
1.0000	60.9002	18.3195	61.3795	167.9055		
1.2000	62.9002	15.4249	63.3722	171.2413		
1.4000	64.4002	13.3058	64.8678	173.9786		
1.6000	65.5002	11.6915	65.9649	176.2639		
1.8000	66.2003	10.4226	66.6629	178.1193		
2.0000	66.9003	9.3999	67.3614	179.9566		

STATION 7 Z IS 0.4230

RADIUS	THETA	BETA	THETA	SUCTION	THETA	PRESSURE
0.8000	70.2003	20.5066	70.8453	174.2223		
1.0000	73.1003	17.1371	73.7138	179.1364		
1.2000	75.1003	14.6247	75.6969	182.7190		
1.4000	76.6003	12.8977	77.1788	185.7584		
1.6000	77.7003	11.5080	78.2666	188.2243		
1.8000	78.4003	10.3397	78.9598	190.1620		
2.0000	79.1003	9.3999	79.6537	192.0644		



STATION 8 Z IS 0.4935

RADIUS	THETA	BETA	THETA	THETA	THETA
			SUCTION	PRESSURE	
0.8000	83.7003	21.4183	84.4222	188.2694	
1.0000	86.2003	17.7592	86.8918	192.6119	
1.2000	88.0003	15.0061	88.6791	195.8298	
1.4000	89.2003	13.0587	89.8670	198.3945	
1.6000	90.1003	11.5076	90.7610	200.5297	
1.8000	90.7003	10.3435	91.3529	202.3719	
2.0000	91.3004	9.4472	91.9428	204.2075	

STATION 9 Z IS 0.5640

RADIUS	THETA	BETA	THETA	THETA	THETA
			SUCTION	PRESSURE	
0.8220	97.0004	21.4097	97.8036	201.8763	
1.0180	99.1004	17.7250	99.8780	205.6341	
1.2130	100.7004	14.9659	101.4698	208.5345	
1.4090	101.7004	12.9617	102.4630	210.7952	
1.6030	102.5004	11.4910	103.2551	212.8377	
1.7990	103.0004	10.3492	103.7462	214.5805	
1.9940	103.5004	9.3995	104.2405	216.2580	

STATION 10 Z IS 0.6345

RADIUS	THETA	BETA	THETA	THETA	THETA
			SUCTION	PRESSURE	
0.8450	110.0004	21.8027	110.8644	215.4447	
1.0360	111.8004	17.9695	112.6488	218.6472	
1.2260	113.3004	15.3986	114.1333	221.4996	
1.4170	114.2004	13.3024	115.0321	223.5346	
1.6070	114.9004	11.8302	115.7235	225.4449	
1.7980	115.3004	10.5221	116.1263	226.9221	
1.9880	115.8004	9.3527	116.6397	228.4069	

STATION 11 Z IS 0.7050

RADIUS	THETA	BETA	THETA	THETA	THETA
			SUCTION	PRESSURE	
0.8680	122.4005	21.6012	123.3433	228.0104	
1.0540	124.1005	18.3842	125.0068	231.3622	
1.2390	125.4005	15.8701	126.2897	233.9710	
1.4250	126.3005	13.7795	127.1881	235.9634	
1.6100	126.9005	12.2086	127.7854	237.6585	
1.7970	127.4005	10.7893	128.2961	239.1342	
1.9820	128.2005	9.4555	129.1258	240.7719	

STATION 12 Z IS 0.7755

RADIUS	THETA	BETA	THETA SUCTION	THETA PRESSURE
0.8910	134.6005	21.5139	135.6148	240.4355
1.0720	135.9005	18.4893	136.8754	243.3553
1.2520	137.0005	16.1101	137.9545	245.7652
1.4330	137.9005	14.2983	138.8370	247.8988
1.6140	138.5005	12.5958	139.4421	249.4767
1.7960	139.2005	10.8853	140.1777	250.9139
1.9760	140.5005	9.4711	141.5198	252.9689

STATION 13 Z IS 0.8460

RADIUS	THETA	BETA	THETA SUCTION	THETA PRESSURE
0.9130	146.5006	23.0503	147.5119	253.4687
1.0890	147.4006	19.8797	148.3769	255.7994
1.2650	148.3006	17.4129	149.2556	257.9100
1.4410	149.0006	15.1563	149.9602	259.5226
1.6170	149.7006	13.2655	150.6750	261.0539
1.7950	150.9006	11.5727	151.9046	263.0093
1.9710	152.8006	9.5985	153.9006	265.2574

STATION 14 Z IS 0.9165

RADIUS	THETA	BETA	THETA SUCTION	THETA PRESSURE
0.9360	157.3006	23.1248	158.3661	264.5457
1.1070	157.9006	20.4294	158.9142	266.7046
1.2780	158.6006	18.0712	159.5886	268.6025
1.4500	159.4006	15.7706	160.3945	270.2684
1.6210	160.3006	13.8591	161.3093	271.9656
1.7930	161.9006	12.0032	162.9510	274.1992
1.9640	165.0006	9.8421	166.1673	277.5265

STATION 15 Z IS 0.9870

RADIUS	THETA	BETA	THETA SUCTION	THETA PRESSURE
0.9590	167.8006	24.5137	168.8607	275.9413
1.1240	167.9006	21.1719	168.9397	277.1625
1.2910	168.4007	18.7981	169.4146	278.7969
1.4580	169.3007	16.6463	170.3105	280.6065
1.6240	170.4007	14.5308	171.4358	282.3768
1.7920	172.5007	12.2337	173.6114	284.8550
1.9590	176.9007	10.1302	178.1248	289.5310



STATION 16 Z IS 1.0575

RADIUS	THETA	BETA	THETA SUCTION	THETA PRESSURE
0.9820	177.4007	24.4625	178.5120	285.7223
1.1420	177.4007	21.0722	178.5013	286.7095
1.3040	177.7007	18.8128	178.7754	288.1262
1.4660	178.6007	16.7306	179.6715	289.9221
1.6280	180.0007	14.7917	181.0880	292.0637
1.7910	182.9007	12.5925	184.0581	295.3891
1.9530	188.5007	10.4246	189.7796	301.2297

STATION 17 Z IS 1.1280

RADIUS	THETA	BETA	THETA SUCTION	THETA PRESSURE
1.0050	186.8007	25.6606	187.9084	295.8195
1.1600	186.8007	22.2309	187.8991	296.7285
1.3170	186.9007	19.6323	187.9901	297.7317
1.4740	187.8007	17.1737	188.9083	299.3134
1.6320	189.4007	14.7514	190.5607	301.3912
1.7900	193.0007	12.8455	194.2120	305.5557
1.9470	199.8008	10.4561	201.1650	312.4438

STATION 18 Z IS 1.1985

RADIUS	THETA	BETA	THETA SUCTION	THETA PRESSURE
1.0280	195.5008	26.7751	196.6067	305.1161
1.1770	195.5008	23.4587	196.5939	305.9959
1.3300	195.6008	19.8780	196.7333	306.5605
1.4820	196.7008	17.2912	197.8635	308.2434
1.6350	198.8008	14.8826	200.0204	310.7991
1.7890	202.9008	12.9864	204.1748	315.4572
1.9410	211.1008	10.5793	212.5381	323.7215

STATION 19 Z IS 1.2690

RADIUS	THETA	BETA	THETA SUCTION	THETA PRESSURE
1.0510	203.6008	26.7633	204.7466	313.3756
1.1950	203.6008	23.3430	204.7461	314.1304
1.3430	204.1008	20.1383	205.2736	315.1917
1.4910	205.5008	17.7401	206.6945	317.2366
1.6390	208.1008	15.3141	209.3536	320.2705
1.7870	212.7008	13.2544	214.0244	325.3184
1.9350	222.3009	10.9804	223.7722	335.0843

STATION 20 Z IS 1.3395

RADIUS	THETA	BETA	THETA	SUCTION	THETA	PRESSURE
1.0730	211.5008	27.8971	212.6410	321.8016		
1.2120	211.6008	24.7681	212.7282	322.7071		
1.3560	212.4008	21.1310	213.5718	323.9120		
1.4990	214.0008	18.0496	215.2333	325.8492		
1.6420	217.1008	15.7947	218.3816	329.4436		
1.7860	222.3009	13.5335	223.6705	334.9886		
1.9300	233.1009	11.6540	234.5692	346.2012		

STATION 21 Z IS 1.4100

RADIUS	THETA	BETA	THETA	SUCTION	THETA	PRESSURE
1.0960	218.9008	28.7245	220.0448	329.5992		
1.2300	219.0008	25.3562	220.1448	330.3689		
1.3690	220.2009	21.4505	221.4044	331.8497		
1.5070	222.3009	18.5882	223.5552	334.3536		
1.6460	225.8009	16.1040	227.1206	338.2406		
1.7850	231.7009	13.8239	233.1137	344.4656		
1.9240	243.3009	12.1525	244.7886	356.5853		

STATION 22 Z IS 1.4805

RADIUS	THETA	BETA	THETA	SUCTION	THETA	PRESSURE
1.1190	225.9009	30.4224	227.0174	337.2009		
1.2480	226.1009	25.9337	227.2601	337.7135		
1.3820	227.8009	22.3357	229.0055	339.7807		
1.5150	230.3009	18.9378	231.5877	342.4717		
1.6490	234.3009	16.2637	235.6709	346.7569		
1.7840	240.9009	13.9775	242.3692	353.6704		
1.9180	253.1010	12.5624	254.6176	366.5086		

STATION 23 Z IS 1.5510

RADIUS	THETA	BETA	THETA	SUCTION	THETA	PRESSURE
1.1420	232.3009	30.3127	233.4508	343.6960		
1.2650	232.9009	26.7217	234.0661	344.7935		
1.3950	235.0009	22.6755	236.2334	347.1100		
1.5230	238.1009	19.0968	239.4311	350.3113		
1.6530	242.7009	16.4053	244.1207	355.1753		
1.7830	250.0010	14.1421	251.5224	362.7807		
1.9120	262.6010	12.8627	264.1582	376.0690		



STATION 24 Z IS 1.6215

RADIUS	THETA	BETA	THETA	THETA
			SUCTION	PRESSURE
1.1650	238.6009	29.8223	239.7969	349.9883
1.2830	239.4009	27.0522	240.5885	351.4442
1.4070	242.0009	23.4469	243.2387	354.3594
1.5320	245.8010	18.9690	247.1924	357.9484
1.6560	251.0010	16.3834	252.4845	363.4100
1.7810	259.0010	14.3019	260.5760	371.7775
1.9060	271.9010	13.3168	273.4794	385.4995

STATION 25 Z IS 1.6920

RADIUS	THETA	BETA	THETA	THETA
			SUCTION	PRESSURE
1.1880	244.9009	29.3461	246.1429	356.2787
1.3000	245.7009	27.4947	246.9057	357.9078
1.4200	248.7010	24.3835	249.9344	361.3493
1.5400	253.5010	19.1152	254.9348	365.6832
1.6600	259.3010	16.4476	260.8394	371.6944
1.7800	267.9010	14.4755	269.5261	380.6913
1.9000	280.9011	13.5818	282.5216	394.5348

APPENDIX D

INSTRUCTIONS FOR USE OF COMPUTER PROGRAM

Persons interested in an updated FORTRAN listing of the three-dimensional solution discussed in Section 4.3 are advised to contact

Head
Pump Section
Lewis Research Center
National Aeronautics and Space Administration
21000 Brookpark Road
Cleveland 35, Ohio

This listing is not included here since the numerical methods for this solution are incomplete at the writing of this report and further developments are needed.

The present program for the quasi three-dimensional solution discussed in Section 4.2 is written in FULL FORTRAN and a listing is appended, together with a flow diagram (Figure D-1). One tape is required for the input and two for the output. A 10K IBM 7070 was used to obtain the data presented in this report. The assembled program used 8109 locations, 1287 of which were for the FORTRAN system.

The user has the option of running the program dimensionally or non-dimensionally (cf. JDIM below); with or without loss term (cf. LOSS below); and with or without de-bugging information (cf. SENSE SWITCH 3 below).

Running time for an inducer with 25 π stations and 6 annuli was approximately one hour.

Input Statements

There are four READ INPUT TAPE statements. For FORMATS, see the appended FORTRAN listing. Also see table of Input Units.

1. CRT (J,K,L) Co-efficients for polynomials describing channel coordinates and hydraulic diameter. K is the axial station index.

$$L = \begin{cases} 1 & \text{corresponds to } \theta_s \\ 2 & \text{corresponds to } \theta_p \\ 3 & \text{corresponds to } D_h \end{cases}$$



Example: The angle θ_p of the pressure side of the fourth annulus (from the hub) at the eleventh Z - station is given by the sixth degree polynomial:

$$\sum_{J=0}^6 CRT(J, 11, 2) R(4, 11)^J$$

where the radius $R(4, 11)$ is in feet and the angle θ_p is in radians. The hydraulic diameter D_h , in feet, at the same location would be given by

$$\sum_{J=0}^6 CRT(J, 11, 3) R(4, 11)^J$$

If polynomials are available for fewer than 25 Z - stations, these remaining stations must be represented by blank cards (i.e., there must be 105 cards present for this read statement).

2. N Number of Z - stations ($2 \leq N \leq 25$)

NA Number of annuli starting at the hub and counting toward shroud ($3 \leq NA \leq 7$)

NB Number of blades

DEL(I,N) Outlet deviation angle in degrees -- I is annulus number, starting at hub with $I = 1$ - ($I = 1, \dots, NA$)

RH(K) Hub radius ($K = 1, \dots, N$)

RS(K) Shroud radius ($K = 1, \dots, N$)

Z(K) Axial coordinate ($K = 1, \dots, N$)

3. This statement reads an 80-column card on which may appear run identification, date, title, or anything the heart desires. The contents of this card will appear at the top of each set of output data. At the end of a run, the computer program returns to this statement for the data of the next analysis.

4. JDIM If $JDIM = 1$, the program is run dimensionally (with dimensional input) and if $JDIM = 0$, it is run non-dimensionally (with non-dimensional input). For units and formulae to be used with input, see Input Units.

LOSS If $LOSS = 1$, the loss term in the motion equation is calculated. If $LOSS = 0$, no loss term appears in the calculations (cf. FORTRAN Statement 806).

GAMMA	Inlet saturation density
PSAT	Inlet saturation pressure
PI	Inlet static pressure
PT	Inlet total pressure
T	Thermodynamic parameter (cf. Equation 4.1.2-9) Note: To run the program incompressibly, let T = 0 (cf. Equation(4.1.2-8))
EPS	An accuracy criterion, ϵ , on radial equilibrium: iteration continues at an axial station until all annulus pairs at that station satisfy the condition $\left \frac{\partial p}{\partial r} - \frac{\rho}{g_0 r} V_\theta^2 \right \leq \epsilon \frac{\rho_f}{g_0} r_{tip} \Omega^2 \quad (\text{cf. Section 4.2.4})$
VMI	Inlet meridional velocity
RPM	Machine rotative speed
VISC	Fluid viscosity
Q	Inlet volume flow
RTIP	Tip radius at blade leading edge

Note: The actual value of inlet tip radius is read only in the case of a non-dimensional analysis. If the program is to be run dimensionally, the number 1.0 must be entered.

Output Statements

The total number of WRITE OUTPUT TAPE statements depends on the position of SENSE SWITCH 3 and on the value of the index JDIM.

The following statements are put on one output tape:

1. Run identification, etc., which was read in the third READ statement.
2. The following de-bugging information is printed only if SENSE SWITCH 3 is ON:



RESIDUAL A dimensionless number which is the radial equilibrium residual between a pair of adjacent annuli (cf. Section 4.2.4)

DEL R Amount by which the common boundary of a pair of annuli is moved (positive means radially outward)

R Mean radius of the lower of the two annuli

DR Radial height of the lower of the two annuli

R1 Mean radius of the upper of the two annuli

DR1 Radial height of the upper of the two annuli

DPDR Radial pressure gradient between the two annuli

I Annulus number of the lower of the two annuli

K Axial station number at which iteration is being performed

The above information is thus a running account of the way in which iteration proceeds at each Z - station. It may be used for trouble-shooting.

3. **R** Mean radius of annulus

PS Static pressure on suction side of annulus

PP Static pressure on pressure side of annulus

DS Density on suction side of annulus

DP Density on pressure side of annulus

WS Relative velocity on suction side of annulus

WP Relative velocity on pressure side of annulus

I Annulus number

K Axial station number.

The following statements are put on the second output tape:

4. Same as first WRITE statement.

5. R Mean radius of annulus
 - PB Static pressure at middle of annulus
 - DB Fluid density at middle of annulus
 - WB Relative velocity at middle of annulus
 - VM Meridional velocity at middle of annulus
 - VT Tangential absolute velocity at middle of annulus
 - DPBB Static pressure difference between pressure and suction sides of annulus (blade loading)
 - I Annulus number
 - K Axial station number
6. RPM Rotative speed of machine
 - GPM Fluid volume flow at inlet, Q_1
 - S POWER Shaft power, P_S
 - H POWER Hydraulic power P_H
 - AVE PRESS Mass averaged static pressure at outlet
 - HD RISE Mass averaged head rise, H_{ave}
 - EFF Machine efficiency, η

For details, see Section 4.2.2.
7. If JDIM = 0, non-dimensionalized values of the output in the sixth WRITE statement will be printed. Otherwise this statement is omitted.
8. Hub-to-tip axial velocity components at outlet (starting with annulus closest to hub)
9. Hub-to-tip total pressure distribution at outlet (starting with annulus closest to hub)



Internal Units of Program

If JDIM = 1 (dimensional run), the working units of the program (not the input or output units) are as follows:

All distances in feet

All velocities in ft/sec

All pressures in lbf/ft²

T (thermodynamic parameter) in ft²/lbf

All densities in slugs/ft³

These are the units used in the second, third, and fifth WRITE statements. If JDIM = 0, all calculations are performed non-dimensionally.

Input Units

The units and/or formulae for preparing input to the program are summarized in the following table:

FORTRAN SYMBOL	ANALYSIS SYMBOL	UNITS	NON-DIMENSIONAL FORMULA (IF ANY)
DEL	δ	degrees	δ
RH	r_h	inches	$\hat{r}_h = r_h / r_{i,t}$
RS	r_t	inches	$\hat{r}_t = r_t / r_{i,t}$
Z	z	inches	$\hat{z} = z / r_{i,t}$
GAMMA	Γ	lbm/ft ³	$\hat{\Gamma} = \frac{\Gamma}{\rho_f U_{i,t}^2} = \frac{1}{2} \tau$
PSAT	p_{sat}	lbf/in ²	$\hat{p}_{sat} = \frac{p_{sat} - p_i}{\rho_f U_{i,t}^2} = \frac{1}{2} \phi^2$
PI	p_i	lbf/in ²	$\hat{p}_i = 0$
PT	p_i	lbf/in ²	$\hat{p}_i = 0$
T	\mathcal{T}	in ² /lbf	$\hat{\mathcal{T}} = \mathcal{T} \frac{\rho_f U_{i,t}^2}{g_o} = \Theta$



2. IN COMPRESSIBLE LOOP $I = 3$ $K = 2$
TO CONTINUE HIT START

This message will appear if the program has cycled through the compressibility loop for a given annulus, within a given radial equilibrium iteration, 100 times without having converged on a mean density. The machine will halt. Upon pressing the START button the program will accept all values currently in storage for station K and proceed to $(K + 1)$ in the normal fashion.

3. IN LOOP $I = 3$ $K = 2$
TO CONTINUE HIT START

This message will appear if the program has made 150 cycles through the radial equilibrium loop for a given axial station without reaching convergence (see Section 4.2.4). The machine will halt. Upon pressing the START button, the program will accept all values currently in storage for station K and proceed to $(K + 1)$ in the normal fashion.

The program normally ends with an input tape END OF FILE condition.

FORTRAN SYMBOL	ANALYSIS SYMBOL	UNITS	NON-DIMENSIONAL FORMULA (IF ANY)
EPS	ϵ	--	--
VM1	$V_{m,1}$	ft/sec	$\hat{V}_{m,1} = V_{m,1} / U_{1,t} = \phi$
RPM	Ω	rev/min	Ω
VISC	ν	ft ² /sec	$\hat{\nu} = \nu / (U_{1,t} r_{1,t}) = 1/Re$
Q	Q	gal/min	$\hat{Q} = Q / (U_{1,t} r_{1,t}^2)$
RTIP	$r_{1,t}$	inches	$r_{1,t}$

Output Units

In the dimensional output (sixth WRITE statement) the following units are used:

rotative speed	rev/min
volume flow	gal/min
powers	horsepower
pressure	lbf/in ²
head rise	ft-lbf/lbm

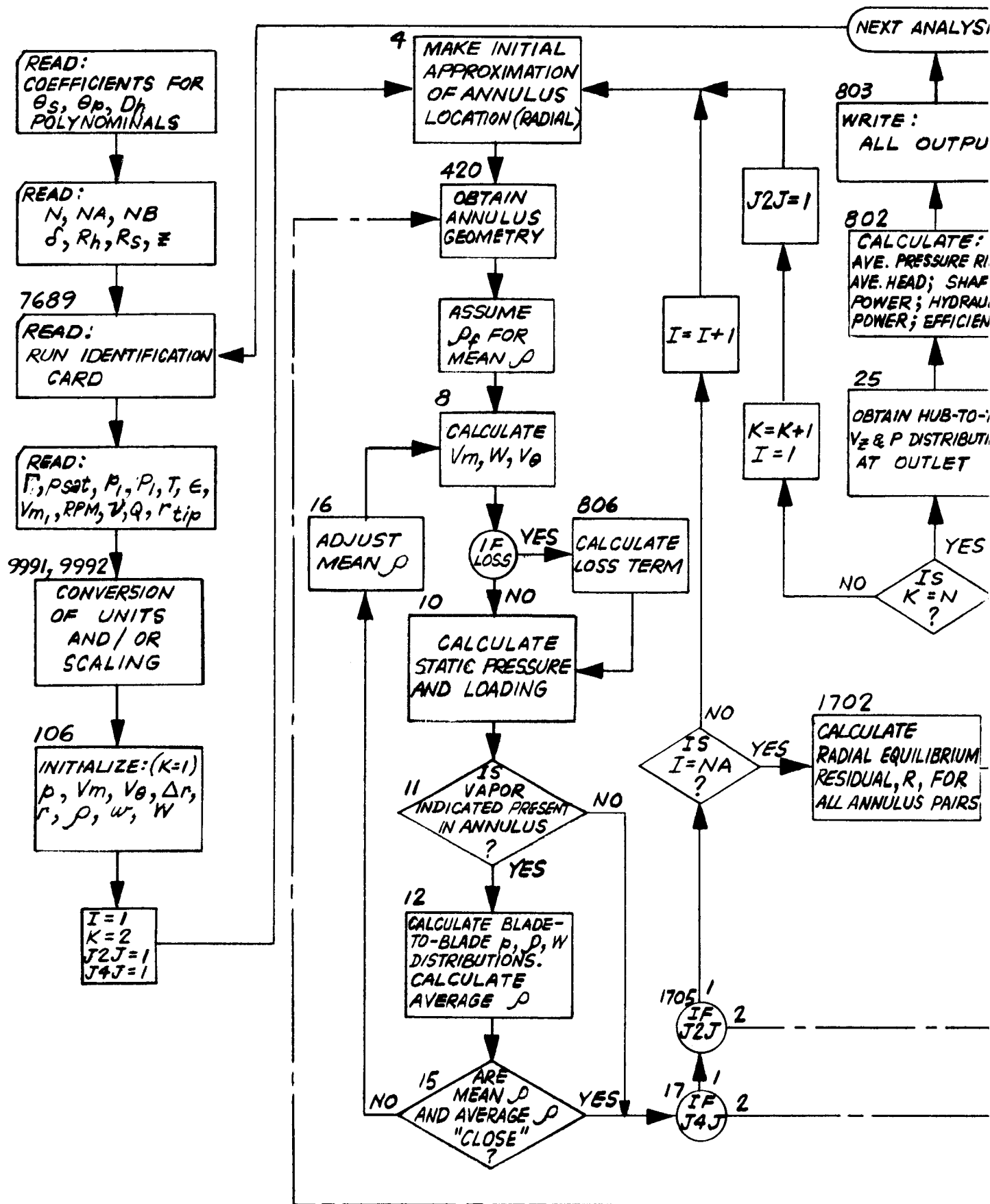
Non-dimensional values of these outputs are calculated as shown by the formulae in Section 4.2.2.

Console Messages

Three messages, which might appear on the console typewriter, are as follows:

1. NEGATIVE LOADING I = 3 K = 2

This message will appear if a situation exists in annulus 3 at station 2 (numbers are illustrative only) similar to the one discussed in Section 4.5.3. This is a situation which the present compressibility iteration loop cannot handle. The computer will stop calculations and proceed directly to FORTRAN statement 25, the output routine.



COMPILE RUN FORTRAN 00180066

NASA ADVANCED INDUCER STUDY - BASICALLY AXIAL FLOW 5/15/63

ER 5288 APPENDIX D

TAPCO DIVISION

THOMPSON RAMO WOOLDRIDGE, INC.

QUASI 3 DIMENSIONAL INDUCER ANALYSIS

DIMENSION RES6,25,DEL87,25,DM87,25,8887,25,BF87,25, 00280066

1 PB87,25,0087,25,VM87,25,VI87,25,W87,25,DL87,25,DP8887,25, 00480066

2 ,PS87,25,PP87,25,OS87,25,DP87,25,WS87,25,WP87,25,P851, 00580066

3 D851,WS87,FM87,25,RH87,25,RS87,25,Z87,25,DR87,25,CF87, 00680066

4 CRT87,25,FG87,25,SM87,25,VZ87,25,PTD87, 00780066

EQUIVALENCE 8PWERS, SM87,25, 8PWERH,SM87,25, 00880066

TANF87,25,SINF87,25,COSF87,25, 00980066

PI # 3.1415927 01080066

TPI # 6.2831853 01180066

READ INPUT TAPE 2, 1002, CRT 01280066

READ INPUT TAPE 2,1003,N,NA,NB,ZDEL87,25,I#1,NA,8RH87,25,K#1,NA, 01380066

1 8RS87,25,K#1,NA,8Z87,25,K#1,NA 01480066

ZNA # NA 01580066

ZN # N 01680066

ENB # NB 01780066

NM1 # N-1 01880066

NA1 # NA-1 01980066

DO 1 K # 1, NM1 02080066

TEMP1 # K 02180066

TEMP1 # 8TEMP1 / ZNA ** 6.0 02280066

DO 1 I # 1, NA 02380066

DEL87,25,DEL87,25, 0174533 02480066

DEL87,25,DEL87,25, 02580066

7689 READ INPUT TAPE 2, 1000 02680066

TYPE 1000 02780066

WRITE OUTPUT TAPE 12,1006 02880066

WRITE OUTPUT TAPE 12, 1000 02980066

WRITE OUTPUT TAPE 13,1006 03080066

IF 8SENSE SWITCH 3d 770, 775 03180066

770 WRITE OUTPUT TAPE 12, 1028 03280066

775 WRITE OUTPUT TAPE 13, 1000 03380066

READ INPUT TAPE 2,1001,JDIM,LOSS,GAMMA,PSAT,PI,PT,Y,EPS,VM1, 03480066

1 RPM,VISC,Q,RTIP 03580066

IF 8JDIM 9991,9992,9991

C



C INITIALIZATION FOR DIMENSIONAL INPUT

C
9991 QM#RPM*IPI/60. 03680066
Q # Q / 449. 03780066
PI # PI * 144. 03880066
PT # PT * 144. 03980066
PSAT # PSAT * 144. 04080066
DSAT # GAMMA / 32.2 04180066
DO 101 K # 1. N 04280066
RH%K # RH%K # 12. 04380066
RS%K # RS%K # 12. 04480066
Z%K # Z%K # 12. 04580066
101 GO TO 103 04680066

C INITIALIZATION FOR DIMENSIONLESS INPUT

C
9992 QM # 1. 04780066
DSAT # 1. 04880066
RTIP # RTIP / 12. 04980066
103 TWONU # 2.0 * VISC 05080066
PRISE # DSAT * RS * QM**2 05180066
IF%TD 105,104,105 05280066
104 NS # 3 05380066
GO TO 106 05480066
105 NS # 51 05580066
106 ZNS # NS 05680066
DO 3 I # 1,NA 05780066
PB%I,1 # PI 05880066
VM%I,1 # VM1 05980066
VT%I,1 # 0.0 06080066
OR%I,1 # %RS -RH% / ZNA 06180066
ZI # I 06280066
R%I,1 # DR%I,1 # %ZI -.5% &RH 06380066
TEMP1 # PSAT - PB%I,1 06480066
IF%TEMP1 1005, 1005, 2 06580066
1005 DB%I,1 # DSAT 06680066
GO TO 2005 06780066
2 DB%I,1 # DSAT / %I.0 & T * TEMP1 06880066
2005 FM%I,1 # DB%I,1 * IPI * R%I,1 # DR%I,1 # VM%I,1 06980066
3 WB%I,1 # %VM%I,1**2 &OM* R%I,1 - VI%I,1**2 # **.5 07080066
K # 1 07180066

C BEGIN MAIN CALCULATIONS

C

3999	K # K&I		07280066
	J4J # 1		07380066
	JCNT # 0		07480066
	TEMP1 # ZRSZKA-RH&KKA / ZRSZKA-10 -RH&K-100		07580066
	TEMP2 # ZRSZK&10 - RH&K&100 / Z RS&KA - RH&KKA		07680066
	DZSQ # Z&ZKA - Z&K-100 **2		07780066
	SUM1 # 0.0		07880066
	I # 1		07980066
4	R&I,Ka # RH&KA &Z&Z&I,K-10 - RH&K-100 * TEMP1		08080066
	IM1 # I-1		08180066
	IF&IM104001,4002 , 4001		08280066
4001	SUM1 # SUM1 & DR &I-1,Ka		08380066
4002	OR&I,Ka # 2.0 * Z R&I,Ka -RH&KA - SUM10		08480066
	J2J # 1		08580066
420	IF &K-Na 4003,4201,4003		08680066
4003	R&I,K&10 # RH&K&10 & ZR&I,Ka- RH&KKA * TEMP2		08780066
4201	DO 430 L # 1,3		08880066
	IF&L -30 421, 4291, 421		08980066
421	DO 429 J4 #1,3		09080066
	K1# K & J4 -2		09180066
	ASSIGN 422 TO J3J		09280066
	GO TO 423		09380066
422	FG&J4,L0 # Y		09480066
	GO TO 429		09580066
423	DO 424 J3 # 1,7		09680066
424	CF&J30 # CRT&J3,K1,L0		09780066
	X # R&I,K10 * RTIP		09880066
	Y # CF&X*CF&Z20&X*CF&Z30&X*CF&Z40&X*CF&Z50&X*CF&Z60&X*CF&Z70000000		09980066
	GO TO J3J,422 , 42920		10080066
429	CONTINUE		10180066
	GO TO 430		10280066
4291	K1 # K		10380066
	ASSIGN 4292 TO J3J		10480066
	GO TO 423		10580066
4292	DH # Y / RTIP		10680066
430	CONTINUE		10780066
	TEMP4 # FG&2,20 - FG&2,10		10880066
	TEMP5 # FG&1,10 & FG&1,20		10980066
	TEMP3 # FG&3,10 & FG&3,20 - TEMP5		11080066
	TEMP5 # 30.5 * ZFG&2,10 &FG&2,20 -TEMP500 **2		11180066
	IF &K -Na 5,5001,5		11280066
5	DM&I,Ka # Z&Z&K&10- Z&K-100**2 & ZR&I,K&10-R&I,K-100**20**5		11380066
	BB&I,Ka # ATANF& 2.0 * DM&I,Ka / ZR&I,Ka * TEMP300		11480066
	OZOM # Z&Z&K&10-Z&K-100 / DM&I,Ka		11580066



```
GO TO 5002
5001  OM%I,K% # %Z%K% - Z%K-l%*2 & %R%I,K% -R%I,K-l%*2%*0.5 11680066
      8B%I,K% # ATANF%2.* DM%I,K% / %R%I,K%&R%I,K-l%* %TEMP5%*0.5 % 11780066
      OZDM # %Z%K% -Z%K-l% / DM%I,K% 11880066
5002  8F%I,K% # 8B%I,K% - DEL%I,K% 11980066
      0B%I,K% # DSAT 12080066
      J6J # 1 12180066
      KOMPR # 0 12280066
      12380066

C
C BEGIN ANNULUS FLOW CALCULATIONS
C
8  VM%I,K% # FM%I / %OB%I,K% * TEMP4 * R%I,K% * DR%I,K%*ENB *OZDM% 12480066
    HOB # 0B%I,K% 12580066
    WB%I,K% # VM%I,K% / SIN% %B%I,K% 12680066
    VT%I,K% # OM * R%I,K% - VM%I,K% / TAN% %B%I,K% 12780066
    IF%I 8021,806,8021 12880066
    IF%VT%I,K% 8041,806,806 12980066
    8041 TYPE 1008,I,K 13080066
        GO TO 23 13180066
    806 IF%LOSS% 9,9001,9 13280066
    9001 DL%I,K% # 0.0 13380066
        GO TO 10 13480066

C
C BEGIN LOSS CALCULATION
C
9  DLAM # %DZSQ & %R%I,K%-R%I,K-l%*2&%*2&%*2&%*2&%*2&%*2&%*2&%*2&%*2 13580066
    1 * TEMP5%*0.5 13680066
    RE # %WB%I,K% & WB%I,K-l%* DM / TWONU 13780066
    F # .00714 & .6104 / RE ** .35 13830066
    TEMP7 # WB%I,K-l% - WB%I,K% 13980066
9002  DL%I,K% # F * DLAM / %4.0* DH% * %WB%I,K-l%*2&%WB%I,K%*2% 14080066
    IF%TEMP7% 10, 10, 9003 14180066
9003  G # TEMP7 / %2.0 * DLAM% % Q/%ENB*PI *%0.5 * %WB%I,K-l% & 14280066
    1 WB%I,K%*%*3.%*0.5 14380066
    DL%I,K% # DL%I,K% -%WB%I,K%*2-WB%I,K-l%*2%* G / % 14480066
    1 2.6666667 & 2.0 * G% 14580066

C
C END LOSS CALCULATION
C
10  A # WB%I,K%*2 - WB%I,K-l%*2 & OM*2 *%R%I,K%-l%*2 -R%I,K%*2% 14680066
    1 & 2.0 * DL%I,K% 14780066
    PB%I,K% # PB%I,K-l% - A * %DB%I,K%& OB%I,K-l%*0.25 14880066
    OPB%I,K% # TEMP4 *OB%I,K%* VM%I,K% *%R%I,K%*%VT%I,K%-R%I,K-l%* %14980066
    1 VT%I,K-l% / %DZSQ &%R%I,K%-R%I,K-l%*2%*0.5 % 15080066
```

11 ASSIGN 15 TO J5J 15180066
GO TO 11, 12, 13, 14, 15, 16, 17, 18, 19, 20, 21, 22, 23, 24, 25, 26, 27, 28, 29, 30, 31, 32, 33, 34, 35, 36, 37, 38, 39, 40, 41, 42, 43, 44, 45, 46, 47, 48, 49, 50, 51, 52, 53, 54, 55, 56, 57, 58, 59, 60, 61, 62, 63, 64, 65, 66, 67, 68, 69, 70, 71, 72, 73, 74, 75, 76, 77, 78, 79, 80, 81, 82, 83, 84, 85, 86, 87, 88, 89, 90, 91, 92, 93, 94, 95, 96, 97, 98, 99, 100, 101, 102, 103, 104, 105, 106, 107, 108, 109, 110, 111, 112, 113, 114, 115, 116, 117, 118, 119, 120, 121, 122, 123, 124, 125, 126, 127, 128, 129, 130, 131, 132, 133, 134, 135, 136, 137, 138, 139, 140, 141, 142, 143, 144, 145, 146, 147, 148, 149, 150, 151, 152, 153, 154, 155, 156, 157, 158, 159, 160, 161, 162, 163, 164, 165, 166, 167, 168, 169, 170, 171, 172, 173, 174, 175, 176, 177, 178, 179, 180, 181, 182, 183, 184, 185, 186, 187, 188, 189, 190, 191, 192, 193, 194, 195, 196, 197, 198, 199, 200, 201, 202, 203, 204, 205, 206, 207, 208, 209, 210, 211, 212, 213, 214, 215, 216, 217, 218, 219, 220, 221, 222, 223, 224, 225, 226, 227, 228, 229, 230, 231, 232, 233, 234, 235, 236, 237, 238, 239, 240, 241, 242, 243, 244, 245, 246, 247, 248, 249, 250, 251, 252, 253, 254, 255, 256, 257, 258, 259, 260, 261, 262, 263, 264, 265, 266, 267, 268, 269, 270, 271, 272, 273, 274, 275, 276, 277, 278, 279, 280, 281, 282, 283, 284, 285, 286, 287, 288, 289, 290, 291, 292, 293, 294, 295, 296, 297, 298, 299, 300, 301, 302, 303, 304, 305, 306, 307, 308, 309, 310, 311, 312, 313, 314, 315, 316, 317, 318, 319, 320, 321, 322, 323, 324, 325, 326, 327, 328, 329, 330, 331, 332, 333, 334, 335, 336, 337, 338, 339, 340, 341, 342, 343, 344, 345, 346, 347, 348, 349, 350, 351, 352, 353, 354, 355, 356, 357, 358, 359, 360, 361, 362, 363, 364, 365, 366, 367, 368, 369, 370, 371, 372, 373, 374, 375, 376, 377, 378, 379, 380, 381, 382, 383, 384, 385, 386, 387, 388, 389, 390, 391, 392, 393, 394, 395, 396, 397, 398, 399, 400, 401, 402, 403, 404, 405, 406, 407, 408, 409, 410, 411, 412, 413, 414, 415, 416, 417, 418, 419, 420, 421, 422, 423, 424, 425, 426, 427, 428, 429, 430, 431, 432, 433, 434, 435, 436, 437, 438, 439, 440, 441, 442, 443, 444, 445, 446, 447, 448, 449, 450, 451, 452, 453, 454, 455, 456, 457, 458, 459, 460, 461, 462, 463, 464, 465, 466, 467, 468, 469, 470, 471, 472, 473, 474, 475, 476, 477, 478, 479, 480, 481, 482, 483, 484, 485, 486, 487, 488, 489, 490, 491, 492, 493, 494, 495, 496, 497, 498, 499, 500, 501, 502, 503, 504, 505, 506, 507, 508, 509, 510, 511, 512, 513, 514, 515, 516, 517, 518, 519, 520, 521, 522, 523, 524, 525, 526, 527, 528, 529, 530, 531, 532, 533, 534, 535, 536, 537, 538, 539, 540, 541, 542, 543, 544, 545, 546, 547, 548, 549, 550, 551, 552, 553, 554, 555, 556, 557, 558, 559, 560, 561, 562, 563, 564, 565, 566, 567, 568, 569, 570, 571, 572, 573, 574, 575, 576, 577, 578, 579, 580, 581, 582, 583, 584, 585, 586, 587, 588, 589, 590, 591, 592, 593, 594, 595, 596, 597, 598, 599, 600, 601, 602, 603, 604, 605, 606, 607, 608, 609, 610, 611, 612, 613, 614, 615, 616, 617, 618, 619, 620, 621, 622, 623, 624, 625, 626, 627, 628, 629, 630, 631, 632, 633, 634, 635, 636, 637, 638, 639, 640, 641, 642, 643, 644, 645, 646, 647, 648, 649, 650, 651, 652, 653, 654, 655, 656, 657, 658, 659, 660, 661, 662, 663, 664, 665, 666, 667, 668, 669, 670, 671, 672, 673, 674, 675, 676, 677, 678, 679, 680, 681, 682, 683, 684, 685, 686, 687, 688, 689, 690, 691, 692, 693, 694, 695, 696, 697, 698, 699, 700, 701, 702, 703, 704, 705, 706, 707, 708, 709, 710, 711, 712, 713, 714, 715, 716, 717, 718, 719, 720, 721, 722, 723, 724, 725, 726, 727, 728, 729, 730, 731, 732, 733, 734, 735, 736, 737, 738, 739, 740, 741, 742, 743, 744, 745, 746, 747, 748, 749, 750, 751, 752, 753, 754, 755, 756, 757, 758, 759, 760, 761, 762, 763, 764, 765, 766, 767, 768, 769, 770, 771, 772, 773, 774, 775, 776, 777, 778, 779, 780, 781, 782, 783, 784, 785, 786, 787, 788, 789, 790, 791, 792, 793, 794, 795, 796, 797, 798, 799, 800, 801, 802, 803, 804, 805, 806, 807, 808, 809, 810, 811, 812, 813, 814, 815, 816, 817, 818, 819, 820, 821, 822, 823, 824, 825, 826, 827, 828, 829, 830, 831, 832, 833, 834, 835, 836, 837, 838, 839, 840, 841, 842, 843, 844, 845, 846, 847, 848, 849, 850, 851, 852, 853, 854, 855, 856, 857, 858, 859, 860, 861, 862, 863, 864, 865, 866, 867, 868, 869, 870, 871, 872, 873, 874, 875, 876, 877, 878, 879, 880, 881, 882, 883, 884, 885, 886, 887, 888, 889, 890, 891, 892, 893, 894, 895, 896, 897, 898, 899, 900, 901, 902, 903, 904, 905, 906, 907, 908, 909, 910, 911, 912, 913, 914, 915, 916, 917, 918, 919, 920, 921, 922, 923, 924, 925, 926, 927, 928, 929, 930, 931, 932, 933, 934, 935, 936, 937, 938, 939, 940, 941, 942, 943, 944, 945, 946, 947, 948, 949, 950, 951, 952, 953, 954, 955, 956, 957, 958, 959, 960, 961, 962, 963, 964, 965, 966, 967, 968, 969, 970, 971, 972, 973, 974, 975, 976, 977, 978, 979, 980, 981, 982, 983, 984, 985, 986, 987, 988, 989, 990, 991, 992, 993, 994, 995, 996, 997, 998, 999, 1000

12 CALCULATE BLADE TO BLADE DISTRIBUTIONS

12 DO 13 J # 1, NS 15480066
ZJ # J # 2 -1 15580066
P%J # P%I, K# 5 * DPBB%I, K# *ZJ/ZNS -1.0# 15680066
TEMP7 # PSAT - P%J#

1201 IF%TEMP7# 1201, 1201, 1202 15780066
D%J# # DSAT 15880066
GO TO 13 15980066

1202 D%J# # DSAT / %1.0 & T * TEMP7# 16080066
13 CONTINUE 16180066
JMID # %NS%I# / 2 16280066
W%JMID# # W%I, K# 16380066
SUM2 # D%JMID# 16480066
J1 # JMID%I 16580066
DO 14 JUP#J1, NS 16680066
JDN# JMID - JUP%JMID 16780066
J # JDN 16880066
JJ1 # JDN & 1 16980066
JJ1 # JDN & 1 17080066
ASSIGN 1401 TO J1J 17180066
GO TO 1402 17280066
J1 # JUP 17380066
JJ1 # JUP - 1 17480066
ASSIGN 14 TO J1J 17580066
TEMP7 # W%J1J# **2 &4. *P%J1J# - P%J# #/ 17680066
1 2D%J1J# & D%J# # 17780066
IF%TEMP7# 1403, 1403, 1404 17880066
1403 W%J# # 0.0 17980066
GO TO 1405 18080066
1404 W%J# # TEMP7 **5 18180066
1405 SUM2 # SUM2 & D%J# 18280066
GO TO J1J, 1401, 14# 18380066
14 CONTINUE 18480066
GO TO J5J, 12307, 15# 18580066
15 DEN # SUM2 / ZNS 18680066
C
C
C

16 COMPRESSIBLE LOOP TEST

16 IF%DEN - DB%I, K# 16, 163, 163 18780066
DB%I, K# # .98 * DB%I, K# 18880066



J6J # 2
KOMPR # KOMPR & I
IF # KOMPR -1000 8, 8, 9995
163 DBZ1,Ka # 0.5 * ZDBZ1,Ka & HD80
GO TO 17
9995 TYPE 1050, I, K
PAUSE 12345
GO TO 23
18980066
19080066
19180066
19280066
19380066
19480066
19580066
19680066

C
C
END ANNULUS FLOW CALCULATION

17 GO TO #1705,17060, J4J
1706 IFZ1-IMAX-10 1707,1708,1708
1707 I # 101
GO TO 420
1708 I # 1 -1
J1 # I
J2 # I
GO TO 1704
1705 GO TO #1703,220010, J2J
1703 IFZ1 -NA0 1701, 1702, 1702
1701 I # 1 01
GO TO 4
19780066
19880066
19980066
20080066
20180066
20280066
20380066
20480066
20580066
20680066
20780066
20880066

C
C
END MAIN CALCULATIONS

1702 J1 # 1
J2 # NA -1
1704 DO 19 I # J1,J2
DPDR # ZPBZ101,Ka - PBZ1,Ka/ZRZ101,Ka - RZ1,Ka0
DVSQ # .5 * Z08Z101,Ka*V1Z101,Ka**2/RZ101,Ka & DBZ1,Ka*V1Z1,Ka**2/21380066
1RZ1,Ka0
20980066
21080066
21180066
21280066
21380066
21480066

C
C
RADIAL EQUILIBRIUM CHECK

19 RESZ1,Ka # ZDPDR - DVSQ0/PRISE
GO TO #1903,20000, J4J
1903 ACC # 0.0
DO 1902 I # 1,NA1
IFZABSFZRESZ1,Ka0-ACC01902,1902,1901
1901 IMAX # I
ACC # ABSFZRESZ1,Ka0
1902 CONTINUE
I # IMAX
21580066
21680066
21780066
21880066
21980066
22080066
22180066
22280066
22380066

1905	IF\$ACC - EPS	23 , 23 , 2000	22480066
2000	GO TO 2001, 2002, J4J		22580066
2001	J4J # 2		22680066
	RHLD # R\$1, Ka		22780066
	RESH # RES\$1, Ka		22880066
	IF\$DR\$1, Ka - DR\$1, Ka 20013, 20016, 20016		22980066
20013	DDR # .02 * DR\$1, Ka		23080066
	GO TO 20019		23180066
20016	DDR # .02 * DR\$1, Ka		23280066
20019	R\$1, Ka # R\$1, Ka & DDR		23380066
	R\$1, Ka # R\$1, Ka & DDR		23480066
	DR\$1, Ka # DR\$1, Ka - 2 * DDR		23580066
	DR\$1, Ka # DR\$1, Ka & 2 * DDR		23680066
	GO TO 420		23780066
2002	J4J # 1		23800066
C			
C			
C			
	CALCULATE REQUIRED RADIAL ADJUSTMENT		
	DELR # -RES\$1, Ka * R\$1, Ka - RHLD / RES\$1, Ka - RESH		23980066
	JCNT # JCNT &1		24080066
	IF\$JCNT - 1500 2102 , 2102 , 10010		24180066
10010	TYPE 1004 , 1, K		24280066
	PAUSE 12345		24380066
	GO TO 23		24480066
2102	R\$1, Ka # R\$1, Ka & DELR		24580066
	R\$1, Ka # R\$1, Ka & DELR		24680066
	TEMP7 # 2.0 * DELR		24780066
	DR\$1, Ka # DR\$1, Ka & TEMP7		24880066
	DR\$1, Ka # DR\$1, Ka - TEMP7		24980066
	IF\$DR\$1, Ka 2105, 2105, 2108		25080066
2105	R\$1, Ka # R\$1, Ka - DELR		25180066
	R\$1, Ka # R\$1, Ka - DELR		25280066
	DR\$1, Ka # DR\$1, Ka - TEMP7		25380066
	DR\$1, Ka # DR\$1, Ka & TEMP7		25480066
	DELR # .5 * DELR		25580066
	GO TO 2102		25680066
2108	IF\$DR\$1, Ka 2105, 2105, 2109		25780066
2109	IF\$SENSE SWITCH 30 2190, 2200		25880066
2190	WRITE OUTPUT TAPE12, 1022, RES\$1, Ka, DELR , R\$1, Ka, DR\$1, Ka, R\$1, Ka		25980066
	1, Ka, DR\$1, Ka , DPOR, 1, K		26080066
2200	JMAX # 1 &1		26180066
	J2J # 2		26280066
	IF\$1 -10 22003, 420 , 22003		26380066
22003	I # 1-1		26480066



GO TO 420
22001 I #1 &1 26580066
IF#1 - JMAX# 420 , 420 , 22004 26680066
22004 I # JMAX -1 26780066
2202 IF#1-1# 2204,2203 , 2204 26880066
2203 J1 # 1 26980066
J2 # 2 27080066
GO TO 1704 27180066
2204 IF#1-NA&1# 2206 , 2205 , 2206 27280066
2205 J1 # NA-2 27380066
J2 # NA-1 27480066
GO TO 1704 27580066
2206 J1 # I -1 27680066
J2 # I &1 27780066
GO TO 1704 27880066
27980066

C

C CALCULATE DISTRIBUTIONS ON BLADES

C

I # 1 28080066
23001 PS#1,K# # PB#1,K# - DPBB#1,K# * 0.5 28180066
PP#1,K# # PS#1,K# & DPBB#1,K# 28280066
TEMP7 # PSAT - PS#1,K# 28380066
IF#TEMP7# 2301 , 2301 , 2302 28480066
DS#1,K# # DSAT 28580066
GO TO 2303 28680066
2302 DS#1,K# # DSAT / #1. & T * TEMP7# 28780066
2303 TEMP7 # PSAT - PP#1,K# 28880066
IF#TEMP7# 2304 , 2304 , 2305 28980066
2304 DP#1,K# # DSAT 29080066
GO TO 2306 29180066
2305 DP#1,K# # DSAT / #1. & T * TEMP7# 29280066
2306 ASSIGN 2307 TO J5J 29380066
IF#ABSF#DPBB#1,K# - 2. * #PB#1,K# - PSAT#2309,2309,12 29480066
2309 TEMP6 # WB#1,K#**2 & 2. * #PB#1,K# - PS#1,K#/DSAT 29580066
IF #TEMP6# 2311, 2311, 2313 29680066
2311 WS#1,K# # 0.0 29780066
GO TO 2315 29880066
2313 WS#1,K# # TEMP6**0.5 29980066
2315 TEMP6 # WB#1,K#**2 & 2. * #PB#1,K# - PP#1,K#/ DSAT 30080066
IF #TEMP6# 2317, 2317, 2319 30180066
2317 WP#1,K# # 0.0 30280066
GO TO 2399 30380066
2319 WP#1,K# # TEMP6**0.5 30480066
GO TO 2399 30580066

2307	TEMP6 # W**2 & 4.**P - PS%I,Kaa/%D & DS%I,Kaa	30680066
	IF %TEMP6a 2321, 2321, 2323	30780066
2321	WS%I,Ka # 0.0	30880066
	GO TO 2325	30980066
2323	WS%I,Ka # TEMP6**5	31080066
2325	TEMP6 # W%NSa**2 & 4.** %P%NSa - PP%I,Kaa / %D%NSa & DP%I,Kaa	31180066
	IF %TEMP6a 2327, 2327, 2329	31280066
2327	WP%I,Ka # 0.0	31380066
	GO TO 2399	31480066
2329	WP%I,Ka # TEMP6**5	31580066
2399	I # 1&1	31680066
	IF%I - NAa23001,23001, 24	31780066
24	IF%K-NA 3999, 25, 25	31880066
C		
C	CALCULATE FINAL OUTPUTS	
C		
25	DO 801 J3 #1,4	31980066
801	SM %J3a # 0.0	32080066
	DO 802 I # 1,NA	32180066
	VZ%Ia # VM%I,Na * %Z%Na-2%N-1a/DM%I,Na	32280066
	PTD%Ia # PB%I,Na&.5*%VT%I,Na**2&VM%I,Na**2a*DSAT	32380066
	SM # SM & FM%Ia	32480066
	SM%2a # SM%2a & FM%Ia * PB%I,Na	32580066
	SM%3a # SM%3a & FM%Ia * %P%TD%Ia-PTa / DSATa	32680066
802	SM%4a # SM%4a & FM%Ia * R%I,Na * VT%I,Na	32780066
	PAVE # SM%2a / %SM * 144. a	32880066
	HAVE # SM%3a / %SM * 32.2a	32980066
	PWERS # OM * PWERS / 550.	33080066
	PWERH # SM%3a / 550.	33180066
	EFF # PWERH / PWERS	33280066
803	DO 804 I # 1,NA	33380066
	WRITE OUTPUT TAPE 12, 1020	33480066
	WRITE OUTPUT TAPE 13, 1021	33580066
	WRITE OUTPUT TAPE 12, 1022, %R%I,Ka, PS%I,Ka, PP%I,Ka, DS%I,Ka,	33680066
	1 DP%I,Ka, WS%I,Ka, WP%I,Ka, I, K, K # 2, Na	33780066
804	WRITE OUTPUT TAPE 13, 1022, %R%I,Ka, PB%I,Ka, DB%I,Ka, WB%I,Ka,	33880066
	1 VM%I,Ka, VT%I,Ka, OP88%I,Ka, I, K, K # 1, Na	33980066
	IF%JDIMA 1023, 1030, 1023	34080066
1023	WRITE OUTPUT TAPE 13, 1025, RPM, GPM, PWERS, PWERH, PAVE, HAVE, EFF	34180066
	GO TO 1035	34280066
1030	CRPM # RPM * PI / 30.	34380066
	CGAM # GAMMA / 32.2	34480066
	GPM # Q * CRPM * RTIP**3.** 449.	34580066
	SPD # PWERS * CGAM * CRPM**3.* RTIP**5.	34680066



HPD # EFF * SPD 34780066
PAVED # PAVE * CGAM * %CRPM * RTIP**2 34880066
HAVED # HAVE * %CRPM * RTIP**2 34980066
WRITE OUTPUT TAPE 13, 1025, RPM,GPM,SPD,HPD,PAVED,HAVED,EFF 35080066
PWERS # PWERS * 550. 35180066
PWERH # PWERH * 550. 35280066
PAVE # PAVE * 144. 35380066
HAVE # HAVE * 32.2 35480066
WRITE OUTPUT TAPE 13,1027, OM,Q, PWERS,PWERH,PAVE,HAVE,EFF 35580066
1035 WRITE OUTPUT TAPE13,1029,%VZ%I,I#1,NAQ 35680066
WRITE OUTPUT TAPE13,10291,%PID%I,I#1,NAQ 35780066
GO TO 7689 35880066

C

FORMATS

C

C

1002 FORMAT% 5E15.8Q 35980066
1003 FORMAT%3I10,5F10.4/%8F10.4Q 36080066
1000 FORMAT%80H 36180066
1 36280066
1006 FORMAT%//Q 36380066
1028 FORMAT%/7X8HRESIDUAL11X4HDELRI4X1HRI3X2HORI3X2HRI11X10HDPD36480066
1R I KQ 36580066
1001 FORMAT%2I10,6F10.4/%8F10.4Q 36680066
1008 FORMAT%19HNEGATIVE LOADING I#12,4H K#12Q 36780066
1050 FORMAT%23HIN COMPRESSIBLE LOOP I#14,4H K#14,21HTO CONTINUE HIT ST36880066
1ARIQ 36980066
1004 FORMAT%10HIN LOOP I#14,4H K#14,21HTO CONTINUE HIT STARTQ 37080066
1022 FORMAT%7E15.8,213Q 37180066
1020 FORMAT%/14X1HRI3X2HPSI3X2HPP13X2HDS13X2HDP13X2HWS13X8HWP I KQ 37280066
1021 FORMAT%/14X1HRI3X2HPB13X2HDB13X2HWB13X2HVM13X2HVI11X10HDPB8 I KQ37380066
1025 FORMAT%/7X3HRPM7X3HGP3X7HS POWER3X7HH POWERIX9HAVE PRESS3X7HHD R37480066
1ISE7X3HEFF/F10.2,6F10.4Q 37580066
1027 FORMAT%/5X5HOMEGA9X1HQ3X7HS POWER3X7HH POWERIX9HAVE PRESS3X7HHD R37680066
11SE7X3HEFF/F10.2,6F10.4Q 37780066
1029 FORMAT%/26HHUB TO TIP VZ DISTRIBUTION/7F10.4Q 37880066
10291 FORMAT%/26HHUB TO TIP PT DISTRIBUTION/7F10.4Q 37980066
END 38080066